OPHIR VALIANTE DUARTE NETO

Modelling and Analysis of Fluid Flow Problems Coupled With Radiative Heat Transfer

FEDERAL UNIVERSITY OF UBERLÂNDIA
SCHOOL OF MECHANICAL ENGINEERING
GRADUATE PROGRAM IN MECHANICAL ENGINEERING

2025

OPHIR VALIANTE DUARTE NETO

Modelling and Analysis of Fluid Flow Problems Coupled With Radiative Heat Transfer

Dissertation submitted to the Graduate Program in Mechanical Engineering at the Federal University of Uberlândia, as part of the requirements for the degree of Master in Mechanical Engineering.

Area of Concentration: Heat Transfer and Fluid Mechanics
Research Line: Computational Fluid Dynamics

Prof. Dr. João Marcelo Vedovotto
Advisor

Prof. Dr. Gilmar Guimarães
Coordinator of the Graduate Program in Mechanical Engineering

Uberlândia, Minas Gerais
2025

Dados Internacionais de Catalogação na Publicação (CIP)
Sistema de Bibliotecas da UFU, MG, Brasil.

D812m
2026

Duarte Neto, Ophir Valiante, 1997-
Modelling and analysis of fluid flow problems coupled with radiative heat transfer [recurso eletrônico] / Ophir Valiante Duarte Neto. - 2026.

Orientador: João Marcelo Vedovotto.
Dissertação (Mestrado) - Universidade Federal de Uberlândia, Programa de Pós-graduação em Engenharia Mecânica.
Modo de acesso: Internet.
Disponível em: http://doi.org/10.14393/ufu.di.2026.5513
Inclui bibliografia.
Inclui ilustrações.

1. Engenharia Mecânica. I. Vedovotto, João Marcelo, 1981-, (Orient.). II. Universidade Federal de Uberlândia. Programa de Pós-graduação em Engenharia Mecânica. III. Título.

CDU: 621.01

André Carlos Francisco
Bibliotecário-Documentalista - CRB-6/3408

UNIVERSIDADE FEDERAL DE UBERLÂNDIA
Coordenação do Programa de Pós-Graduação em Engenharia Mecânica
Av. João Naves de Ávila, nº 2121, Bloco 1M, Sala 212 - Bairro Santa Mônica, Uberlândia-MG, CEP 38400-902
Telefone: (34) 3239-4282 - www.posmecanicaufu.com.br - secposmec@mecanica.ufu.br

ATA DE DEFESA - PÓS-GRADUAÇÃO

Programa de Pós-Graduação em:	Engenharia Mecânica				
Defesa de:	Dissertação de Mestrado Acadêmico, nº 665, PPGEM				
Data:	21/08/2025	Hora de início:	13:30	Hora de encerramento:	16:30
:	12312EMC011				
Nome do Discente:	Ophir Valiante Duarte Neto				
Título do Trabalho:	Modelling and Analysis of Fluid Flow Problems Coupled With Radiative Heat Transfer				
Área de concentração:	Transferência de Calor e Mecânica dos Fluidos				
Linha de pesquisa:	Dinâmica dos Fluidos e Transferência de Calor				
Projeto de Pesquisa de vinculação:	Modelagem de caldeira de CO como combustor ciclônico - MFLab/Petrobras				

Reuniu-se por videoconferência a Banca Examinadora, designada pelo Colegiado do Programa de Pós-graduação em Engenharia Mecânica, assim composta: Prof. Dr. Francis Henrique Ramos França - UFRGS; Prof. Dr. Rogério Gonçalves dos Santos - UNICAMP; Prof. Dr. Gilmar Guimarães - UFU e Prof. Dr. João Marcelo Vedovotto - UFU; orientador do candidato.

Iniciando os trabalhos, o presidente da mesa, Dr. João Marcelo Vedovotto, apresentou a Comissão Examinadora e o candidato, agradeceu a presença do público, e concedeu ao Discente a palavra para a exposição do seu trabalho. A duração da apresentação do Discente e o tempo de arguição e resposta foram conforme as normas do Programa.

A seguir, o senhor presidente concedeu a palavra, pela ordem sucessivamente, aos examinadores, que passaram a arguir o candidato. Ultimada a arguição, que se desenvolveu dentro dos termos regimentais, a Banca, em sessão secreta, atribuiu o resultado final, considerando o candidato:

Aprovado.

Esta defesa faz parte dos requisitos necessários à obtenção do título de Mestre.

O competente diploma será expedido após cumprimento dos demais requisitos, conforme as normas do Programa, a legislação pertinente e a regulamentação interna da UFU.

Nada mais havendo a tratar, foram encerrados os trabalhos. Foi lavrada a presente ata que após lida e achada conforme foi assinada pela Banca Examinadora.

Documento assinado eletronicamente por **João Marcelo Vedovotto**, **Professor(a) do Magistério Superior**, em 21/08/2025, às 16:20, conforme horário oficial de Brasília, com fundamento no art. 6º, § 1º, do Decreto nº 8.539, de 8 de outubro de 2015.

Documento assinado eletronicamente por **Gilmar Guimarães**, **Professor(a) do Magistério Superior**, em 21/08/2025, às 16:21, conforme horário oficial de Brasília, com fundamento no art. 6º, § 1º, do Decreto nº 8.539, de 8 de outubro de 2015.

Documento assinado eletronicamente por **Rogério Gonçalves dos Santos**, **Usuário Externo**, em 22/08/2025, às 07:50, conforme horário oficial de Brasília, com fundamento no art. 6º, § 1º, do Decreto nº 8.539, de 8 de outubro de 2015.

Documento assinado eletronicamente por **Francis Henrique Ramos França**, **Usuário Externo**, em 23/08/2025, às 15:35, conforme horário oficial de Brasília, com fundamento no art. 6º, § 1º, do Decreto nº 8.539, de 8 de outubro de 2015.

A autenticidade deste documento pode ser conferida no site https://www.sei.ufu.br/sei/controlador_externo.php?acao=documento_conferir&id_orgao_acesso_externo=0, informando o código verificador **6581219** e o código CRC **BD947B22**.

Referência: Processo nº 23117.055017/2025-59 SEI nº 6581219

OPHIR VALIANTE DUARTE NETO

Modelling and Analysis of Fluid Flow Problems Coupled With Radiative Heat Transfer

Expected Dissertation by the Graduate Program in Mechanical Engineering at the Federal University of Uberlândia.

Area of Concentration: Heat Transfer and Fluid Mechanics
Research Line: Computational Fluid Dynamics

Uberlândia, August 21st, 2025.

Examination Committee:

Prof. Dr. João Marcelo Vedovotto (UFU)
Advisor

Prof. Dr. Gilmar Guimarães (UFU)
Internal member of the Examining Committee

Prof. Dr. Rogério Gonçalves dos Santos (UNICAMP)
External member of the Examining Committee

Prof. Dr. Francis Henrique Ramos França (UFRGS)
External member of the Examining Committee

Acknowledgements

To my family, especially my parents and grandparents, for the incredible amount of support and love that enabled me to follow this path. Their efforts can't be understated; nothing would be possible without them.

To my friends, who have time and again comforted me, gave me the support to endure troubling times, and with whom I've also shared many happy moments.

To my teachers, who at this point have stacked up to such an overwhelming number that I can't properly remember the faces, voices and even names of all, but who provided me with some of the most valuable gifts that exist.

To my colleagues in MFLab, who took me as their own and gave me much of the support I needed during my Master's. I can safely say that they're one of the main reasons of the laboratory's success: more than an institute of excellence, it is an environment forged in kinship and cooperation. Intelligence, skilfulness, resourcefulness, ambition, fame, these traits have little meaning if one keeps them to oneself.

Unfortunately, I can't mention everyone by names, but a few individuals are in order. My advisor, João Marcelo Vedovotto; his kindness, intelligence and hard work have supported the growth of many people and made an impact in society. Aristeu, the founding father of MFLab, whose passion and character have deeply inspired me. Ricardo Serfaty, who has been with the lab through thick and thin, and who inspired inspired the development of this work. Ricardo Catta Preta, who inspired me to accept my advisor's proposal of working with radiative heat transfer, a physicist with passion and poetry for his craft. Pedro Mota, a veteran of the Lab, who constantly supports the lab's students whenever he can; his help was paramount to the development of my work and I am glad we've crossed paths. Johnatas, technician, developer and an important member of MFLab, with whom I've shared many conversations and who's helped me plenty. And finally, Gabriel Magalhães and the team at Wikki Brazil, who helped and inspired me in enrolling in MFLab as a Master's student and researcher.

To CAPES, CNPq, FAPEMIG and Petróleo Brasileiro S.A. for their constant support on the research not only of MFLab, but of the Faculty of Mechanical Engineering (FEMEC) at the Federal University of Uberlândia. They are paramount to our success as an institution of excellence in education and research.

I would also like to thank the people at FEMEC, including our Graduate Programme Coordinator, Gilmar Guimarães, and his assistants, for their kindness and support.

A special thanks to Shihe Xin for promptly and kindly providing me with data from their thermal cavity experiments.

And to God, for everything.

"To exist is to change, to change is to mature, to mature is to go on creating oneself endlessly."

— Henri Bergson

DUARTE NETO, Ophir Valiante. *Modelling and Analysis of Fluid Flow Problems Coupled With Radiative Heat Transfer*. 140 p. Dissertation (M.Sc.) — Federal University of Uberlândia, Uberlândia, MG, Brazil, aug. 2025. Available from: http://doi.org/10.14393/ufu.di.2026.5513.

Abstract

Combustion plays a fundamental role in society, being one of the primary means of energy conversion and storage, with countless applications. As such, it is a key topic in engineering and industrial processes. In many cases, combustion and thermal radiation occur simultaneously: the high temperatures resulting from exothermic reactions, as well as the radiative interaction of the gases generated from these reactions, create an environment where complex radiative heat transfer takes place. Therefore, coupling CFD with radiative heat transfer models is essential for the accurate simulation of industrial reactive flows. Furthermore, literature shows that thermal radiation can significantly affect heat transfer in other situations, such as in thermal cavities at ambient temperature, a problem that is frequently studied without considering radiation effects. This work presents the development and benchmarking of a coupling between a CFD software (MFSim) and a radiative heat transfer solver for participating media (RTS), both internally developed by MFLab in the Federal University of Uberlândia. MFSim is a robust simulation package, capable of modelling turbulence, heat transfer, fluid–structure interactions, reacting flows, and Lagrangian particle transport. RTS is capable of modelling radiative transfer in gray and non-gray participating media containing gases like CO_2 and H_2O, as well as isotropic and anisotropic scattering phenomena. By integrating these codes, the extensive set of physical models available in MFSim, designed to simulate complex engineering problems, now includes radiative heat transfer, enabling more realistic and accurate modelling of combustion processes. The coupling employs distinct meshes for CFD and radiation, connected via interpolation, allowing for more computational efficiency, as radiative models do not usually require the same spatial resolution as CFD. Tests have shown that the interpolation layer between both algorithms has relatively low computational cost. Benchmarks performed on canonical cases show good agreement with the literature, verifying the approach and reinforcing the importance of radiation in heat transfer simulations.

Keywords: Computational Modelling, Heat Transfer, Computational Fluid Dynamics, Combustion, Radiation, Radiative Heat Transfer, Numerical Simulation.

DUARTE NETO, Ophir Valiante. *Modelling and Analysis of Fluid Flow Problems Coupled With Radiative Heat Transfer.* 140 f. Dissertação (Mestrado) — Universidade Federal de Uberlândia, Uberlândia, MG, Brasil, ago. 2025. Disponível em: http://doi.org/10.14393/ufu.di.2026.5513.

Resumo

A combustão desempenha um papel fundamental na sociedade, sendo uma das principais formas de conversão e armazenamento de energia, com inúmeras aplicações. Por isso, é um tema central em engenharia e processos industriais. Em muitos casos, combustão e radiação térmica ocorrem simultaneamente: as altas temperaturas resultantes de reações exotérmicas, assim como a interação dos gases gerados por essas reações com a radiação, formam um ambiente com processos complexos de transferência de calor radiativa. Assim, o acoplamento entre CFD e modelos de transferência de calor radiativa é essencial para a modelagem acurada de escoamentos reativos industriais. Além disso, a literatura mostra que a radiação térmica pode afetar a transferência de calor significativamente em outras situações, como em cavidades térmicas a temperatura ambiente, um problema que frequentemente é estudado sem considerar efeitos de radiação. Este trabalho apresenta o desenvolvimento e benchmarking de um acoplamento entre um software CFD (MFSim) e um solver de radiação térmica para meios participantes (RTS), ambos desenvolvidos internamente pelo MFLab na Universidade Federal de Uberlândia. O MFSim é um pacote robusto de simulação computacional, capaz de modelar turbulência, transferência de calor, interações fluido-estrutura, escoamentos reativos e transporte lagrangiano de partículas. Já o RTS é capaz de modelar transferência de calor radiativa em meios participantes cinza e não-cinza contendo gases como CO_2 e H_2O, assim como espalhamentos isotrópico e anisotrópico. Integrando os dois códigos, o conjunto extenso de modelos físicos disponíveis no MFSim, desenvolvidos para simular problemas complexos de engenharia, agora inclui transferência de calor radiativa, permitindo uma modelagem mais realista e acurada de processos de combustão. O acoplamento utiliza malhas distintas para CFD e radiação, conectadas por interpolação, o que permite maior eficiência computacional, já que modelos radiativos não costumam exigir a mesma resolução espacial do CFD. Testes mostraram que a camada de comunicação entre os códigos tem custo computacional relativamente baixo. Benchmarks em casos canônicos demonstraram boa concordância com a literatura, verificando a abordagem e reforçando a importância da radiação em simulações de transferência de calor.

Palavras-chave: Modelagem Computacional, Transferência de Calor, Dinâmica dos Fluidos Computacional, Combustão, Radiação, Transferência de Calor Radiativa, Simulação Numérica.

List of Figures

List of Tables

List of Algorithms

List of abbreviations and acronyms

Institutions and Organizations

CAPES	Coordination for the Improvement of Higher Education Personnel
CNPq	National Council for Scientific and Technological Development
FAPEMIG	Minas Gerais State Agency for Research and Development
MFLab	Fluid Mechanics Laboratory
Petrobras	Petróleo Brasileiro S.A.
UFU	Federal University of Uberlândia

Other acronyms

BICGStab	Biconjugate Gradient Stabilized Method
CFD	Computational Fluid Dynamics
DNS	Direct Numerical Simulation
DOM	Discrete Ordinates Method
DSAL	Directional Sweep Algorithm
FAM	Finite Angles Method
FSK	Full Spectrum Correlated-k
FVM	Finite Volume Method
GMRES	Generalized Minimal Residual Method
IBM	Immersed Boundary Method
KSP	Krylov Space
LBL	Line by Line
LES	Large Eddy Simulation
P_N	Spherical harmonics P_N Method
$RMSE$	Root Mean Square Error

$RMSE_{\text{rel.}}$	Root Mean Square of Relative Error
RTE	Radiative Transfer Equation
RTS	Radiative Transfer Simulator
SLW	Spectral Line Based Weighted Sum of Gray Gases
SNBM	Statistical Narrow Band Model
TRI	Turbulence Radiation Interaction
WSGG	Weighted Sum of Gray Gases

Units and Measurements

m	meter (length)
kg	kilogram (mass)
s	second (time)
N	Newton (force)
Pa	Pascal (pressure)
J	Joule (energy)
°C	degree Celsius (temperature)
K	Kelvin (temperature)

Mathematical Operators

Δ	Finite difference (i.e. $\Delta y = y(x_2) - y(x_1)$)
$\frac{\partial}{\partial x}$	Partial derivative with respect to x
∇	Gradient operator
$\nabla\cdot$	Divergence of a vector field
∇^2	Laplacian operator
$\cdot$	Dot product
$\times$	Cross product
$\langle\phi\rangle$	Time averaged value of ϕ

List of symbols

Primary Symbols

A	Area
A_p	Projected area
Bo	Boltzmann number
c	Speed of light
c_0	Speed of light in a vacuum
E_b	Emissive power of a blackbody
g	Gravitational acceleration
h	Planck's constant
I	Radiative intensity
I_b	Intensity of emitted radiation
k	Thermal conductivity
k_B	Boltzmann's constant
L	Characteristic length of a cavity
N_C	Radiation-conduction parameter
$\hat{n}$	Normal direction
Pl	Planck number
Pr	Prandtl number
Q	Energy
Ra	Rayleigh number
$\hat{s}$	Direction of a beam of radiation
$\vec{S}_i$	Direction $\hat{s}$ integrated over a discrete solid angle
T	Temperature
t	Time

u	U-velocity
w	DOM weight, w-velocity
$\vec{x}$	Position in space

Greek Symbols

α	Thermal diffusivity, absorptivity
β_e	Extinction coefficient
β_e	Thermal expansion coefficient
ϵ	Emissivity
η	Wave number
θ	Polar angle, dimensionless temperature
κ	Absorption coefficient
ν	Frequency, kinematic viscosity
ρ	Specific mass, reflectivity
σ	Stefan-Boltzmann coefficient
σ_s	Scattering coefficient
τ	Optical thickness
τ_t	Transmissivity
ϕ	Azimuthal angle
Φ	Phase function
$\bar{\Phi}$	Phase function integrated over discrete solid angle
Ω	Solid angle

Subscripts

η	Field value for wavenumber η
ν	Field value for frequency ν
i	Field value for discrete direction $\hat{s}_i$
j	Field value for discrete direction $\hat{s}_j \neq \hat{s}_i$

P	Discrete field value at the centroid of reference cell P
f	Discrete field value at the centroid of cell face f
w	Discrete field value at boundary surface centroid w
U	Discrete field value at the centroid of upwind cell U
N	Discrete field value at neighbour cell N
∞	Upstream flow condition or reference value at "infinity" (e.g., u_∞)

Superscripts

$\rightarrow$	A first order tensor (i.e. a vector)
$\overrightarrow{\rightarrow}$	A second order tensor (or simply tensor)
$\hat{}$	A unit vector

Contents

1 Introduction

Thermal energy transfer can happen through three distinct mechanisms: conduction, convection, and radiation. In the latter case, thermal energy is carried via photons that can be emitted, reflected, or absorbed by a physical object, which can be a solid, a liquid, a gas, and so on. Given that it is transported through electromagnetic waves, it can propagate through a vacuum and across long distances at the speed of light; conduction and convection, on the other hand, have a much more limited range. The main example of this form of energy transfer is how the sun heats and illuminates the earth; other examples include the heat from a bonfire, which is mainly due to radiation; and how closing the curtains in a cold winter helps keep the room warm, as it stops thermal energy from escaping the room through radiation (Modest; Mazumder, 2022).

The study of thermal energy transfer via radiation is known to be quite difficult, requiring knowledge of topics such as optics, quantum physics, and partial differential equations. In many practical problems, convection and conduction are responsible for most of the transport of thermal energy, causing people to avoid considering the effects of radiation because of the relative difficulty in studying it. Another reason may simply be oversight, with radiative heat transfer being ignored in situations where it may be unexpectedly important; this will be discussed further in the text. Nevertheless, it has been shown to have a considerable effect for many other problems. One such instance is combustion processes, which range from industrial problems, such as gas flow inside a boiler (Orbegoso, 2013), to safety engineering problems, such as fire propagation in forests or buildings (Shen; Huang; Chien, 2008).

Radiation also has complex interactions with fluid dynamics, an area of study which is still relatively unknown. For example, radiation influences and is influenced by turbulence (Coelho, 2007), a fact which is not trivial to understand or model. To this date, there are ongoing studies on the interaction between turbulence and radiation, such as in Kogawa *et al.* (2021) or Coelho and Fraga (2024). A particular challenge is setting up physical experiments, due to the fact that the radiative field intensities are hard to measure. In this vein, numerical simulations help give more details.

In combustion systems, not only there is turbulence, but also chemical reactions and a series of participating gas species, which further complicates the modelling process. The presence of solid particles like soot, which interacts with radiation, is also another challenge to be considered. In spite of this, researchers have managed to model and simulate this kind of environment, showcasing relatively good predictions for soot and NO_x formations, such as in Liu *et al.* (2002a) and Lee *et al.* (2013).

The mathematical modelling and simulation of radiative thermal energy transfer

is based on the radiative transport equation (RTE), an integro-differential equation based on seven variables (three spatial, two directional, one for time and another one for wavelength). The RTE is used in other areas of physics where electromagnetic wave phenomena are present, like the transport of neutrons inside a nuclear reactor. This equation, when solved, yields the radiative intensity field, which describes how radiation propagates in a medium and can be used to determine the radiative heat fluxes in it.

Many models have been developed over the years for solving the RTE, with Chandrasekhar (1960) being one of the first. Spherical Harmonics, Monte Carlo and Ray-tracing are some of the models for solving the RTE. The use of the Discrete Ordinate Method (DOM) or the Finite Angles Method (FAM) for discretizing the angular domain, coupled with traditional Finite Elements or Finite Volumes Methods for space discretization, have been found to be a good cost-benefit for accurate results and are commonly implemented in commercial and/or open source software like OpenFOAM, AnSys and FDS. Other methods dedicate themselves to solving the spectral dimension, either by simplifying the band (like the Gray Gas Method or the Weighted Sum of Grey Gases Method), to fully solving it, like the Line-by-Line integration method. Ongoing studies attempt to optimize the integration of the spectral dimension, in search of fast and accurate algorithms (Asllanaj *et al.*, 2023).

The biggest challenge in solving the RTE is mainly due to the following factors:

- **Cost:** The simulation of radiative transfer is costly due to its multidimensional nature. That is, for a given (x, y, z) point in a three-dimensional space, the radiative intensity is directional, that is, it is dependent on the direction (ϕ, θ). Effectively, this leads to a five-dimensional domain, which requires more complex modelling and a larger mesh, which make it more expensive to solve. This is further complicated by the tight coupling between angular directions in certain scenarios, such as in scattering and non-gray boundaries;

- **Spectral nature:** Thermal energy transfer occurs within a certain range of the electromagnetic spectrum. The radiative properties of the system being analysed can change with the wavelength of the radiation that is carrying the thermal energy, thus requiring calculation of the radiative intensity over this entire range, leading to another cost increase. Effectively, this constitutes to a six-dimensional problem $(x, y, z, \phi, \theta, \nu)$. Models like the weighted sum of grey gases (WSGG) try to reduce the computations in the spectral domain, but in many cases they cannot be fully eliminated, leading to a cost increase;

- **Participating media:** If the media through which the radiation propagates interacts with it by emission, absorption or scattering, it is called a participating media. This participating media can be relatively simple, like a gray gas that has

constant properties over the spectrum, or even pre-defined spectral properties. It could also be a mixture of real gases, like CO_2 and H_2O vapour, which require more complex modelling to calculate the overall emission, absorption and scattering effects of the media, while accounting for spectral effects. This is further aggravated in couplings with Computational Fluid Dynamics solvers, where these properties are also a function of the temperature, pressure and species molar fractions;

Other challenges in designing a radiative transfer solver are:

- **Boundaries:** Defining boundary conditions in radiative transfer problems can be a challenge, depending on how general and complex the boundary modelling needs to be. For example, a diffusively reflecting and opaque boundary is relatively simple to model. However, there could be walls with specular reflection or some level of transparency, which increase its complexity. Boundary conditions must also take into account the directionality of the radiation rays, meaning that they change based on the analysed direction. Boundaries also establish a coupling between these different directions.
- **Finite directions:** Radiation happens in an infinite number of directions, but deterministic solvers need to break them into finite directions, and in doing so, introduce numerical artifacts like ray effects in the solution, or overhang in boundary conditions. This requires not only developing smart solvers that can mitigate these issues, but also user knowledge in setting up well-balanced cases that are not too costly but yield acceptable results.

Radiative heat transfer solvers are commonly run together with Computational Fluid Dynamics (CFD) algorithms. They can be classified in many ways, from simple models to more complicated ones. The choice usually revolves around the requirements of the user and the computational costs involved. For example, deterministic solvers based on the Finite Volume with Discrete Ordinates discretization of the RTE are quite complex and noticeably heavy, but allow modelling complex scenarios with participating media and strong scattering, while allowing for refinement to arbitrary precisions (though this may not always be feasible). Other solvers may not be as generally applied, such as the Spherical Harmonics P_1 method. Others, still, may provide even better results, such as Photon Monte Carlo based stochastic solvers, which, despite being computationally intensive and historically quite expensive, are becoming more accessible thanks to modern GPUs.

This work dedicates itself to the development and testing of the coupling between a fluid dynamics solver (MFSim) and a radiative heat transfer solver (RTS), both developed in-house at the Fluid Mechanics Laboratory at the Federal University of Uberlândia. MFSim is a finite volume based CFD software with adaptive dynamic mesh

and several libraries for simulating complex multiphysics phenomena. RTS is a recently developed finite-volume based solver for radiation that implements the P1, DOM and FAM methods, as well as a WSGG model and anisotropic scattering (Rodrigues, 2023). This coupling is, then, applied to two different thermal cavities with radiative heat transfer effects, respectively described by Yücel, Acharya and Williams (1989) and Salat *et al.* (2004). The resulting flow field is then analysed, discussed and compared with the results obtained by these authors. With this coupling verified, further simulations of flows containing radiative heat transfer may be performed, allowing for further research in flows with radiative heat transfer, such as combustion processes.

1.1 Objectives

The overall research aims to solve turbulent reactive flows coupled with radiative heat transfer. In this particular work, the goals are to develop tools for bridging the gap between a CFD code (that solves the turbulent reactive flow) and a pure RTE code that determines the radiative intensity of the medium. It follows the work of Rodrigues (2023), and aims to couple RTS, the in-house developed radiative transfer code, with MFSim, the in-house code for general CFD problems. Other objectives, like a bibliographic review on radiative heat transfer in fluid dynamics and on solver design for the RTE, are also part of this work. In summary, these are its main objectives:

- Bibliographic review of radiative heat transfer, and its particular presence and influence in fluid flow problems;
- Study of both MFSim and RTS code, in order to understand well the inner workings of both packages and how they can communicate;
- Development of tools capable of bridging a two-way communication between the two packages;
- Testing and benchmarking of the communication layer with canonical problems.

2 Thermal Radiation

This chapter introduces the fundamental concepts of radiative transfer, its respective modelling and its importance. Furthermore, it defines clearly what is thermal radiation and radiative heat transfer, in contrast to the generic term ”radiation”.

2.1 Introduction

Radiation is an umbrella term that can describe many different phenomena. One type of radiation is **electromagnetic radiation**, which can be interpreted either as massless particles known as photons crossing through space, or as electric and magnetic fields that are perpendicular to each other and to their direction of propagation, oscillating in a sinusoidal fashion. Both interpretations are correct and complementary, resulting in what is called the wave-particle duality. There are cases where one interpretation is more adequate to understand a physical process than the other. Electromagnetic radiation comprises a spectrum of wavelengths (or frequencies) that is divided according to their origin and interactions with matter: gamma radiation, x-rays, ultraviolet, visible light, infrared, microwaves, radio waves, and so on.

In the particular case of this work, we are interested in a subset of the electromagnetic radiation spectrum comprised between wavelengths $0.1\ \mu m$ and $100\ \mu m$, which represents a range from the middle of the infrared to the middle of ultraviolet bands (Figure 1). This type of radiation transports energy in such a way that it is perceived as heat, and thus is aptly called **thermal radiation**. Electromagnetic radiation outside of this range transports energy, but is not emitted solely due to a medium’s temperature and isn’t of much concern in heat transfer applications (Modest; Mazumder, 2022).

Due to being transported via electromagnetic waves, thermal radiation has quite unusual properties when compared with the other modes of heat transfer, namely conduction and advection. More specifically, this transport typically occurs at relativistic speeds and may happen across a variety of scales: Modest and Mazumder (2022) cites that the mean free path of a photon may range from $1\ \mathring{A}$ to ten million kilometres. In comparison, conduction and advection mechanisms have more localized influence, and heat takes longer to propagate. Another quirk of radiative heat transfer is that it is proportional to the fourth power of the temperature (T^4), while conduction is proportional only to its first power (T) and advection is somewhere between T and T^2 (Howell; Mengüç; Siegel, 2015). This means that radiative heat transfer becomes increasingly important as the temperature difference increases, making it especially relevant in situations like combustion systems.

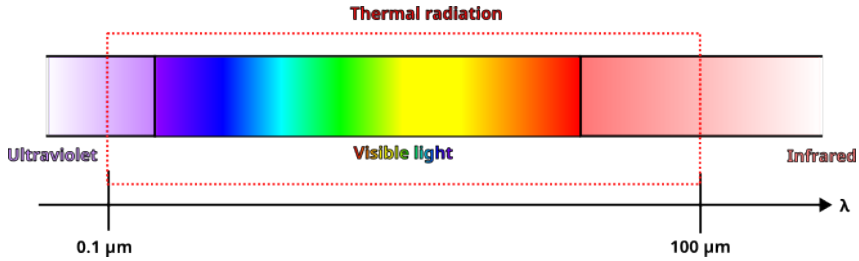

Figure 1 – Illustration of the thermal radiation range in the electromagnetic spectrum.

Thermal radiation can be interpreted as a thin, concentrated beam of electromagnetic radiation that moves at the speed of light of the medium it is immersed in, known as a ray. In a given instant, an infinitude of such rays are crossing through a physical system, in all directions, and without interacting with each other. These rays tend to travel in a straight line, unless they encounter some obstacle, which can then reflect, diffract, refract or absorb them, altering their path. This obstacle is a physical body itself, and thus is also emitting thermal radiation, as long as its temperature is above $0\ K$.

Such obstacles can be particles, walls, or even air molecules. As such, it is interesting to differentiate between continuous and discrete analysis of radiative transport. For instance, consider a beam of solar radiation crossing through the Earth's atmosphere. As this beam crosses Earth's atmosphere, it interacts with the molecules present in it, which may absorb, refract, diffract or reflect this beam. These are discrete processes that happen individually to each photon present in the beam and which globally translate to a combined effect of absorption and scattering. In this scenario, the atmosphere may be understood as a continuous media possessing coefficients of absorption and scattering, and the beam is interpreted to be continually absorbed or scattered as it crosses the atmosphere. These effects become more intense as these coefficients grow larger, and the more intense they are, the less the beam tends to cross the region in a straight line without losing its energy. This global approach is quite convenient and is the foundation for studying radiative transfer in continuous physical systems.

2.2 Spherical coordinates

The nature of thermal radiation makes it so that it is necessary to describe it not only in terms of where a ray is located at, but also in the direction it is pointing towards, which may be defined as $\hat{s}$. This direction is usually described in terms of the spherical coordinates θ, the **polar angle**, and ϕ, the **azimuthal angle**, which are enough to define $\hat{s}$, as seen in Figure 2. The spherical radius, which is necessary to describe any point in space, is left out as only the direction of the ray is of interest. Thus, it can be said that, in the study of radiative transfer, only the unit sphere and the angular coordinates it contains (i.e. the set of values of $\hat{s}$) are of important consideration.

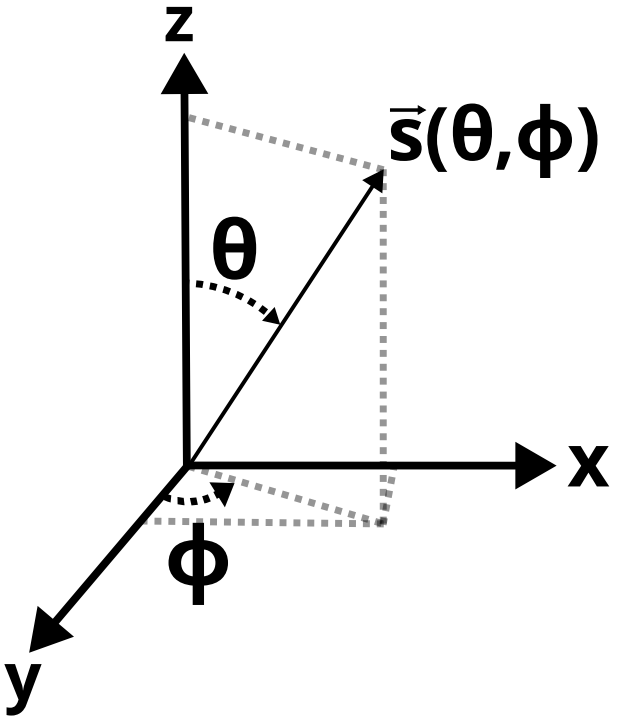

Figure 2 – Spherical coordinates.

To each ray transporting radiation, an infinitesimal **solid angle** $d\Omega$ describes the region it is affecting, as in Figure 3. The solid angle is the three dimensional analogue of an angle: much like the angle in a circle ranges from 0 to 2π and is associated to the length of a section of a circle, a solid angle ranges from 0 to 4π and is associated to the area of a section of a sphere. It is usually denoted by the greek letter Ω, and defined in terms of θ and ϕ as:

$$d\Omega = \sin(\theta)\ d\theta\ d\phi. \tag{2.1}$$

$$\Omega = \int_{\phi_1}^{\phi_2} \int_{\theta_1}^{\theta_2} \sin(\theta)\ d\theta\ d\phi. \tag{2.2}$$

Describing the area of influence of a set of rays, then, requires integration over its correlated solid angle. As a consequence, solid angles form part of the foundation for mathematically modelling radiative transfer, much like spherical coordinates.

2.3 Radiative intensity

The basic unit for measuring the energy transported by means of thermal radiation is the **radiative intensity**, I, as defined by authors such as Modest and Mazumder (2022) and Howell, Mengüç and Siegel (2015). If one imagines that a body's surface is constantly emitting radiation to all directions and absorbing radiation from all directions, then the power contained in each direction is measured in terms of the radiative intensity

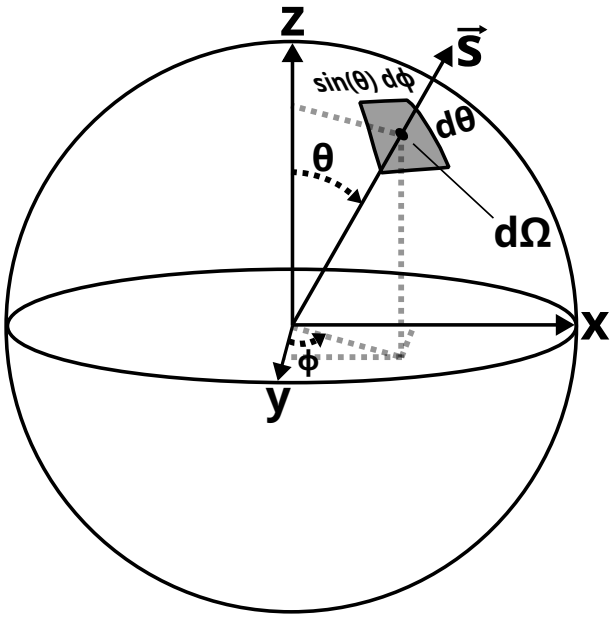

Figure 3 – Solid angle.

(Figure 4). It measures energy transferred per unit time interval, per unit projected area, per unit solid angle, per unit wavelength interval (Howell; Mengüç; Siegel, 2015):

$$I = \lim \frac{\partial^4 Q}{\partial t \; \partial A_p \; \partial \Omega \; \partial \lambda}. \tag{2.3}$$

In a physical system, all information about the radiative heat transfer of this system can be described by the **radiative intensity field**. This field has the distinctive property of containing not only components in the spatial positions x, y and z and time t, as usual in other transport problems, but also directional components, described in spherical coordinates as θ and ϕ, and a component in the electromagnetic spectrum, λ. This is due to the **directional and spectral nature** of radiation: it can be understood to move through space as a series of infinitesimally small rays, each with a given direction and which may occupy the same physical space of other rays. These rays may or may not interact with their surroundings, and their interactions depend on their position in the electromagnetic spectrum.

Good examples of how radiative transfer can be significantly different depending on the wavelength of the ray are certain kinds of plastic bags, which are opaque to visible light, but translucent to infrared, as in Figure 5. In the same picture, it can also be observed that the man's eyeglasses are practically transparent to visible light, **transmitting** most of the radiation, but are essentially black and opaque in the infrared image, meaning that rays in this wavelength are being **absorbed**. Another good example is in Figure 6, which displays that smoke, despite being optically thick in visible light, is thinner in the infrared, a fact which can be used in search and rescue during firefighting operations. Yet another interesting example is how human breath is invisible to the

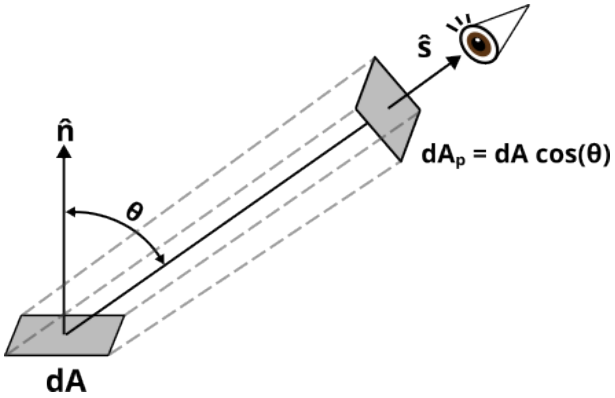

Figure 4 – Illustration of a beam emitted by a surface dA with radiative intensity I being received at the projected surface dA_p. Figure adapted from Modest and Mazumder (2022).

Figure 5 – The spectral properties of materials change spectrally. The left picture is taken from a normal camera, while the right is taken with an infrared camera. One can observe the man's hands through the plastic bag on the right picture, but not on the left. Similarly, his glasses are opaque in the infrared picture. Figure taken by NASA and adapted from Hurt (2025).

Figure 6 – Example of infrared camera usage for identifying people in thick smoke, showing how optical thickness can be different for different regions of the electromagnetic spectrum. Figure issued by specialty camera manufacturer FLIR and taken from Bhowmik and Sen (2016).

naked eye, but may be seen with thermal imaging (Figure 7), a fact which inspired some researches during the COVID-19 pandemic.

All of these cases give intuitive, visible examples of how **participating media** acts: it somehow interacts with radiation, affecting its intensity field. For example, human breath is visible in the infrared spectrum because it interacts with infrared radiation, but

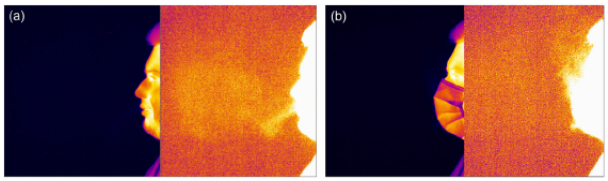

Figure 7 – Human breath makes a visible "mist" in the infrared spectrum, despite being invisible for the naked eye. This can help measure the effectiveness of face masks. Figure taken from Koroteeva and Shagiyanova (2022).

is invisible in the visible light spectrum, as it is transparent to this band. How intensely a media affects thermal radiation is measured by means of an **absorption coefficient** and a **scattering coefficient**. Globally, this leads to the concept of **optical thickness**, a dimensionless number defined as a product of a length and the sum of the absorption as scattering coefficients. The thicker the environment, the more it affects radiation that passes through it. In combustion systems environments, the medium may have a broad range of optical thicknesses, each with its more adequate modelling. In general, this means that analysing radiative heat transfer in these systems is not always possible with a simple model, requiring a more generalized and complicated one.

2.4 Emission of thermal radiation

This section relates to how physical bodies emit thermal radiation, a phenomenon described by Prévost's Law. It contains a brief historical description on the studies of thermal radiation emission, followed by the definition of the law that describes it (Planck's Law). The equation given by Planck's Law is then integrated it to find Stefan-Boltzamann's law. An explanation of Lambertian emission is also given, which is important in the conceptual definition of thermal radiation emission.

2.4.1 Prévost's law and the blackbody

Any body whose temperature is above $0\ K$ emits energy in the form of thermal radiation. This happens due to atomic and molecular processes that release energy in the form of photons, such as molecular vibrations or electron shifts in energy levels. This occurs randomly and towards all directions at the same time, even when the body is in thermal equilibrium with its surroundings, a fact that is known as Prévost's law (Howell; Mengüç; Siegel, 2015).

The emission of thermal radiation can be structured under the analysis of an idealized body that absorbs all the incident thermal radiation from all wavelengths, suitably dubbed the **blackbody**. One can also prove that, due to this characteristic, the blackbody also emits more thermal radiation than anything else: suppose that a blackbody is placed inside of a cavity that is isolated from the exterior and at thermal equilibrium with

it. Due to being at thermal equilibrium, both the body and the cavity must emit as much energy as they absorb; otherwise, their temperature would change, which violates the thermal equilibrium. Therefore, the blackbody is not only a perfect absorber, but a perfect emitter. In general, good emitters are usually good absorbers, and vice-versa. This explains why blankets for use in space (Mylar blankets) are made of reflective material, as they minimize radiative heat loss through emission. It can also be proven that a blackbody has a uniform emission pattern (Howell; Mengüç; Siegel, 2015): that is, it emits the same amount of energy in all directions for all points in its surface.

Predicting the radiative intensity emitted from a blackbody was a challenge that stumped late XIX century and early XX century physicists, and was so infamous that it was dubbed the "ultraviolet catastrophe". This "catastrophe" was eventually solved by Max Planck, who proposed a novel model that assumed that this radiation could only be emitted and absorbed in discrete amounts of energy known as a quanta Q, defined as a function of its frequency ν and whose size is given by:

$$Q = h\nu,$$

where $h = 6.62606957 \times 10^{-34}\ J/s$ is **Planck's constant**. This theory contrasts with classical physics, where energy was thought to be absorbed and emitted in a continuous fashion and where the radiation's energy was thought to be a function only of its amplitude and unrelated to its frequency (Nussenzveig, 1998). This discovery marked the beginning of modern physics and the adoption of the quantum model. It also illustrates how thermal radiation is quite deeply intertwined with modern physics.

Planck then established a law that determines the emissive power $E_b(T, \nu)$ of a beam with frequency ν emitted by a blackbody at temperature T. This law can also be adapted to determine the emitted radiative intensity $I_b(T, \nu)$ of a blackbody. Planck's law and blackbody radiative emissions will be discussed further in the subsections below. Both E_b and I_b can also be defined based on the beam's wavelength λ, leading to $E_b(T, \lambda)$ and $I_b(T, \lambda)$, which will be used from now on to characterize the spectral dimension.

2.4.2 Lambert's law and emissive power

Imagine a black surface emitting thermal radiation towards another surface, as shown in Figure 4. The energy transfer between these surfaces can be described as the black surface's **directional emissive power** $E_{b,d,\lambda}$, which gives the power emitted by the surface per unit surface area of the *emitting element* per unit solid angle per unit wavelength. This contrasts with radiative intensity, which is the power emitted by the surface per unit area *normal to the propagation direction* per unit solid angle per unit wavelength. The radiative intensity of a black surface is constant in all directions and its directional emissive power is given by **Lambert's law**, which states that:

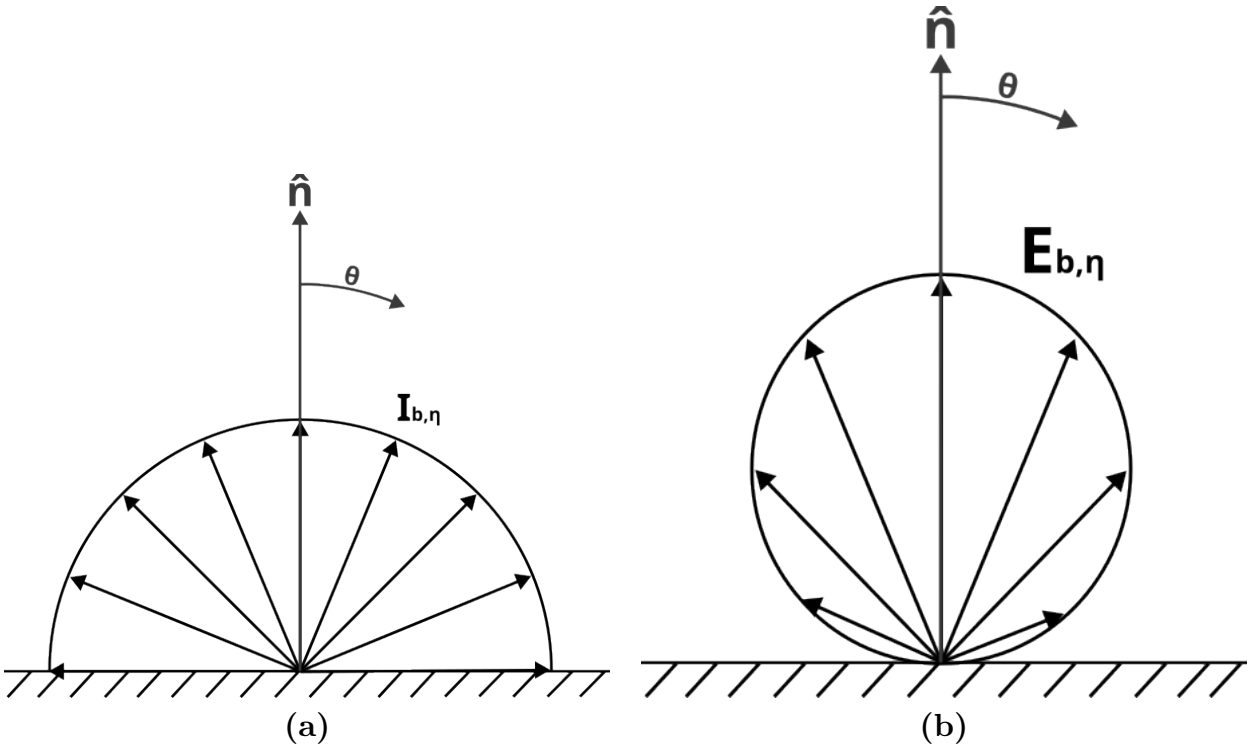

Figure 8 – Illustration of a surface with Lambertian emission. Figure adapted from Modest and Mazumder (2022).

$$E_{b,d,\lambda} = I_{b,\lambda} \cos(\theta). \tag{2.4}$$

That is, the directional emissive power is maximum at the zenith ($\theta = 0$) and decreases as the angle between the surface normals grows. Any surface in which this law holds true, including black surfaces, is known as **Lambertian**. An example can be seen in Figure 8.

In nature, some surfaces can be satisfactorily be described as Lambertian and, as such, their emission may also be modelled as similar to a blackbody. Other real surfaces, however, cannot be considered Lambertian, such that characterizing their emission pattern can be quite challenging as the radiative intensity is now not uniform in all directions. An intuitive (and rather extreme) example of non-Lambertian emission would be, for example, the beam of a laser diode, which exhibits strong directionality, much like in Figure 9. Owing to its practicality and applicability, computational models of radiative heat transfer often employ Lambertian emission for characterizing surfaces, which is often enough to satisfactorily describe them.

It is important to define the **emissive power** $E_{b,\lambda}$ of a black surface, which describes the total power emitted by the surface per unit area per unit wavelength:

$$E_{b,\lambda} = \int_0^{2\pi} \int_0^{\frac{\pi}{2}} I_{b,\lambda} \cos(\theta) \sin(\theta)\ d\theta\ d\phi = \pi I_{b,\lambda}. \tag{2.5}$$

Equation 2.5 is simply an integral over the hemisphere that bounds all outgoing rays that exit the black surface. It is especially important to relate Planck's law and

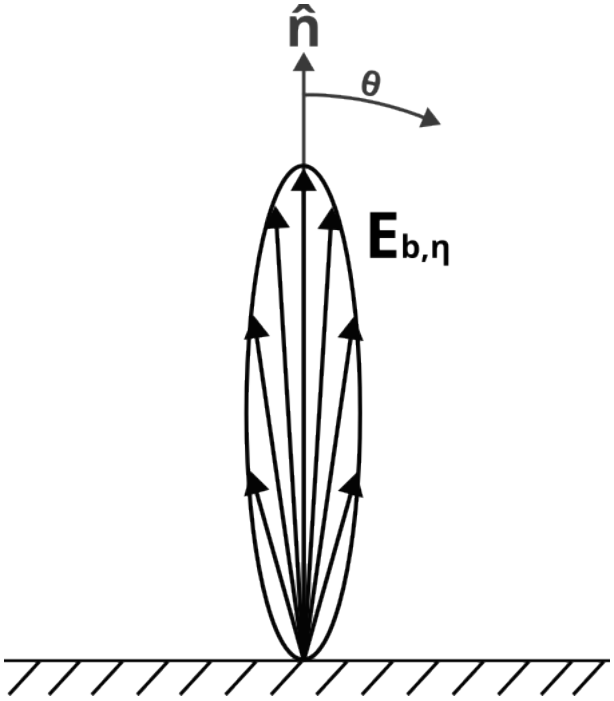

Figure 9 – Illustrative example of the emissive power of a non-Lambertian surface with high directionality.

Stefan-Boltzmann's law to the radiative intensity $I_{b,\lambda}$ that a black surface emits.

2.4.3 Planck's law

Planck's law states that the emissive power of a beam at a wavelength λ emitted by a blackbody at temperature T is given by:

$$E_b(T,\lambda) = \frac{2\,\pi\,h\,c_0^2}{\lambda^5\,n^2[\exp(\frac{h\,c_0}{\lambda\,n\,k_B\,T}) - 1]}. \tag{2.6}$$

Where n is the medium's refractive index, c_0 is the speed of light in the vacuum, h is Planck's constant and k_B is Boltzmann's constant. The refractive index n is assumed to be constant, that is, it is not a function of T or λ, which is reasonable for the vaccuum, ordinary gases and certain semi-transparent media (Modest; Mazumder, 2022). Substituting the wavelength for the wavenumber $\eta = \frac{1}{\lambda}$, Equation 2.6 can be re-written in terms of the wavenumber. As $E_b(T,\lambda)$ is a spectral density, it must obey the following expression:

$$\int_0^\infty E_b(T,\lambda)\,\mathrm{d}\lambda = \int_0^\infty E_b(T,\eta)\,\mathrm{d}\eta, \tag{2.7}$$

which leads to:

$$\begin{aligned} E_b(T,\lambda)\,\mathrm{d}\lambda &= E_b(T,\eta)\,\mathrm{d}\eta, \\ E_b(T,\eta) &= E_b(T,\lambda)\,\left|\frac{\mathrm{d}\lambda}{\mathrm{d}\eta}\right|. \end{aligned} \tag{2.8}$$

The modulus of the derivative is used to ensure that the integration remains the same over the same interval $[0, \infty)$. Given that $\frac{\mathrm{d}\lambda}{\mathrm{d}\eta} = -\frac{1}{\eta^2}$, then:

$$E_b(T,\eta) = \frac{2\,h\,\pi\,c_0^2\,\eta^5}{n^2\,[\exp(\frac{h\,c_0\,\eta}{n\,k_B\,T}) - 1]} \cdot \left| -\frac{1}{\eta^2} \right|,$$
$$E_b(T,\eta) = \frac{2\,h\,\pi\,c_0^2\,\eta^3}{n^2\,[\exp(\frac{h\,c_0\,\eta}{n\,k_B\,T}) - 1]}. \tag{2.9}$$

The wavenumber will be henceforth used to describe the spectral dimension. The notation $E_b(T,\eta) = E_{b,\eta}(T)$ will also be adopted to denote this quantity's spectral nature. Planck's law establishes the emission of thermal radiation in a generalized manner and is a fundamental building block in radiative heat transfer models.

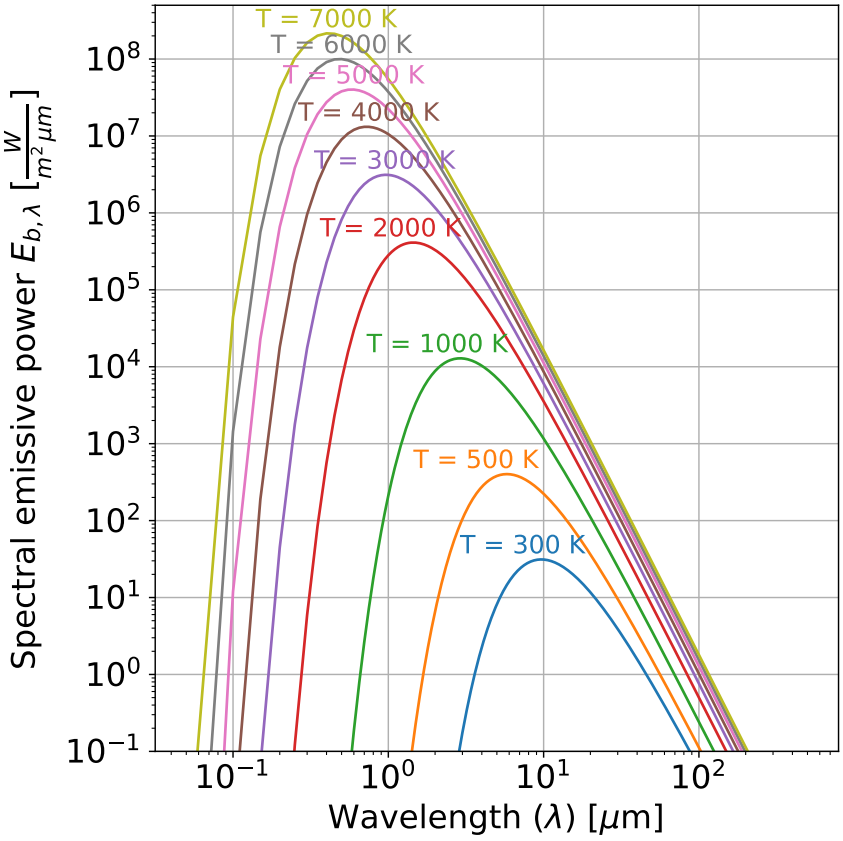

Figure 10 – Plot of Planck's law for several temperature profiles.

2.4.4 Stefan Boltzmann Law

If Equation 2.9 is integrated over the entire electromagnetic spectrum, we have:

$$E_b(T) = \int_0^\infty E_{b,\eta}(T)\ \mathrm{d}\eta,$$

$$E_b(T) = \int_0^\infty \frac{2\,h\,\pi\,c_0^2\,\eta^3}{n^2\,[\exp(\frac{h\,c_0\,\eta}{n\,k_B\,T}) - 1]}\ \mathrm{d}\eta, \tag{2.10}$$

$$E_b(T) = \frac{2\,h\,\pi\,c_0^2}{n^2}\int_0^\infty \frac{\eta^3}{\exp(\frac{h\,c_0\,\eta}{n\,k_B\,T}) - 1}\ \mathrm{d}\eta. \tag{2.11}$$

Let $C_0 = \frac{2\,h\,\pi\,c_0^2}{n^2}$ and $C_1 = \frac{h\,c_0}{n\,k_B\,T}$. To perform the integration, we adopt the following substitution:

$$\xi = C_1\,\eta,\ \mathrm{d}\eta = \frac{1}{C_1}\,\mathrm{d}\xi \tag{2.12}$$

Then:

$$E_b(T) = \frac{C_0}{C_1^4}\int_0^\infty \frac{\xi^3}{\exp(\xi) - 1}\,\mathrm{d}\xi. \tag{2.13}$$

The above integral can be solved analytically and yields:

$$\int_0^\infty \frac{\xi^3}{\exp(\xi) - 1}\,\mathrm{d}\xi = \frac{\pi^4}{15}. \tag{2.14}$$

And therefore:

$$E_b(T) = \frac{C_0}{C_1^4}\frac{\pi^4}{15}. \tag{2.15}$$

Finally:

$$E_b(T) = \frac{2\,h\,\pi\,c_0^2}{n^2}\left(\frac{n\,k_B\,T}{h\,c_0}\right)^4\frac{\pi^4}{15},$$

$$E_b(T) = \frac{2}{15}\frac{\pi^5\,k_B^4}{h^3\,c_0^2}\,n^2\,T^4,$$

$$E_b(T) = \sigma\,n^2\,T^4. \tag{2.16}$$

Where $\sigma = \frac{2\,\pi^5\,k_B^4}{15\,h^3\,c_0^2}$ is **the Stefan-Boltzmann constant** and is equal to $\sigma = 5.6697 \times 10^{-8}\ Wm^{-2}K^{-4}$. Equation 2.16 evaluates the total emissive power of a perfect blackbody. Applying Equation 2.5, the emitted radiative intensity of the blackbody can also be calculated:

$$I_b(T) = \frac{1}{\pi}\,\sigma\,n^2\,T^4 \tag{2.17}$$

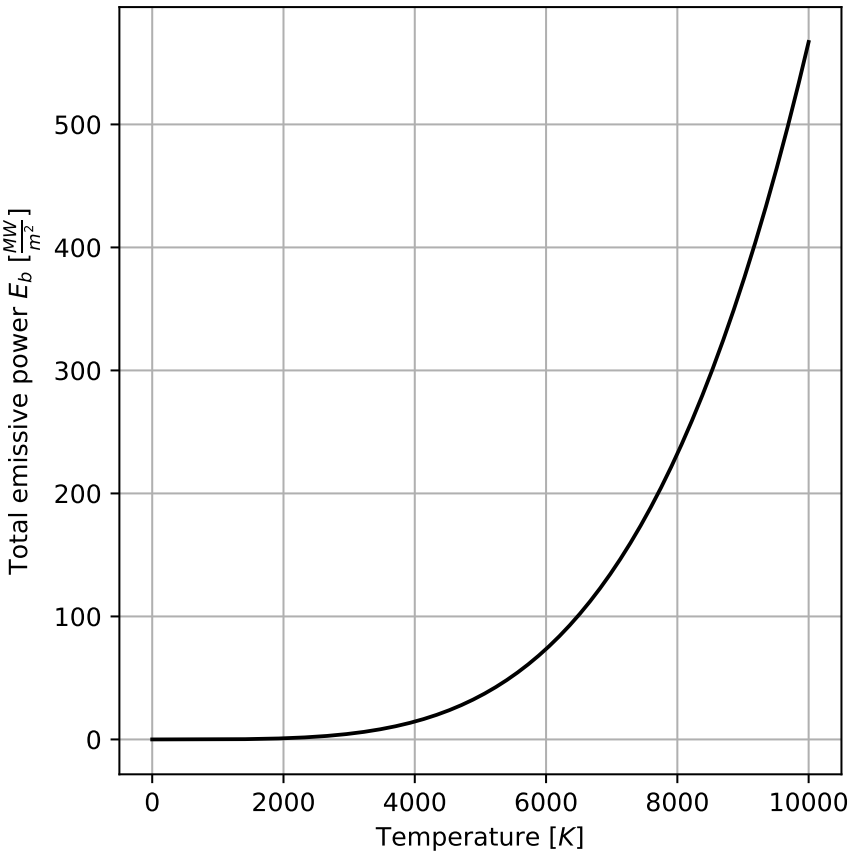

Figure 11 – Plot of Stefan-Boltzmann's law.

2.4.5 Gray body emission

Realistically, true blackbodies do not exist, even though very good approximations do. Nevertheless, assuming that the radiative intensity is uniform in all directions, and that the emissive power is independent of the wavenumber, the emission of thermal radiation of a non-black objects can be modelled with the Stefan-Boltzmann Law but with the added generalization of a dimensionless coefficient known as the **emissivity** $0 \leq \epsilon \leq 1$:

$$E_b = \epsilon \sigma n^2 T^4. \tag{2.18}$$

When $\epsilon = 1$, the body is said to be perfectly black. Otherwise, for values of $\epsilon > 0$, a body is said to be **gray**. By virtue of not being perfectly black, bodies with $\epsilon \neq 1$ do not absorb all incident radiation. Therefore, for the thermal equilibrium described in Section 2.4.1 to be satisfied, it must emit less radiation than a blackbody: the less energy it absorbs, the less energy it emits, hence $\epsilon < 1$. Equation 2.5 can likewise be applied to determine the radiative intensity emitted by a gray body:

$$I_b = \frac{1}{\pi}\epsilon\sigma n^2 T^4. \tag{2.19}$$

2.5 Radiative interactions

As radiation travels, it may interact with its medium or with other bodies according to their **radiative properties**. These properties depend on the kind of material within the medium, which for example could be gases, like CO_2, N_2 and H_2O, or particle clouds like soot. These properties are also dependent on the wavenumber η, as well as the pressure or temperature of the medium or physical body. An illustration of the different radiative phenomena discussed in this section, which are described by these radiative properties, can be viewed in Figure 12.

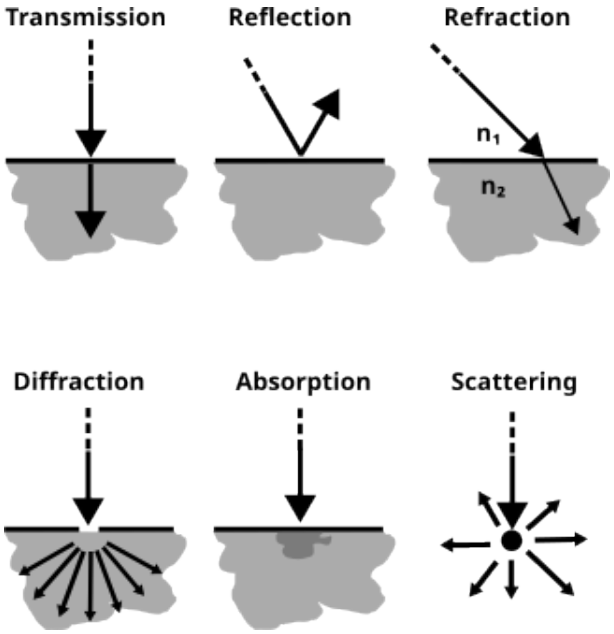

Figure 12 – Illustration of different physical phenomena that electromagnetic radiation exhibits. Figure adapted from Polyzos (2018).

2.5.1 Transmission

Transmission refers to when a beam of radiation is able to pass through a region without being deviated or absorbed. In other words, it is the capacity of the beam maintaining its original trajectory and energy. When analysing surfaces, the **transmissivity** τ_t, a dimensionless number between 0 and 1, is commonly employed to describe it.

2.5.2 Absorption

In the case of thermal energy, absorption refers to the process where radiation is transformed into the internal energy of a body. When analysing the absorption of

radiation by a surface, the **absorptivity** α, a dimensionless value bounded between 0 and 1, is commonly used. In rigour, the absorptivity of a surface may vary with both wavelength and angle of incidence to the surface (i.e. the beam's direction); however, models which consider a constant absorptivity in all directions and wavelengths may be applied for simplicity. There is an entire field of study dedicated to characterizing surfaces, including their absorptivity.

In the case of a continuous media, the absorption coefficient κ with dimension $[L^{-1}]$ is utilized instead to describe how the beam may be absorbed by the media as it crosses through it.

2.5.3 Reflection

Reflection happens when radiation does not cross the boundary between two different media and is instead redirected to a direction away from it. The capacity of a body's surface to reflect radiation is defined as the **reflectivity** ρ.

Reflection can be **specular** or **diffuse**. In the former, all incoming rays that are parallel to each other are kept parallel after they are reflected. In diffuse reflection, they are instead sent towards different directions to each other and are spread uniformly. The differences of these reflection processes can be visualized in Figure 13. This differentiation is especially important when defining boundary conditions for the radiative transfer, as walls can be either diffusively reflecting or specular, with the latter being harder to model due to its directional effects.

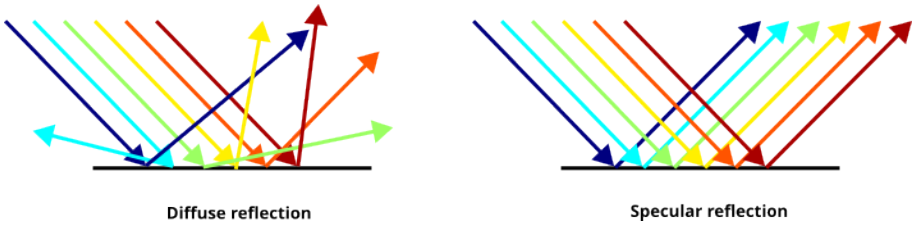

Figure 13 – Diffusive vs specular reflection.

2.5.4 Diffraction

Diffraction is when a beam of radiation is scattered towards other directions when encountering an obstacle, effectively bending around it. A good example of such obstacle is an aperture with similar wavelength to the beam that crosses it. It is a property common to any wave.

2.5.5 Refraction

Refraction happens when a beam of radiation crosses between media with different refractive indices n. Instead of passing through it unaltered, it instead changes directions

following Snell's Law.

2.5.6 Scattering

Scattering is an umbrella term for any process that may alter a radiation beam's direction. In a continuous medium, it can be understood as a combination of reflection, diffraction and refraction happening all at once at a particular point, the effect of which can be summarized by a **scattering coefficient** $\sigma_{s,\lambda}$, with dimension $[L^{-1}]$, and a phase function Φ. The phase function depends on the directional properties of the scattering process being analysed; for example, it may be modelled as isotropic, where $\Phi = 1$, or as anisotropic, where Φ is described by various models such as Mie and Rayleigh anisotropic scattering. The presence of particulate in a media, like soot or water droplets, are known for their strong scattering effects.

2.5.7 Extinction

Extinction is defined as the loss of radiative intensity in a given direction $\hat{s}$. It is the combined effect of absorption and out-scattering, the latter of which refers to beams that went out of said direction $\hat{s}$ and towards a new direction $\hat{s}'$. For a continuous media, the extinction coefficient can be defined as:

$$\beta = \kappa + \sigma_s. \tag{2.20}$$

2.5.8 Optical thickness

It is a dimensionless number that measures how intensely radiation interacts as it crosses an environment, and is defined as:

$$\tau = (\kappa + \sigma_s) \cdot L, \tag{2.21}$$

where L is a characteristic length. The higher the optical thickness, the "more participating" the medium is. A common range of optical thicknesses is described by Rodrigues (2023):

- **Non-participating or transparent medium** ($\tau = 0$): In this case, radiation is simply exchanged between the surfaces of the environment, and does not interact with the medium;
- **Optically thin medium** ($\tau << 1$): The medium has some interaction with radiative transfer, but it is not very strong;

- **Auto absorbing medium** ($\tau \approx 1$): It is neither too large, nor too small, being more mathematically complex. Many practical problems have this kind of optical thickness;
- **Optically thick medium** ($\tau >> 1$): In this case, radiative transfer is quite localized and is more similar to a diffusion process, like heat conduction.

For the sake of an example, we can compare how visible light behaves when it crosses the atmosphere with how it behaves inside the ocean. The ocean's optical thickness is considerable, to the point where it gets dark in shallow depths. The atmosphere, on the other hand, is optically thin, to the point where one can see the outer space through it.

2.5.9 Scattering albedo

It is a dimensionless number that measures how strong the scattering of a medium is relative to its extinction coefficient:

$$\omega = \frac{\sigma_s}{\kappa + \sigma_s}. \tag{2.22}$$

The combination of the optical thickness and scattering albedo is enough to describe the radiative properties of a system in terms of dimensionless numbers, and this pair may instead be used in place of the absorptivity κ and scattering coefficient σ_s, which have a dimension.

2.5.10 Emission

It relates to the capacity of a body to emit radiative energy. As mentioned in the previous section, it can be measured by the emissivity ϵ.

2.5.11 Kirchhoff's Law

Kirchhoff's law may be deduced from the Second Law of Thermodynamics and is generally applicable to radiative heat transfer analysis. It states that the radiative energy emitted by a body in thermodynamic equilibrium is equal to the radiative energy it absorbs.

One of its application is in surface radiation analysis. Suppose that a body's surface is described by a global absorptivity α and a global emissivity ϵ, which measure the total energy from all wavelengths and directions that is, respectively, absorbed and emitted. If the surface is in thermal equilibrium with its surroundings, then:

$$\alpha = \epsilon \text{ (Thermodynamic equilibrium)}. \tag{2.23}$$

2.5.12 Dimensionless numbers

Apart from the optical thickness and scattering albedo, there are other dimensionless numbers for characterizing radiative heat transfer in a system. Specifically, the **Stark number**, also known as radiation-conduction parameter (Snyder, 2002), and the Planck number (Yücel; Acharya; Williams, 1989), measure the relative importance of radiative heat transfer when compared with other modes of heat transfer. Howell, Mengüç and Siegel (2015) defines the former as:

$$N_C = \frac{k\beta}{4\sigma T_0^3}, \tag{2.24}$$

where k is the thermal conductivity, β is the extinction coefficient, L is a characteristic length, T_0 is a characteristic temperature and σ is the Stefan-Boltzmann constant. Yücel, Acharya and Williams (1989) defines the Planck number as:

$$Pl = \frac{\frac{k}{L}}{4\sigma T_0^3}. \tag{2.25}$$

They also note that $N_C = \tau \cdot Pl$. Dombrovsky and Baillis (2010) also defines a **Boltzmann number** that relates the convective heat transfer with the radiative heat transfer:

$$Bo = \frac{\rho u c_p T_0}{\sigma T_0^4}. \tag{2.26}$$

Where ρ and c_p are the specific mass and heat capacity of the medium and u is the flow's velocity.

These numbers are quite important in problems with different modes of heat transfer and may be used, for instance, to evaluate if a given system has appreciable radiative heat transfer or if the other modes dominate.

2.5.13 Radiative description of a continuous medium

To characterize the radiative transport through a continuous media (e.g. a gas), all radiative interactions described above may be summarized in three distinct effects: **absorption**, **emission** and **scattering**. Absorption and scattering are measured, respectively, by the absorption coefficient κ and the scattering coefficient σ_s, as described in Sections 2.5.2 and 2.5.6. The emission is modelled by an adaptation of either Planck's law (for non-gray media, see Section 2.4.3) or Stefan-Boltzmann's law (for gray media, see Section 2.4.4).

The absorption, scattering and extinction coefficients κ, σ_s and β all have a unit of $[L^{-1}]$, typically m^{-1} in the international system of units (SI). Remember that Equation 2.21 describes a dimensionless number (τ) as a product of β and L. As L has units of $[L]$, then it follows that β, and thus κ and σ_s, must be $[L^{-1}]$. These coefficients are crucial for modelling the radiative energy balance in a continuous medium. Many gases have

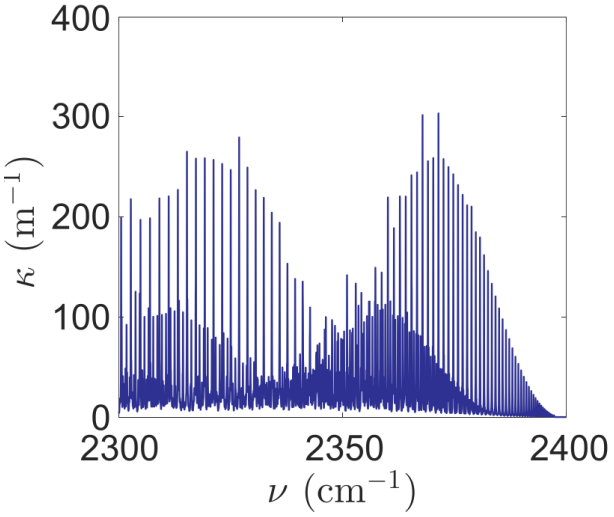

Figure 14 – CO_2 absorption coefficient measured at 1000 K and 0.1 bar of partial pressure in an atmosphere of 1 bar. Figure taken from HITRAN 2012 database and adapted from Rodrigues (2023).

had these properties measured and tabulated databases such as HITRAN. Figure 14 shows the absorption coefficient of CO_2 at given thermodynamic conditions.

2.5.14 Radiative description of a surface

A beam of radiation incident on a surface may undertake three main processes: it can be **absorbed**, **reflected** or simply be **transmitted** through it. As discussed previously, each of these processes may be correlated to the absorptivity α, the reflectivity ρ and the transmissivity τ_t, respectively, and are shown in Figure 15. All of these parameters are dimensionless numbers that may vary according to the direction and wavelength of the beam. For the sake of this analysis, global parameters that describe the contribution of all wavelengths and directions will be considered for simplicity.

Conservation of energy states that these parameters are bounded by the following equation:

$$\alpha + \tau_t + \rho = 1. \tag{2.27}$$

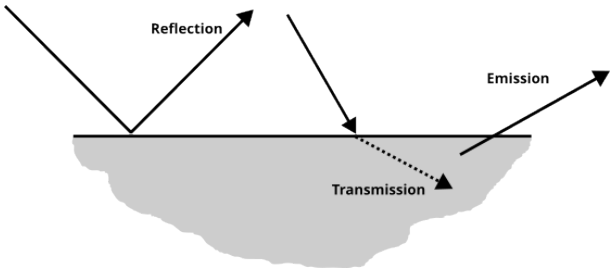

Figure 15 – Illustration of the radiative energy balance in a surface.

A few notable cases can be listed, as discussed by Rodrigues (2023):

- **Transparent surface:** when all radiation incident on a surface is transmitted, that is, when $\tau_t = 1$;
- **Opaque:** when all radiation striking a surface is either reflected or absorbed, i.e. $\tau_t = 0$;
- **Black**: when all radiation incident on a surface is absorbed, and therefore $\alpha = 1$.
- **Thermal equilibrium:** In this situation, the body must emit as much energy as it absorbs, as per Equation 2.23, so therefore $\epsilon = \alpha$.

The modelling of radiative exchange on surfaces is fundamental for defining boundary conditions in radiative transfer problems.

2.5.15 Gray and non-gray media

One way of simplifying radiative transfer analysis is by assuming that the radiative field does not change much with the wavenumber. Of course, this is an approximation, but it yields simpler models that are easier to understand and work with. When a medium or a body is assumed to behave the same for the entire electromagnetic spectrum they are called **gray**. In contrast, **non-gray** media or bodies behave differently for different parts of the electromagnetic spectrum.

Usually, in practical problems, gray approximations provide inaccurate results. On the other hand, representing the entire electromagnetic spectrum (as done in the line-by-line, or LBL, method) is computationally expensive (very much so) and thus has limited applications. This is similar to Direct Numerical Simulations (DNS) in computational fluid dynamics. A third option is to model the spectral behaviour of non-gray gases such that directly integrating the entire spectrum is avoided, as is done in models such as the Weighted Sum of Gray Gases (WSGG) or Full-Spectrum K-Distribution (FSK). These models seek to provide a reduced spectral domain that is appreciably accurate while being cost-viable. However, developing such models is a complicated task and there is a considerable amount of on-going research with this objective. Bibliographic review and discussion on these models is provided in Section 3.8.

3 The Radiative Transfer Equation

This chapter presents the general formulation for radiative energy transfer, in the form of a Partial Differential Equation (PDE) known as the Radiative Transfer Equation (RTE). It then follows on its discretization in the spatial domain via the Finite Volumes Method (FVM) and in the spatial domain by means of the Discrete Ordinates Method (DOM) or the Finite Angles Method (FAM). It then discusses the modelling of its spectral dimension, solver techniques and coupling with CFD.

3.1 Introduction

As stated previously, radiative heat transfer can be thought of as a thin, concentrated beam of electromagnetic radiation moving in a certain direction $\hat{s}$. As it crosses through a medium, it may be absorbed or scattered by it. This same medium also emits radiation. In order to mathematically express these phenomena, an infinitesimal control volume ds can be defined around this beam and a balance of its radiative intensity can be established inside of it, as seen in Figure 16. This balance makes up what is known as the **Radiative Transfer Equation**, or simply RTE for short. There are many ways to model the balance of radiative intensity; a relatively general formulation, that is suitable for many practical radiative heat transfer problems, including combustion processes, is shown below:

$$\underbrace{\frac{1}{c}\frac{\partial I(\vec{x},\hat{s},\eta,t)}{\partial t}}_{accumulation}+\underbrace{\frac{\partial I(\vec{x},\hat{s},\eta,t)}{\partial s}}_{transmission}=\underbrace{-\beta I(\vec{x},\hat{s},\eta,t)}_{extinction}+\underbrace{\kappa I_b(\vec{x},\eta,t)}_{Planck's\ law}+\underbrace{\frac{\sigma_s}{4\pi}\int_{\Omega} I(\vec{x},\hat{s}',\eta,t)\ \Phi(\hat{s}',\hat{s})\ d\Omega'}_{in-scattering}. \tag{3.1}$$

Where c is the speed of light, I is the radiative intensity of the beam, $\vec{x}$ is the spatial position of the beam, $\hat{s}$ is the beam's direction, η is its wavenumber, t is time, β is the extinction coefficient (Subsection 2.5.7), κ is the absorption coefficient (Subsection 2.5.2), I_b is the irradiation of the medium described according to Planck's Law (Subsection 2.4.3), σ_s is the scattering coefficient, Ω is the entire domain of $\hat{s}$ (which corresponds to the unit sphere), and Φ is the phase function. $\frac{1}{c}\frac{\partial I(\vec{x},\hat{s},\eta,t)}{\partial t}$ is an accumulation term, representing how the radiative intensity balance changes over time. For many practical applications, such as combustion systems commonly studied in engineering, it can be safely discarded, as radiation propagates so fast that it can be thought of as instantaneous compared to other processes. Thus, a steady state solution is enough.

$\frac{\partial I(\vec{x},\hat{s},\eta,t)}{\partial s}$ represents how much radiative intensity is transmitted through the infinitesimal control volume ds. Further in this text, it will be shown that this term is

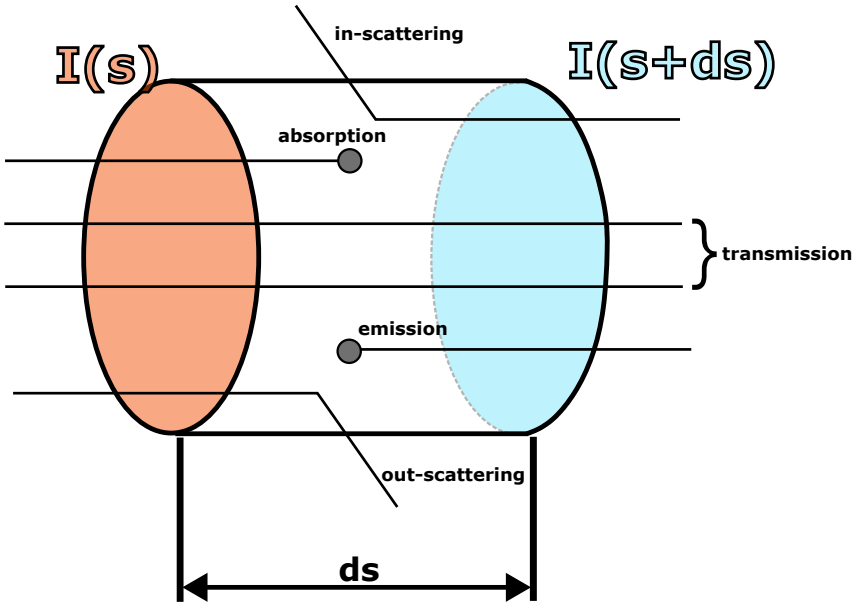

Figure 16 – Infinitesimal control volume for the RTE equation balance.

mathematically equivalent to an advection. $-\beta I(\vec{x}, \hat{s}, \eta, t)$ is the extinction term, representing how much radiative intensity is absorbed or out-scattered from the direction $\hat{s}$, thus diminishing the transmitted intensity of this particular beam. $\kappa I_b(\vec{x}, \eta, t)$ is a source term that represents the media's own emission of thermal radiation, as prescribed by Prévost's law (Section 2.4.1). In the formulation given in this work, it is assumed to be described by Planck's Law (Subsection 2.4.3) and, as a consequence, it is not a function of the direction $\hat{s}$ but it is a function of the media's temperature (represented here indirectly by the coordinates $\vec{x}$ and t, of which the temperature field is a function of). $\int_\Omega I(\vec{x}, \hat{s}', \eta, t)\ \Phi(\hat{s}', \hat{s})\ d\Omega'$ is an integral over all possible angular directions $\hat{s}' \in \Omega$ that cross the beam, which is fixed at a given position $\vec{x}$ and direction $\hat{s}$. It results in the total amount of radiative intensity that is in-scattered towards the beam's direction $\hat{s}$, therefore increasing the total amount of transmitted radiative intensity. This term couples all angular directions together. $\Phi(\hat{s}', \hat{s})$ is known as the phase function, which informs how much radiative intensity from direction $\hat{s}'$ is scattered towards $\hat{s}$.

The RTE as prescribed above assumes that the medium is continuous with a constant index of refraction n throughout and neglects polarization effects. It also neglects interactions in the spectral dimension η, as may happen with Raman scattering or fluorescence. Most importantly, it uses the **local thermodynamic equilibrium (LTE)** assumption, which considers that the emission of radiation is given by $dI_{e,\eta} = \kappa I_{b,\eta}\ ds$. This is reasonable in many combustion systems, such as industrial boilers, and is commonly adopted by books such as Howell, Mengüç and Siegel (2015) and Modest and Mazumder (2022).

A couple other simplifications are in order. First, the temporal dependency can, for most problems, be safely neglected, as the photons carrying thermal energy propagate

much faster than the typical time scales associated with changes in other physical properties (such as temperature, pressure, density and species fractions), which means that the domain's radiative properties (absorption and scattering), as well as its radiative emissions, also update very slowly, given they're a function of the former. In practical simulations, it is common to not update the radiative field on every time step, but only after a set number of CFD time-steps, which further illustrates this difference in time scales. Another possible simplification is to establish that the radiative intensity field I and the radiative properties (κ and σ_s) do not depend on the wavenumber; such model implies that the media is **gray**. As the media is usually a gas in radiative heat transfer for CFD problems, this is also commonly referred to as a **gray gas model**. This simplification avoids having to integrate the RTE over the electromagnetic spectrum, which is costly and complicated. Section 3.8 is dedicated to strategies to model the spectral dependency of the RTE; for now, we shall simply add the subscript η to imply that the RTE is being solved for only the wavenumber η, which is mathematically identical to a gray media model as long as there is no spectral coupling (which is assumed). Therefore, the solution of several such equations (each representing a **band**) may then be numerically integrated to obtain the correct non-gray solution.

All of the above leads to the following simplified version of the RTE:

$$\frac{dI_\eta(\vec{x},\hat{s})}{ds} = -\beta_\eta I_\eta(\vec{x},\hat{s}) + \kappa_\eta I_{b,\eta}(\vec{x}) + \frac{\sigma_{s,\eta}}{4\pi}\int_\Omega I_\eta(\vec{x},\hat{s}')\ \Phi(\hat{s}',\hat{s})\ d\Omega'. \tag{3.2}$$

The equation above is formulated in terms of the differential segment ds, which describes the energy balance of a given beam of radiative energy along an infinitesimal path in space. It is ideal for models such as the Monte Carlo Method or the Ray Tracing Method, which follow the trajectory of such beams throughout space to determine the radiative heat transfer. Other models, such as the Discrete Ordinates Method (DOM) or the Finite Angles Method (FAM), define a discrete set of directions, each of which represent the average intensity over a solid angle, and then determine the intensity of each direction in each spatial node. A good analogy would be that methods such as Monte Carlo are Lagrangian-like, while DOM and FAM are Eulerian-like. For the latter, the divergent form of the RTE is more natural. We can obtain it by first applying the following identity:

$$\frac{dI}{ds} = (\hat{s}\cdot\nabla)I. \tag{3.3}$$

As $\hat{s}$ is constant, it can also be written as:

$$(\hat{s}\cdot\nabla)I = \nabla\cdot(I\hat{s}), \tag{3.4}$$

where $\hat{s}$ is the unit vector that represents the beam's direction, $(\hat{s}\cdot\nabla)I$ is the scalar product of the gradient of I by $\hat{s}$ and $\nabla\cdot(I\hat{s})$ is the divergent of $I\hat{s}$. Thus, we have:

$$\nabla \cdot (I_\eta(\vec{x}, \hat{s})\ \hat{s}) + \beta_\eta I_\eta(\vec{x}, \hat{s}) = \kappa_\eta I_{b,\eta}(\vec{x}) + \frac{\sigma_{s,\eta}}{4\pi} \int_{4\pi} I_\eta(\vec{x}, \hat{s}')\ \Phi(\hat{s}, \hat{s}')\ d\Omega'. \tag{3.5}$$

Equation 3.5 is equivalent to Equation 3.2 and is established for one of the infinitely many beams present in the domain. It can be noticed that the term $\nabla \cdot (I_\eta\, \hat{s})$ is mathematically equivalent to an advection term, where $\hat{s}$ is similar to a velocity, meaning that, for a fixed direction $\hat{s}$, the RTE may be interpreted as describing an advection of sorts.

This form of the RTE can then be readily discretized, a process which can be split in two main components: the spatial discretization and the angular discretization. The spatial discretization of the RTE can be done with the usual methods used in continuum mechanics, such as finite elements or finite volumes. The angular discretization refers to the directional component $\hat{s}$ of the RTE, and consists of discretizing the angular domain into a finite number of beams.

To close Equation 3.5, boundary conditions need to be specified. In this work, we will follow with the assumption that the boundary of the domain consists of opaque walls which emit and reflect light diffusively in all directions. Local thermodynamic equilibrium is also assumed. Thus, the **diffusively emitting and reflecting opaque surface boundary condition** is defined:

$$I_{w,\eta}(\vec{x}, \hat{s}) = \epsilon_\eta(\vec{x}) I_{b,\eta}(\vec{x}) + \frac{\rho_\eta(\vec{x})}{\pi} \int_{\hat{n}\cdot\hat{s}<0} I_\eta(\vec{x}, \hat{s}')|\hat{n}_w \cdot \hat{s}'|\ d\Omega',\ \forall \hat{s} : \hat{s} \cdot \hat{n}_w > 0, \tag{3.6}$$

where $I_{w,\eta}$ is the radiative intensity at the position $\vec{x}$ pointing towards $\hat{s}$, ϵ_η is the wall's emissivity, ρ_η is the wall's reflectivity and $\hat{n}_w$ is the wall's normal vector. As it is assumed that the wall is opaque and there is local thermodynamic equilibrium in it, then Kirchhoff's law (Equation 2.23) applies and thus the following identity follows from Equation 2.27:

$$\epsilon + \rho = 1. \tag{3.7}$$

This boundary condition can be hard to understand, as it does not fit the mould of a typical Dirichlet, Neumann or Robin type boundary condition that one may expect. For numerical implementation purposes, Equation 3.6 could be understood as a kind of Dirichlet boundary condition, where a radiative intensity is prescribed only to rays that are outgoing ($\hat{s} \cdot \hat{n} > 0$) relative to the surface. Incoming rays are simply reflected by the surface and are used to define the radiative intensity of the outgoing rays. In other words, as long as $\rho_\eta \neq 0$ (i.e. not a black surface), the angular directions are coupled at the boundary. Numerically, this can be dealt with an iterative algorithm, where the radiative

intensity field for each direction is first solved separately, yielding how much radiation will be reflected at each boundary and thus allowing the integral of Equation 3.6 to be solved. The boundary conditions are then updated and the new radiative intensity field is calculated again. This process repeats until the radiative intensity converges. A similar iterative process can be performed to deal with the coupling caused by the integral term of the RTE (Equation 3.5).

For the incoming directions relative to the wall, no calculation is needed to be performed, and thus these boundaries can be ignored. Certain algorithms (like RTS) may store a value for these intensities at the boundary by considering that the radiative intensity at the boundary's centroid is equal to the intensity at the cell's centroid. Both approaches may be understood as applying a zero Neumann boundary condition:

$$\nabla I_{\eta,w} \cdot \hat{n}_w = 0. \tag{3.8}$$

Where $\hat{n}_w$ is the surface's normal vector and $\nabla I_{\eta,w}$ is the radiative intensity gradient at the surface. The boundary condition given by Equation 3.6 suffices to close the problem at hand, is good enough for many engineering applications and is currently implemented in RTS. Other boundary condition types, such as boundaries that have specular reflection or consider semi-transparent boundaries are unavailable, but are a possible addition. A good summary on RTE boundary conditions can be seen on Coelho (2012). An important point to note is that free surfaces (which the author calls open boundaries) can be modelled as black walls.

The field for which the RTE is solved for, the radiative intensity I, is not very interesting by itself. Post-processing of the RTE results is commonly done both for visualizing its results and also for coupling the radiative transfer with CFD solvers. This is done by means of a couple of derived fields that are calculated from I. These are, as defined in Modest and Mazumder (2022):

$$G_\eta(\vec{x}) = \int_\Omega I_\eta(\vec{x}, \hat{s})\ d\Omega \qquad \text{(Incident radiation)}, \tag{3.9}$$

$$\nabla \cdot \vec{q}_{\,rad,\eta}(\vec{x}) = \kappa\,[I_{\eta,b}(\vec{x}) - G(\vec{x})] \qquad \text{(Divergent radiative heat flux)}, \tag{3.10}$$

$$\vec{q}_{\,\eta} = \int_\Omega \hat{s}\ I_\eta(\vec{x}, \hat{s})\ d\Omega \qquad \text{(Radiative heat flux vector)}, \tag{3.11}$$

$$q_{\eta,w} = \hat{n}_w \cdot \vec{q}_{\,\eta} \qquad \text{(Radiative heat flux through a surface with normal } \hat{n}_w\text{)}. \tag{3.12}$$

The following sections will discretize the RTE both in the spatial and angular domains. The spatial domain will be discretized with the Finite Volumes Method. The angular

domain discretization will be described for both the the Discrete Ordinates Method and the Finite Angles Method. The resulting computational domain may be thought of as a series of partial differential equations, one for each direction, that describe an advective transport and compose a discrete domain similar to the one illustrated in Figure 17. If the spectral domain is considered (i.e. gray media model is not applied), then the domain resembles the one illustrated in Figure 18.

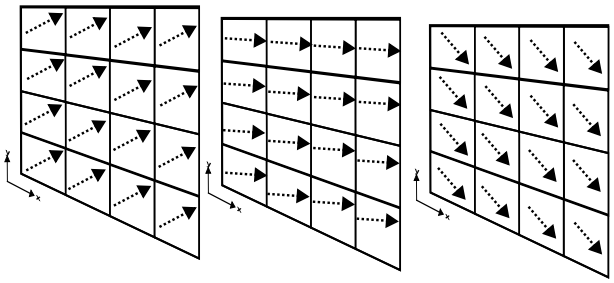

Figure 17 – Illustration of the domain of the discretized RTE when the gray model is applied. Each rectangle represents the spatial domain for a given direction.

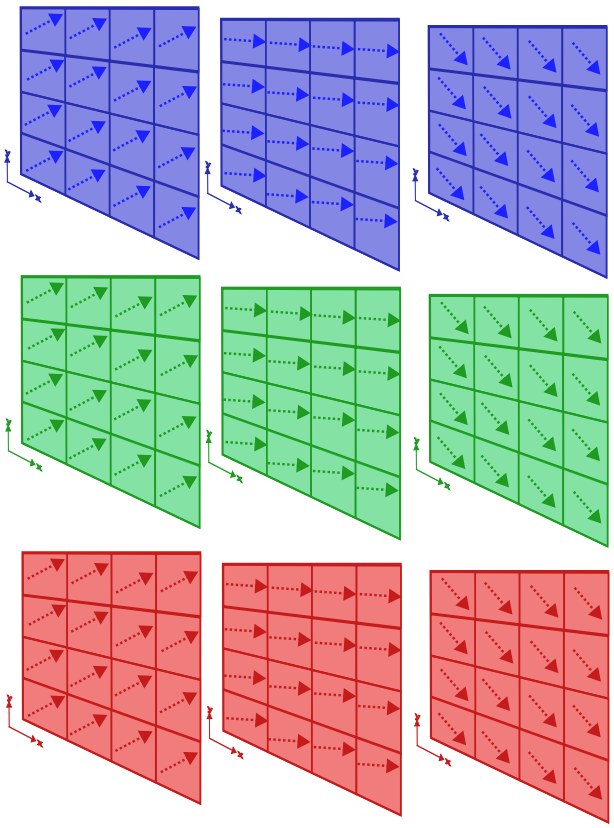

Figure 18 – Illustration of the domain of the discretized RTE in a non-gray media. Each rectangle represents the spatial domain for a given direction, and each colour represents a given band.

3.2 The Finite Volumes Method for Spatial Discretization

We shall discretize Equation 3.5 spatially with the Finite Volumes Method, which is used by both MFSim and RTS. This discretized form will serve as a good basis for applying the angular discretization. Integrating Equation 3.5 in a generic discrete volume V yields:

$$\int_V \nabla \cdot (I_\eta \ \hat{s}) \ dV + \int_V \beta_\eta I_\eta \ dV = \int_V \kappa_\eta I_{b,\eta}(\vec{r}) \ dV + \int_V \frac{\sigma_{s,\eta}}{4\pi} \int_{4\pi} I_\eta \Phi(\hat{s}, \hat{s}') \ d\Omega' \ dV. \quad (3.13)$$

From here, we assume that the value of a field $f(\vec{x})$ on the cell's centroid times its volume is approximately equal to the integral of this field over the volume. Mathematically, this can be expressed by:

$$\int_V f(\vec{x}) \ dV \approx f(\vec{x}_P) \cdot \Delta V = f_P \cdot \Delta V. \quad (3.14)$$

It is also fundamental to apply Gauss's Theorem on the divergence terms of the PDE, transforming them into surface integrals:

$$\int_V \nabla \cdot \vec{g}(\vec{x}) \ dV = \int_A \vec{g}(\vec{x}) \cdot \hat{n} \ dA. \quad (3.15)$$

Since it is assumed that the cells of a finite volume method mesh are all convex polyhedra with a finite number of faces, Equation 3.15 can be written as:

$$\int_A \vec{g}(\vec{x}) \cdot \hat{n} \ dA = \sum_f \int_{A_f} \vec{g}(\vec{x}) \cdot \hat{n} \ dA. \quad (3.16)$$

Again, we assume that the value of field $\vec{g}(\vec{x})$ in the centroid of face A_f, which may be defined as $\vec{g}(\vec{x}_f)$, will be approximately equal to the integral average of the same field in this face. That is:

$$\int_{A_f} \vec{g}(\vec{x}) \cdot \hat{n} \ dA \approx \vec{g}(\vec{x}_f) \cdot \hat{n} \ \Delta A_f = g_f \cdot \hat{n} \ \Delta A_f. \quad (3.17)$$

Thus, Equation 3.13 becomes:

$$\sum_f (I_{\eta,f} \ \hat{s}) \cdot (\Delta A_f \ \hat{n}_f) + \beta_{\eta,P} I_{\eta,P} \ \Delta V_P = \kappa_{\eta,P} I_{b,P} \ \Delta V_P + \frac{\sigma_{s,\eta,P}}{4\pi} \Delta V_P \int_\Omega I_P(\hat{s}') \Phi(\hat{s}', \hat{s}) \ d\Omega' \ . \quad (3.18)$$

It is common practice to group the emission and in-scattering terms together into a single source term $S_M(\vec{x}, \eta)$:

$$S_M = \kappa_{\eta,P} I_{b,\eta,P} \ \Delta V_P + \frac{\sigma_{s,\eta,P}}{4\pi} \Delta V_P \int_\Omega I_{\eta,P}(\hat{s}') \Phi(\hat{s}', \hat{s}) \ d\Omega'. \quad (3.19)$$

Applying Equation 3.19 yields:

$$\sum_f (I_{\eta,f}\ \hat{s}) \cdot (\Delta A_f\ \hat{n}_f) = -\beta_{\eta,P} I_{\eta,P}\ \Delta V_P + S_M. \tag{3.20}$$

Equation 3.20 is a common manner to write the Radiative Transfer Equation discretized with the Finite Volumes Method, and is readily applicable to all types of meshes. To complete it, however, we still need a way to determine the values of $I_{\eta,f}$, contained in a face centroid, given that the field I is only stored in the centroid of the computational cells. To do this, an interpolation method needs to be chosen. Modest and Mazumder (2022) has an in-depth discussion on different interpolation schemes for this purpose. In computational models of the RTE, the **first order upwind** scheme (commonly referred to as the **step scheme**, or simply as upwind) is widely used.

Usually, the upwind scheme yields good results, but due to being a first order method, it may not be as accurate as more sophisticated methods. Nevertheless, it represents the physics of this problem quite well; in fact, upwind is the standard discretization scheme in radiative transfer simulations and has widespread use across RTE solvers. In this work, the first-order upwind scheme is applied to discretize this term, unless specified. For future works, utilization of the **diamond scheme**, one of the best contenders for replacing the upwind scheme, might be an interesting endeavour.

Let's define the radiative intensity in the surface centroid $I_{\eta,f}$ in the following manner:

$$I_{\eta,f} = \alpha\ I_{\eta,U} + (\alpha - 1)\ I_{\eta,P}, \tag{3.21}$$

where $I_{\eta,U}$ is the radiative intensity of the upwind cell relative to the surface, $\vec{I}_{\eta,P}$ is the radiative intensity of the downwind cell relative to the surface and $\alpha \in [0, 1]$ is an interpolation parameter. If $\alpha = 1$, the first order upwind scheme is applied (Figure 19a); if $\alpha = 0.5$, the Central Difference Scheme (CDS) is applied (Figure 19b); finally, $\alpha = 0$ corresponds to a downwind method. It is recommended that $\alpha = 1$ be utilized, as discussed above. One may still want to set $\alpha = 0.5$, which is permissible, but may require even finer meshes and is not standard. Setting $\alpha < 0.5$ is ill-advised.

Modest and Mazumder (2022) proposes the following expression for the first order upwind scheme, which does not use conditionals and is adapted for all discrete directions $\hat{s}_i$:

$$(\hat{n}_f \cdot \hat{s}_i) I_{\eta,f,i} \approx \frac{|\hat{n}_f \cdot \hat{s}_i| + (\hat{n}_f \cdot \hat{s}_i)}{2} I_{\eta,P,i} - \frac{|\hat{n}_f \cdot \hat{s}_i| - (\hat{n}_f \cdot \hat{s}_i)}{2} I_{\eta,N,i}. \tag{3.22}$$

Where $I_{\eta,N,i}$ is the neighbouring cell that shares face f with the cell P in which the energy balance is established. We can mix Equation 3.22 with Equation 3.21 to get a more general expression:

$$(\hat{n}_f \cdot \hat{s}_i) I_{\eta,f,i} \approx \frac{(2\alpha - 1)\ |\hat{n}_f \cdot \hat{s}_i| + (\hat{n}_f \cdot \hat{s}_i)}{2} I_{\eta,P,i} - \frac{(2\alpha - 1)\ |\hat{n}_f \cdot \hat{s}_i| - (\hat{n}_f \cdot \hat{s}_i)}{2} I_{\eta,N,i}. \tag{3.23}$$

Equation 3.23 can be readily applied to a general Finite Volume problem, including those with unstructured meshes.

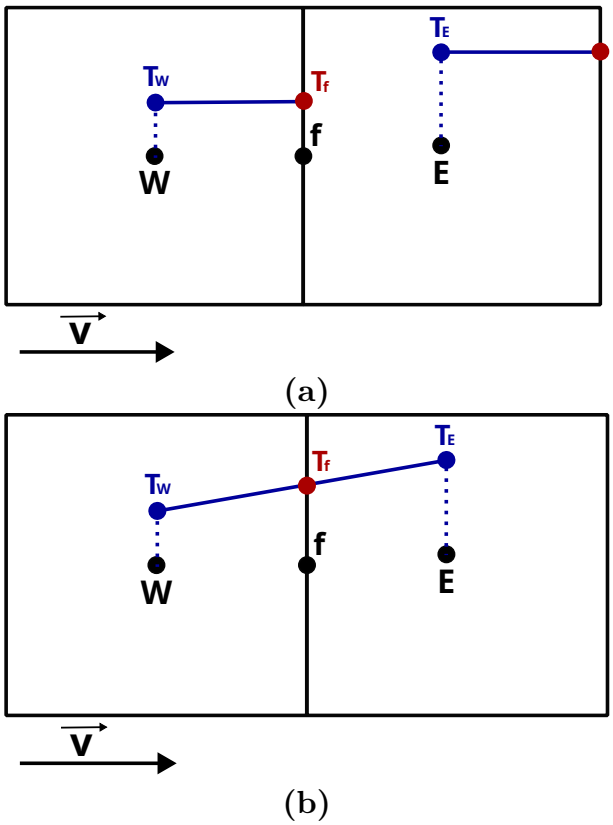

Figure 19 – Illustration of the first order upwind (a) and central difference (b) schemes.

3.3 The Discrete Ordinates Method

In the Discrete Ordinates Method (DOM), the unit sphere that represents the directional (or angular) domain of the RTE is discretized into a series of discrete ordinate directions $\hat{s}_i$ (thus the name), each of which has an associated weight w_i. The values of the directions $\hat{s}_i$ and weights w_i, as well as how many of them exist, are determined beforehand based on a discrete integral model for the unit sphere. Several such models exist and are commonly referred to as quadratures, such as the S_N, T_N and Q_N quadratures (Figures 20, 21 and 22), the three of which are implemented in RTS.

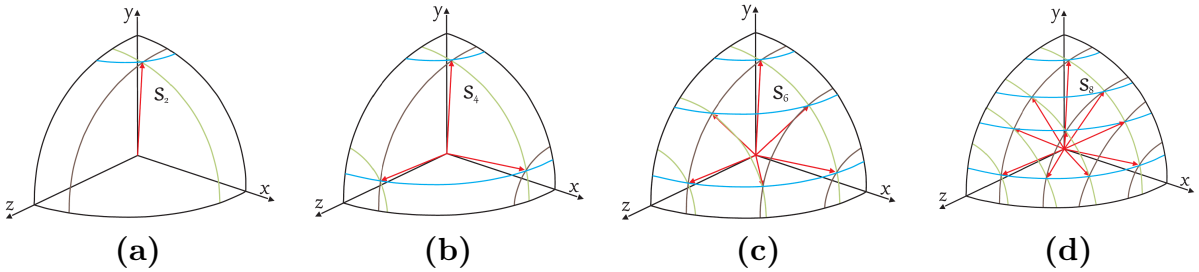

Figure 20 – Illustration of S_N quadrature set, taken from Rodrigues (2023).

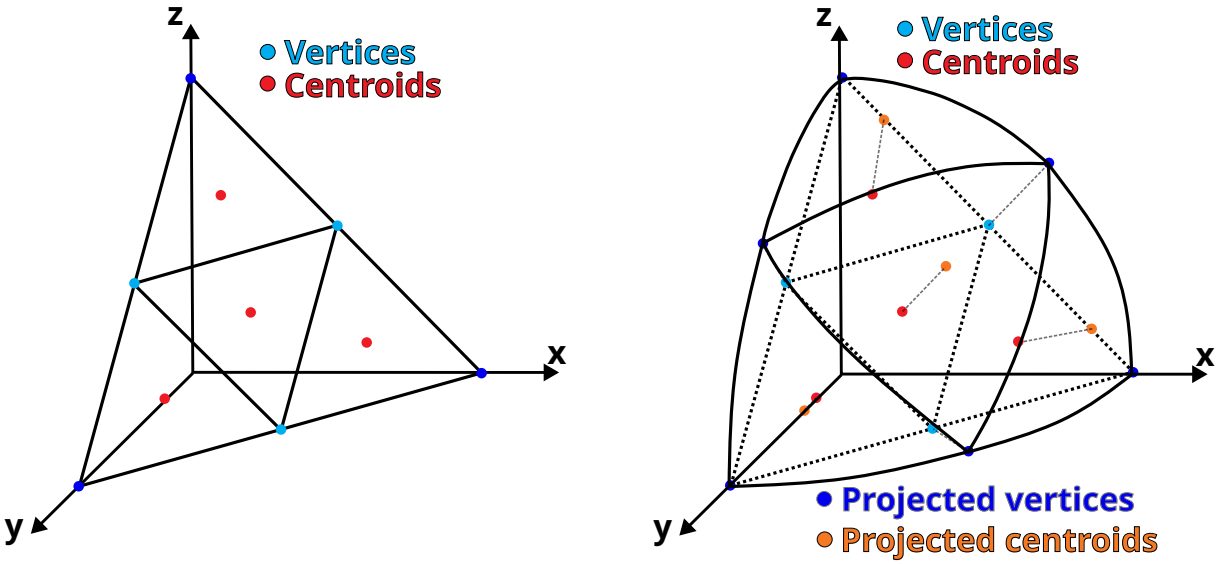

Figure 21 – Illustration of T_2 quadrature set. Figure adapted from Rodrigues (2023).

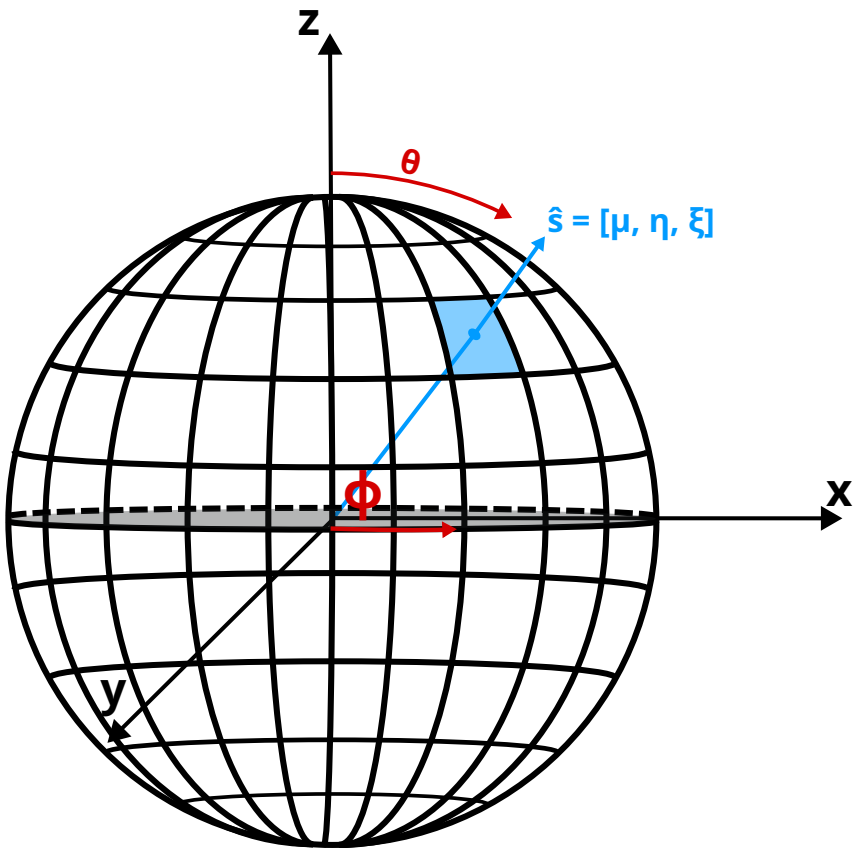

Figure 22 – Illustration of Q_N quadrature set. Figure adapted from Rodrigues (2023).

The DOM can be developed by starting with the discretization of the in-scattering integral:

$$\int_{\Omega} I_{\eta,P}(\hat{s}')\Phi(\hat{s}',\hat{s})\ d\Omega \approx \sum_{j} w_j I_{\eta,P}(\hat{s}_j)\Phi(\hat{s}_j,\hat{s}_i). \tag{3.24}$$

Equation 3.20 is transformed into a series of discrete PDEs, each representing a direction $\hat{s}_i$. Thus, we have:

$$\sum_f (I_{\eta,f,i}\ \hat{s}_i) \cdot (\Delta A_f\ \hat{n}_f) = -\beta_{\eta,P} I_{\eta,P,i}\ \Delta V_P + S_M, \tag{3.25}$$

where:

$$S_M = \kappa_{\eta,P} I_{b,P,i} \Delta V_P + \frac{\sigma_{s,\eta,P}}{4\pi} \Delta V_P \sum_j w_j I_{\eta,P}(\hat{s}_j) \Phi(\hat{s}_j, \hat{s}_i). \tag{3.26}$$

The boundary condition is also readily discretized:

$$I_{\eta,i,w} = \epsilon_{\eta,w} I_{b,w} + \frac{\rho_{\eta,w}}{\pi} \sum_{\hat{n}_w \cdot \hat{s}_j < 0} w_j I_{\eta,w,j} |\hat{n}_w \cdot \hat{s}_j|,\ \hat{n}_w \cdot \hat{s}_i > 0 \text{ (Outgoing rays)}. \tag{3.27}$$

The incident radiation, divergent radiative heat flux and radiative wall heat flux are given by:

$$G_{\eta,P} = \sum_i w_i I_{\eta,P,i} \qquad \text{(Incident radiation)}, \tag{3.28}$$

$$\nabla \cdot q_{rad,\eta,P} = \kappa_{\eta,P} I_{\eta,b,P} - G_{\eta,P} \qquad \text{(Divergent radiative heat flux)}, \tag{3.29}$$

$$q_{rad,\eta,w} = \hat{n}_w \cdot \sum_i w_i I_{i,\eta,w} \hat{s}_i \qquad \text{(Radiative wall heat flux)}. \tag{3.30}$$

Equations 3.25 through 3.30 are generic and serve as an interface for the chosen quadrature. Essentially, the quadrature model must inform the number of PDEs to be solved, as well as the direction unit vector $\hat{s}_i$ and weight w_i associated with each PDE. Once the quadrature is chosen, the discretization is finally complete and a linear system can then be defined from it.

The choice of quadrature model directly affects the result, as well as the computational cost. A number of models exist, with Modest and Mazumder (2022) implying that there is no universally optimal selection (the authors even characterize their choice as arbitrary). In other words, choosing the best quadrature may end up being a process of trial and error by the user and is dependant on the problem at hand and its geometry. Nevertheless, there are guidelines for producing good quadratures, such as the ones cited by Modest and Mazumder (2022):

- Display symmetry for any arbitrary rotation of $90°$;
- Satisfy the zeroth moment: $\int_\Omega d\Omega = 4\pi = \sum_i w_i$;
- Satisfy the first moment: $\int_\Omega \hat{s}\ d\Omega = \vec{0} = \sum_i w_i \hat{s}_i$;

- Satisfy the second moment: $\int_\Omega \hat{s}\hat{s}\ d\Omega = \frac{4}{3}\pi \overrightarrow{\overrightarrow{I_{id}}} = \sum_i w_i \hat{s}_i \hat{s}_i$, where $\overrightarrow{\overrightarrow{I_{id}}}$ is the identity tensor;
- Satisfy the first moment over a half range: $\int_{\hat{n}\cdot\hat{s}<0} |\hat{n}\cdot\hat{s}|\ d\Omega = \int_{\hat{n}\cdot\hat{s}>0} \hat{n}\cdot\hat{s}\ d\Omega = \pi = \sum_{\hat{n}\cdot\hat{s}_i>0} w_i\, \hat{n}\cdot\hat{s}_i$. This cannot be achieved for arbitrary orientations of the surface normal, but can be satisfied for the main Cartesian orientations (i.e. if $\hat{n} = \hat{i}$, $\hat{n} = \hat{j}$ or $\hat{n} = \hat{k}$).

Rodrigues (2023) also cites a series of conditions enumerated by Koch *et al.* (1995):

- All weighing factors w_i must be positive, minimizing numerical errors;
- The reciprocity principle, that is, $\Phi(\hat{s}', \hat{s}) = \Phi(\hat{s}, \hat{s}')$, must be preserved;
- The number of photons must be conserved, which leads to satisfying the following condition: $\sum_i w_i |\hat{s}_i \cdot \hat{n}| = 0$. This is similar to the first momentum condition;
- The quadrature must not have directional bias, that is, any rotation of the nodal points must not affect the result;
- Every nodal point $\hat{s}$ must have a corresponding opposite point (i.e. For all $\hat{s}$, $-\hat{s}$ must exist).

Overall, the DOM is quite competent at delivering high-accuracy results for a number problems of radiative heat transfer of varied complexity. It has, therefore, become a staple in radiative transfer solvers, particularly when coupled with CFD. It does, however, have a few drawbacks, such as:

- Poor convergence in optically thick or highly scattering media;
- Susceptibility to ray effects;
- Conservativeness in the angular direction is not strictly guaranteed, unlike in the Finite Volumes Method, which is guaranteed by the formulation.

Many attempts have been made to address these issues. For example, the Finite Angles Method is quite similar to the DOM, but has been observed to range from slightly better to noticeably better in terms of results and computational costs, depending on the problem (Modest; Mazumder, 2022). Nevertheless, the DOM is still competent and broadly used to this day.

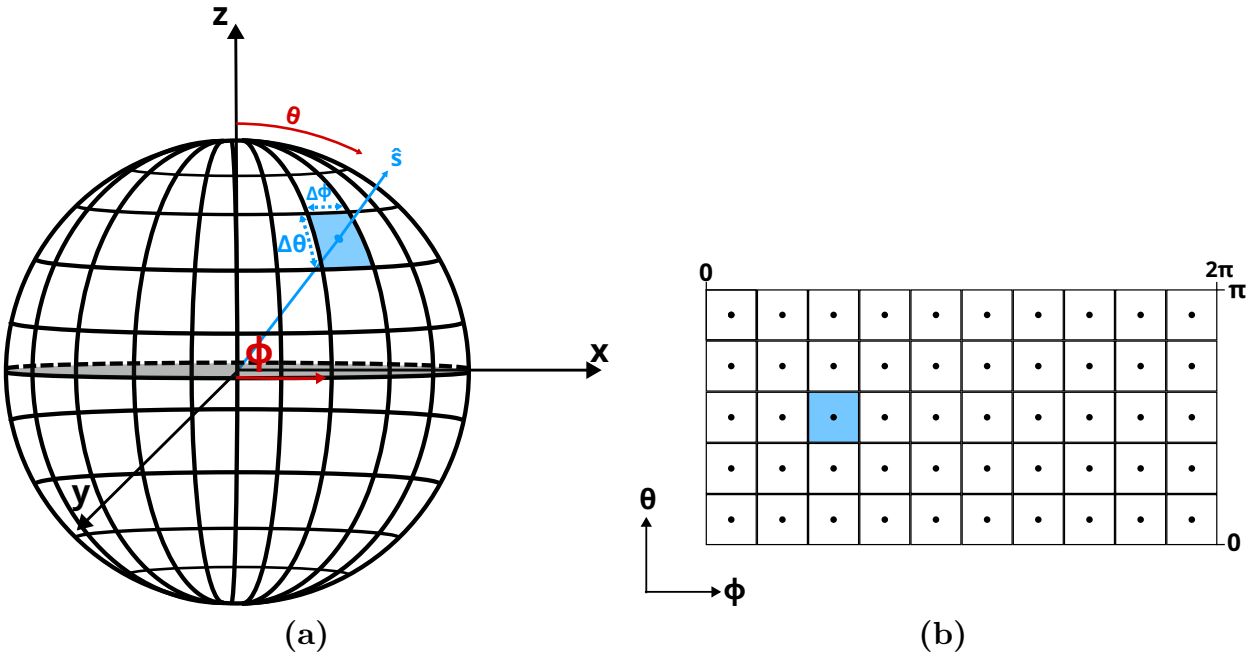

Figure 23 – Illustration of the regular FAM grid in the unit sphere (a) and an abstraction of its domain (b). Figure adapted from Rodrigues (2023).

3.4 The Finite Angle Method

The Finite Angle Method (FAM), also known as the Finite Volume Discrete Ordinates Method (FVDOM), is a method for discretizing the RTE. Like the DOM, it discretizes the unit sphere; however, instead of generating a finite number of points, each with weights associated with them, it instead tessellates the unit sphere into a finite number of solid angles. The RTE is, then, split into a system of coupled PDEs, each relating to one of the unit sphere's discrete solid angles. Likewise, the in-scattering integral is also split into a sum of the integrals over each solid angle. The RTE is then integrated not only on the spatial domain, but also on the angular domain that pertains to that discrete solid angle.

The meshing of the unit sphere can be both structured or unstructured, similarly to a 2D Cartesian plane. It is common, however, to utilize structured meshes, where the two angular directions θ and ϕ are split in equal intervals. In this case, the FAM mesh (Figure 23) is similar to the one applied to Q_N quadratures (Figure 22).

Taking Equation 3.20, the RTE is integrated over the i-th solid angle Ω_i:

$$\sum_f (\Delta A_f \ \hat{n}_f) \cdot \int_{\Omega_i} (I_{\eta,f} \ \hat{s}) \ d\Omega = \int_{\Omega_i} (-\beta_{\eta,P} I_{\eta,P} \ \Delta V_P + S_M) \ d\Omega, \tag{3.31}$$

where:

$$\int_{\Omega_i} S_M \ d\Omega = \kappa_{\eta,P} \ \Delta V_P \int_{\Omega_i} I_{b,P} \ d\Omega + \frac{\sigma_{s,\eta,P}}{4\pi} \Delta V_P \int_{\Omega_i} \int_{\Omega} I_{\eta,P}(\hat{s}') \Phi(\hat{s}', \hat{s}) \ d\Omega' \ d\Omega. \tag{3.32}$$

The in-scattering integral is discretized in the following way, which already takes into account that it is integrated again in the solid angle Ω_i:

$$\int_{\Omega_i}\int_{\Omega} I_{\eta,P}(\hat{s}')\Phi(\hat{s}',\hat{s})\ d\Omega'\ d\Omega \approx \sum_j \left[\int_{\Omega_i}\int_{\Omega_j} I_{\eta,P}(\hat{s}')\Phi(\hat{s}',\hat{s})\ d\Omega'\ d\Omega\right]. \tag{3.33}$$

The nodal value $I_{\eta,P}(\hat{s}'_j)$ is assumed to be the integral average of the radiative intensity:

$$I_{\eta,P}(\hat{s}'_j) \approx \frac{\int_{\Omega_j} I_{\eta,P}(\hat{s}')\,\Phi(\hat{s}',\hat{s})\ d\Omega'}{\int_{\Omega_j}\Phi(\hat{s}',\hat{s})\ d\Omega'}, \tag{3.34}$$

which then yields:

$$\int_{\Omega_j} I_{\eta,P}(\hat{s}')\Phi(\hat{s}',\hat{s})\ d\Omega' \approx I_{\eta,P}(\hat{s}_j)\int_{\Omega_j}\Phi(\hat{s}',\hat{s})\ d\Omega'. \tag{3.35}$$

Finally, as $I_{\eta,P}(\hat{s}_j) = I_{\eta,P,j}$ is constant in relation to Ω_i, we can write the fully discretized in-scattering integral as:

$$\sum_j \left[\int_{\Omega_i}\int_{\Omega_j} I_{\eta,P}(\hat{s}')\Phi(\hat{s}',\hat{s})\ d\Omega'\ d\Omega\right] \approx \sum_j I_{\eta,P,j}\int_{\Omega_i}\int_{\Omega_j}\Phi(\hat{s}',\hat{s})\ d\Omega'\ d\Omega. \tag{3.36}$$

The integrals over the phase function Φ can be performed analytically, tabulated and fed into the solver:

$$\int_{\Omega_i}\int_{\Omega_j}\Phi(\hat{s}',\hat{s})\ d\Omega'\ d\Omega = \bar{\Phi}_{j,i}. \tag{3.37}$$

With the in-scattering integral fully discretized, attention can be given to the integration on the face field:

$$\sum_f \Delta A_f \cdot \int_{\Omega_i}\left[I_{\eta,f}(\hat{s})\,(\hat{s}\cdot\hat{n}_f)\right]\ d\Omega. \tag{3.38}$$

Again, it is assumed that $I_{\eta,f}(\hat{s}_i)$ is the integral average of $I_{\eta,f}(\hat{s})$ throughout Ω_i and can, thus, be taken off the integral term, yielding:

$$\sum_f \Delta A_f \cdot I_{\eta,f,i}\int_{\Omega_i}(\hat{s}\cdot\hat{n}_f)\ d\Omega. \tag{3.39}$$

The integral above is then determined analytically, yielding the following term:

$$\hat{n}_f\cdot\vec{S}_i = \int_{\Omega_i}\hat{s}\cdot\hat{n}_f\ d\Omega. \tag{3.40}$$

Finally completing the advective term:

$$\sum_f \Delta A_f\, I_{\eta,f,i}\int_{\Omega_i}\hat{s}\cdot\hat{n}_f\ d\Omega \approx \sum_f I_{\eta,f,i}\,(\hat{n}_f\cdot\vec{S}_i)\,\Delta A_f. \tag{3.41}$$

Then, the remaining terms must be integrated over the solid angle. In this case, it is also assumed that their value on the centroid is equal to the integral average over said solid angle:

$$\int_{\Omega_i} f(\hat{s})\ d\Omega \approx f(\hat{s}_i)\Delta\Omega_i = f_i\Delta\Omega_i. \tag{3.42}$$

The RTE can now be written as:

$$\sum_f I_{\eta,f,i}\,(\hat{n}_f\cdot\vec{S}_i)\,\Delta A_f + \beta_{\eta,P}\ I_{\eta,P,i}\ \Delta\Omega_i\Delta V_P = \kappa_{\eta,P}\ I_{\eta,P,i}\ \Delta\Omega_i\Delta V_P + \frac{\sigma_{s,\eta,P}}{4\pi}\Delta V_P \sum_j I_{\eta,P,j}\ \bar{\Phi}_{j,i}. \tag{3.43}$$

The boundary condition is given by applying energy conservation on the walls. We can start by integrating Equation 3.6 on the unit sphere to figure out the energy flux on the surface:

$$\int_{\hat{n}_w\cdot\hat{s}>0} I_{\eta,w}\ (\hat{s}\cdot\hat{n}_w)\ d\Omega = \int_{\hat{n}_w\cdot\hat{s}>0} (\epsilon_{\eta,w}I_{b,w})(\hat{s}\cdot\hat{n}_w)\ d\Omega + \rho_{\eta,w}\int_{\hat{n}_w\cdot\hat{s}<0} I_{\eta,w}\ |\hat{s}\cdot\hat{n}_w|\ d\Omega. \tag{3.44}$$

This expression above can then be developed to isolate $I_{\eta,w}$. First, we assume that $I_{\eta,w}$ is uniform over the hemisphere $\hat{s}\in\Omega : \hat{s}\cdot\hat{n} > 0$, which is reasonable for a diffusively reflecting and emitting wall, and allows us to take $I_{\eta,w}$ off the left hand side integral. By the same assumption, $I_{\eta,b,w}$ is also uniform and can be taken off the integral. Furthermore, $\epsilon_{\eta,w}$, $\rho_{\eta,w}$ and $\hat{n}_w$ are piece-wise constant for each discrete surface of the finite volume mesh, which also allows us to take them off the integral as well. Finally, we can write:

$$I_{\eta,w,out}\ \left(\hat{n}_w\cdot\int_{\hat{n}_w\cdot\hat{s}>0}\hat{s}\ d\Omega\right) = \epsilon_{\eta,w}\ I_{b,w}\ \left(\hat{n}_w\cdot\int_{\hat{n}_w\cdot\hat{s}>0}\hat{s}\ d\Omega\right) - \rho_{\eta,w}\ \left(\hat{n}_w\cdot\int_{\hat{n}_w\cdot\hat{s}<0} I_{\eta,w}\ \hat{s}\ d\Omega\right), \tag{3.45}$$

$$I_{\eta,w,out} = \frac{\epsilon_{\eta,w}\ I_{b,w}\ \left(\hat{n}_w\cdot\int_{\hat{n}_w\cdot\hat{s}>0}\hat{s}\ d\Omega\right) - \rho_{\eta,w}\ \hat{n}_w\cdot\left(\int_{\hat{n}_w\cdot\hat{s}<0} I_{\eta,w}\ \hat{s}\ d\Omega\right)}{\hat{n}_w\cdot\int_{\hat{n}_w\cdot\hat{s}>0}\hat{s}\ d\Omega}. \tag{3.46}$$

The integral in the Planck's law term simplifies with the denominator:

$$I_{\eta,w,out} = \epsilon_{\eta,w}\ I_{b,w} - \rho_{\eta,w}\frac{\hat{n}_w\cdot\int_{\hat{n}_w\cdot\hat{s}<0} I_{\eta,w}\ \hat{s}\ d\Omega}{\hat{n}_w\cdot\int_{\hat{n}_w\cdot\hat{s}>0}\hat{s}\ d\Omega}. \tag{3.47}$$

The statement above defines the boundary condition exactly. We can determine it numerically:

$$I_{\eta,i,w} = \epsilon_{\eta,w}I_{b,w} + \rho_{\eta,w}\frac{\sum_{\hat{n}_w\cdot\hat{s}_j<0} I_{\eta,j,w}\ |\vec{S}_j\cdot\hat{n}_w|}{\sum_{\hat{n}_w\cdot\hat{s}_k>0}\vec{S}_k\cdot\hat{n}_w},\ \hat{n}_w\cdot\hat{s}_i > 0\ \text{(Outgoing rays)}, \tag{3.48}$$

with:

$$\vec{S}_i = \int_{\Omega_i}\hat{s}\ d\Omega. \tag{3.49}$$

Likewise, the incident radiation, the divergent radiative heat flux and the radiative wall heat flux are given by:

$$G_{\eta,P} = \sum_i I_{\eta,P,i}\ \Delta\Omega_i \qquad \text{(Incident radiation)}, \tag{3.50}$$

$$\nabla \cdot q_{rad,\eta,P} = \kappa_{\eta,P}\, I_{\eta,b,P} - G_{\eta,P} \qquad \text{(Divergent radiative heat flux)}, \tag{3.51}$$

$$q_{rad,\eta,w} = \hat{n}_w \cdot \sum_i I_{i,\eta,w}\, \vec{S}_i \qquad \text{(Radiative wall heat flux)}. \tag{3.52}$$

Equation 3.43 is generic and can be applied to any Finite Volume and Finite Angle-based algorithm, even if they present unstructured meshes for both spatial and directional domains. Further simplifications can be assumed; for example, in a regular angular grid (Figure 23), the solid angles are defined by evenly splitting the unit sphere in the θ and ϕ directions, yielding linear integration limits. That is:

$$\int_{\Omega_i} f(\hat{s})\ d\Omega = \int_{\phi_1}^{\phi_2} \int_{\theta_1}^{\theta_2} f(\theta,\phi)\ \sin(\theta)\ d\theta\ d\phi. \tag{3.53}$$

It is not unusual for FAM implementations to use regular angular grids. This is the case for RTS, to give an example. It is also the case for Fluent (Murthy; Mathur, 1998) and OpenFOAM (Boyao, 2020). These grids make the integrals over solid angles easier to calculate.

Overall, the Finite Angles Method is another popular choice for radiative heat transfer problems. Like in the DOM, accurate solutions of complex problems can be obtained at a reasonable computational cost. Furthermore, the FAM is conservative, thanks to the fact that it integrates the entire RTE in the solid angle space. It also allows for more generic discretization of the angular domain, limited only by the mesh and the algorithm.

3.5 General formulation for the DOM and FAM in regular FVM grids

For the sake of completely finalizing the RTE discretization with the FVM and either the DOM or the FAM, Equations 3.25 and 3.43 can be developed in a structured hexahedral grid illustrated in Figure 24, leading to the following general expression:

$$A_P I_{\eta,P,i} + A_e I_{\eta,e,i} + A_w I_{\eta,w,i} + A_n I_{\eta,n,i} + A_s I_{\eta,s,i} + A_t I_{\eta,t,i} + A_b I_{\eta,b,i} = S_M, \tag{3.54}$$

where the sub-indices e, w, n, s, t and b refer respectively to the east, west, north, south, top and bottom cells relative to the reference cell P. This formulation adapts well to an iterative solution process for the angular space coupling: first, the split RTE is solved

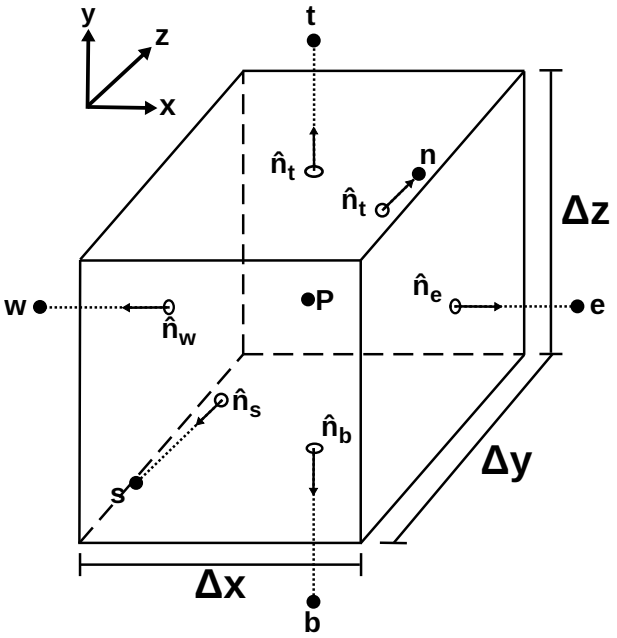

Figure 24 – Computational cell on which the stencil in Equation 3.54 is defined.

independently for all the i discrete directions. Afterwards, the term S_M, which is treated as a source term, is updated, and the discretized RTE is solved again.

The values of the A_k coefficients depends on whether the DOM or the FAM was applied. We can define the unit cosines ξ_i, η_i and μ_i from $\hat{s}_i$:

$$\hat{s}_i = \xi_i \, \hat{i} + \eta_i \, \hat{j} + \mu_i \, \hat{k}. \tag{3.55}$$

And then define the A_k coefficients for the FVM + DOM discretization in the following manner:

$$A_e = \frac{(2\alpha - 1)|\xi_i| - \xi_i}{2} \, \Delta y_P \, \Delta z_P, \tag{3.56}$$

$$A_w = \frac{(2\alpha - 1)|\xi_i| + \xi_i}{2} \, \Delta y_P \, \Delta z_P, \tag{3.57}$$

$$A_n = \frac{(2\alpha - 1)|\eta_i| - \eta_i}{2} \, \Delta x_P \, \Delta z_P, \tag{3.58}$$

$$A_s = \frac{(2\alpha - 1)|\eta_i| + \eta_i}{2} \, \Delta x_P \, \Delta z_P, \tag{3.59}$$

$$A_t = \frac{(2\alpha - 1)|\mu_i| - \mu_i}{2} \, \Delta x_P \, \Delta y_P, \tag{3.60}$$

$$A_b = \frac{(2\alpha - 1)|\mu_i| + \mu_i}{2} \, \Delta x_P \, \Delta y_P, \tag{3.61}$$

$$A_P = \beta \Delta x_P \, \Delta y_P \, \Delta z_P - A_e - A_w - A_n - A_s - A_t - A_b. \tag{3.62}$$

And for the FVM + FAM model, we have:

$$A_e = \frac{(2\alpha - 1)|\hat{n}_e \cdot \vec{S}_i| - (\hat{n}_e \cdot \vec{S}_i)}{2} \Delta y_P \ \Delta z_P, \tag{3.63}$$

$$A_w = \frac{(2\alpha - 1)|\hat{n}_w \cdot \vec{S}_i| + (\hat{n}_w \cdot \vec{S}_i)}{2} \Delta y_P \ \Delta z_P, \tag{3.64}$$

$$A_n = \frac{(2\alpha - 1)|\hat{n}_n \cdot \vec{S}_i| - (\hat{n}_n \cdot \vec{S}_i)}{2} \Delta x_P \ \Delta z_P, \tag{3.65}$$

$$A_s = \frac{(2\alpha - 1)|\hat{n}_s \cdot \vec{S}_i| + (\hat{n}_s \cdot \vec{S}_i)}{2} \Delta x_P \ \Delta z_P, \tag{3.66}$$

$$A_t = \frac{(2\alpha - 1)|\hat{n}_t \cdot \vec{S}_i| - (\hat{n}_t \cdot \vec{S}_i)}{2} \Delta x_P \ \Delta y_P, \tag{3.67}$$

$$A_b = \frac{(2\alpha - 1)|\hat{n}_b \cdot \vec{S}_i| + (\hat{n}_b \cdot \vec{S}_i)}{2} \Delta x_P \ \Delta y_P, \tag{3.68}$$

$$A_P = \beta_P \Delta x_P \ \Delta y_P \ \Delta z_P \ \Delta \Omega_i - A_e - A_w - A_n - A_s - A_t - A_b, \tag{3.69}$$

where $\hat{n}_e = \hat{i}$, $\hat{n}_w = -\hat{i}$, $\hat{n}_n = \hat{j}$, $\hat{n}_s = -\hat{j}$, $\hat{n}_t = \hat{k}$, $\hat{n}_b = -\hat{k}$ are the face normals and Δx_P, Δy_P and Δz_P are the dimensions of cell P. Equation 3.54 lends itself to a matrix-free iterative solver, where values of $I_{\eta,P,i}$ are calculated directly from the expression. It can also be used to assemble a linear system where A_P is part of the diagonal, A_k are the off-diagonal terms and S_M can be placed at the independent vector. With this, the RTE is finally fully discretized and implementing it in an algorithm that uses structured Cartesian grids should be quite straightforward.

3.6 Numerical issues in the RTE

3.6.1 Overhang

Overhang is a class of numerical errors that arise in discrete RTE problems, where the solid angles of the unit sphere present in a cell's face are not perfectly aligned with the face's normal, as can be seen in Figure 25. As such, there are angular directions that are fully incoming (coloured green), fully outgoing (coloured red) and both incoming and outgoing (coloured yellow). The problem arises in correctly representing the contributions of the yellow solid angles, which might otherwise result in unphysical energy balance and inaccuracies. In regular Cartesian meshes, overhang does not occur as the cell faces neatly divide the unit sphere into outgoing and incoming quadrants, but this problem can be expected to occur in unstructured meshes and possibly in other forms of representing complex geometries like Immersed Boundary Methods (IBM).

One of the solutions for dealing with this problem is to simply use a more refined angular mesh. This way, the higher resolution will more accurately represent the energy balance and diminish the influence of overhang; they will still exist, but will have less influence on the problem. Of course, finer angular meshes makes the global problem

heavier and may not be ideal. Another solution is **pixellation**, as described by Murthy and Mathur (1998), which consists of dividing the overhang angles into smaller solid angles, allowing then for greater resolution only in the problematic area, which is similar to adaptive mesh refinement. Depending on the problem, a fine level of pixellation may not be needed. In fact, some problems may be acceptably accurate even without any pixellation at all. For more information on overhang and pixellation, it is suggested to refer to this publication.

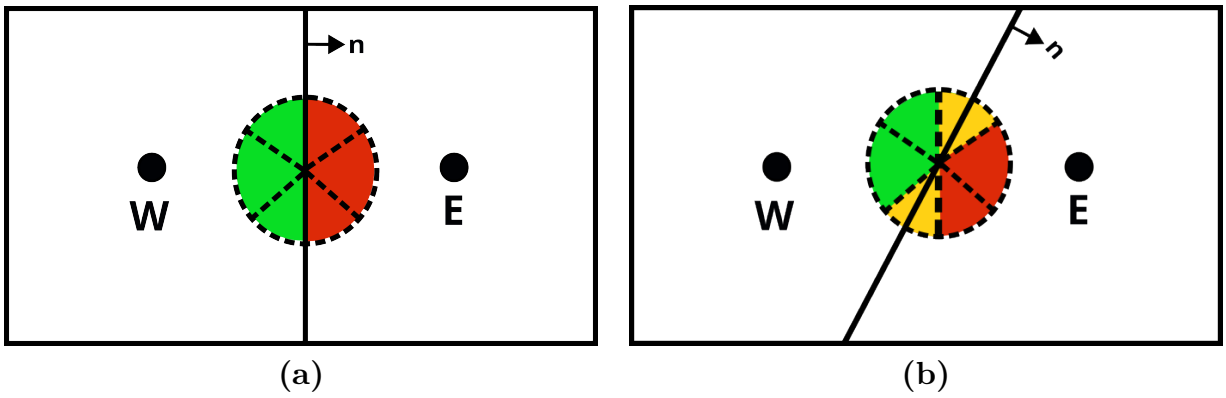

Figure 25 – Illustration of the overhang effect in the face of a 2D domain. In (a), no overhang occurs, as the solid angles are all either incoming (green) or outgoing (red) from the face. In (b), the yellow coloured angular volumes have both incoming (positive) and outgoing (negative) contributions, which causes issues in the calculation of the total flux that crosses the face. Overhang error appears when their contribution is incorrectly calculated, such as considering the entire volume as either incoming or outgoing. Figure adapted from Murthy and Mathur (1998).

3.6.2 Ray effects and false scattering

Ray effects are a result of coarse angle discretization and become evident in problems with strong directional bias, such as the one illustrated in Figure 26. It can be noticed that the radiation creates distinct, sharp rays on the solution that are non-physical. False scattering, on the other hand, is caused by the grid lines not being aligned with the angular directions. As such, radiation beams gradually widen as they move through the domain. One reason this problem may appear is a coarse discretization of the spatial domain or low order discretization methods.

According to Modest and Mazumder (2022), ray effects and false dispersion may nullify each other. That is, a coarse spatial discretization may offset numerical errors that arise from coarse angular discretization, and vice-versa. As a result, refining the spatial mesh may cause ray effects to become more pronounced, and refining the angular mesh may cause false dispersion to get more pronounced, both of which reduce the accuracy of the solution. To obtain a true accuracy increase, one should take care to refine one mesh

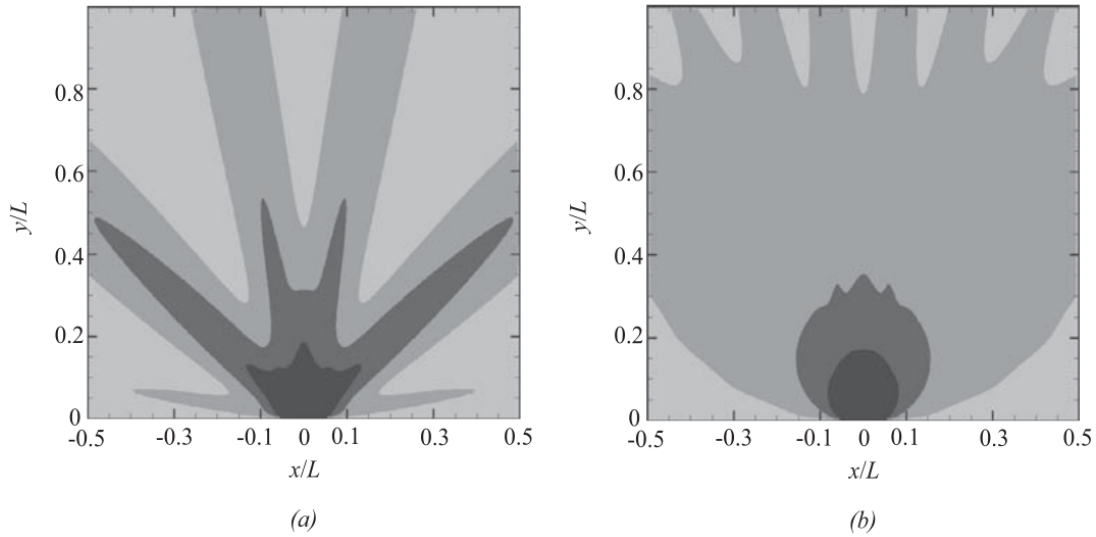

Figure 26 – Illustration of ray effects, adapted from Modest and Mazumder (2022). Figure (a) is the temperature field of a case solved in DOM S_8, while (b) shows the same problem solved with FAM using the same directions as the S_8 quadrature. The strong gradients resulting in well defined rays in the temperature field are characteristic of ray effects.

without leaving the other too coarse, which has a side-effect of making the problem even more costly, as refining one grid too much forces the other to be refined as well.

3.7 Disambiguation on the Discrete Ordinates and the Finite Angles Methods Terminology

An issue regarding the Discrete Ordinates Method and the Finite Angles Method is simply their nomenclature. In the literature, it is common practice to classify all forms of discretization of the angular domain (i.e. the unit sphere) as DOM, whether they are based on quadratures or on the Finite Volumes Method. The Finite Angles nomenclature was proposed by Modest and Mazumder (2022) in their book to differentiate it from the "Finite Volumes Method" terminology, which has a broader scope of meanings, and to better emphasize its unique aspect of dividing the unit sphere into a finite set of solid angles, which contrasts with quadrature-based discretization.

In order to improve clarity, this work also adopts the "Finite Angles Method" nomenclature suggested by Modest and Mazumder (2022). That is, it refers to discretization methods that integrate the RTE over a solid angle as described in Section 3.4. Furthermore, the "Discrete Ordinates Method" nomenclature is used to address, specifically, the methods that discretize the unit sphere into finite points, but that do not perform any sort of solid angle integral, instead utilizing weights. In this specific method, the angular domain is simply discretized by finite differencing, with the integrals over it

being approximated by numerical quadrature, as per Section 3.3. In the Finite Angles Method, the RTE is split into many PDEs, with each PDE being integrated over its respective solid angle, which ensures better conservativeness. Likewise, the integrals over the directional domain are not approximated by a quadrature.

This distinction is important to comprehend, as it is usual for the "DOM" nomenclature to be used to refer to what is defined here as the Finite Angles Method. This is the case for both AnSYS Fluent and OpenFOAM. Unfortunately, it can be difficult to make sure which methodology is actually being used, as the literature may not make it clear at first glance. A good guiding principle is to check on whether an author or documentation mentions the discretization in number of divisions per angular coordinate; if so, then most likely they are using an implementation of FAM. Similarly, mentions of quadrature commonly imply that DOM is being used.

Both FAM and DOM are quite similar in result quality and computational cost, and are generally applicable to the same cases. In fact, they are a staple of deterministic RTE solvers, as both methods allow a simulation to be easily refined to arbitrary precision and provide accurate enough results with reasonable computational costs. However, FAM may be better in a few cases, such as in the case of highly anisotropic media, as noted by Coelho (2014). Figure 26 also shows a situation where the FAM presented better results, alleviating ray effect errors.

3.8 Spectral Modelling

So far, the spatial and angular spaces discretization of the RTE were discussed. We have yet to discuss how to discretize and model the spectral dimension, represented by the wavenumber η. The radiative properties of the media κ_η and $\sigma_{s,\eta}$, as well as the Planck Law term $I_{b,\eta}$ are dependent on the wavenumber; consequently, the radiative intensity I_η is a function of it. In rigour, these properties vary continuously on the electromagnetic spectrum and thus also require a discretization of sorts. There are many ways to model the spectral dimension, each with its associated costs and accuracy, which shall be summarized below.

The simplest spectral model is the **gray gas model**, which simply assumes that there is no spectral dependency on the RTE: κ_η and $\sigma_{s,\eta}$ are constant in the electromagnetic spectrum ($\kappa_\eta = \kappa$, $\sigma_{s,\eta} = \sigma_s$) and $I_{b,\eta}$ may simply be calculated by the Stefan-Boltzmann Law (Subsection 2.4.4), thus $I_{b,\eta} = I_b$. Effectively, only one band of the RTE must be solved, making it computationally very cheap and simple to implement. This model can be quite good at simple numeric simulations and may even be applied successfully to the modelling of real world problems, but it is unfortunately quite limited. That is because the radiative transfer usually varies significantly in the electromagnetic spectrum and it simply doesn't suffice to use average values of spectrally dependent properties, as

exemplified in Figures 5, 6 and 7. Therefore, the spectral variation of the RTE must be modelled and solved to obtain accurate solutions for many, if not most, real world problems, including those involving combustion processes.

If a gray gas model does not suffice, a possible approach is the Line-By-Line (LBL) calculation. It consists of breaking the electromagnetic spectrum into a series of narrow bands, which may amount to around a million (Modest; Mazumder, 2022). For each band, the RTE is solved locally with fixed properties, yielding a radiative intensity field I_{η_i} associated with that band. This process is repeated in all the other bands, with the net radiative intensity field I and correlated fields being determined by a discrete integral over all the bands. The spectrally dependent properties may be taken from high resolution spectroscopic databases such as the ones given by Gordon *et al.* (2017) and Rothman *et al.* (2010).

The LBL method is the most accurate way to spectrally model the RTE, but it is also very expensive. It can be understood as analogous to Direct Numerical Simulations (DNS) in CFD, where the flow, with all of its turbulent structures, is entirely solved: both are high resolution, high fidelity and high accuracy solutions, but are computationally very expensive and of limited application beyond academic research and benchmarking. In order to solve complex industrial processes, a model that can accurately represent the spectral dimension of the RTE while being much cheaper than LBL (i.e. solving only a few bands) is required. That being said, according to Modest and Mazumder (2022), the LBL method may be efficient when used with Monte Carlo methods for solving the RTE, as seen in publications such as Feldick and Modest (2012). However, even if it may be efficient, it is still expensive when compared to other models.

A cheap alternative for spectral modelling is the Weighted Sum of Gray Gases (WSGG), first introduced by Hottel and Sarofim (1967). As the name suggests, it consists of solving a series of bands for the RTE, each associated to a virtual gray gas with given I_b, κ and σ_s that are determined from the model. The combined solution for the radiative intensity I field of each gray gas, then, should yield an accurate solution for the real, spectrally dependent gas being modelled. WSGG models usually require the order of 5 bands (four gray and one transparent) to be solved, making them quite economical and commonly employed in combustion systems simulations, as exemplified in Orbegoso (2013). They may also support single band models, which may be aptly called gray. RTS uses the WSGG implementation found in Bordbar, Fraga and Hostikka (2020), which extends the model described by Bordbar, Węcel and Hyppänen (2014) to allow for all molar fraction ratios of H_2O and CO_2 instead of being limited to $0.01 \leq \frac{Y_{H_2O}}{Y_{CO_2}} \leq 4.0$ and can be applied to domains with non-uniform pressure, temperature and species fractions.

Other WSGG models found in the literature include Bordbar *et al.* (2021), which extends Bordbar, Węcel and Hyppänen (2014), modelling a broader pressure range.

Sadeghi *et al.* (2021) presents a WSGG model for six different hydrocarbon fuel vapours, CO and soot, which were then coupled with other WSGG models for carbon dioxide and water vapour by means of a superposition method. This allows for the modelling of complex combustion environments that can account for the participation of fuel and soot. Fonseca *et al.* (2023) provides a wide-band based WSGG for mixtures of water vapour and CO_2, with or without soot. This wide-band approach consists of dividing the electromagnetic spectrum into five bands and applying the WSGG method to each of them, which allows for higher accuracy when compared to similar models found in the literature.

Another popular method is the Full Spectrum k-Distribution (FSK), which traces back to Modest and Zhang (2001). It consists of remapping the absorption coefficient given by spectral data (the same ones used in LBL) of the gases into a monotonic variable k defined by a cumulative k-distribution, which is easier to integrate. In the end, it allows the RTE to be solved in a small number of bands (similar to WSGG), with the radiative intensity being integrated by a Gaussian quadrature. The Full Spectrum Correlated-k uses a correlated absorption coefficient to allow for modelling of non-homogeneous media with variation of pressure, temperature and species concentrations, further broadening the cases in which the FSK is applicable. According to Wang *et al.* (2016), the FSK method may reduce the spectral dimension from millions of spectral lines in the LBL method to as little as around ten bands without losing spectral line information.

Other models discussed in the literature include the Statistical Narrow Band Model (SNBM), also said to be highly accurate and famously used in RADCAL (Grosshandler, 1993), but, according to Bordbar, Węcel and Hyppänen (2014), requires hundreds to thousands of band evaluations. Another method is the Spectral Line Based Weighted Sum of Gray Gases (SLW), introduced by Denison and Webb (1993) and worked on by Solovjov and Webb (2000), which may be thought of as similar to the aforementioned WSGG and FSK.

Assembling any of these spectral models requires careful processing of spectral databases that weigh at least several thousand gigabytes, something that is not trivially performed, especially for complex gas mixtures. As for their accuracy, Rashidzadeh *et al.* (2023) uses a one-dimensional domain filled with H_2O as a participating medium to compare the accuracy of WSGG, SLW and FSK, concluding that FSK generally performs better than the WSGG, with SLW being close in accuracy to the FSK when four or more bands are used. It should be noted that two of the authors from this publication also worked on the WSGG model shown in Bordbar, Węcel and Hyppänen (2014) and Bordbar, Fraga and Hostikka (2020). In the comparison made by Consalvi *et al.* (2020) using turbulent axisymmetric jet diffusion flames fueled by either hydrogen or methane, it was also shown that FSK and SLW are the best choices for CFD codes, displaying similar accuracy, although FSK shows considerably higher error. The authors also note

that the WSGG has satisfactory accuracy for engineering combustion simulations. Owen *et al.* (2024) cites the development of an FSK method as a future endeavour in the development of the Pele software suite, indicating that it is a trend in spectral modelling, even in the case of highly complex CFD. In contrast, Centeno *et al.* (2018) found excellent agreement between a WSGG model and LBL results for a case that is representative of a laminar diffusion jet flame of ethylene diluted with H_2O. Andre *et al.* (2019) also deemed results for the WSGG model tested as acceptable, while also being the fastest in their analysis. Fonseca *et al.* (2023) also achieved appreciable accuracy in their WSGG model for H_2O, CO_2 and soot mixtures. As such, it seems that accuracy may vary significantly according to the model, which may perform better or worse depending on the application it is being used on and the manner in which it was developed.

3.9 Radiation Turbulence Interaction (TRI)

Radiation Turbulence Interaction refers to the complex, non-linear, two-way coupling between radiative heat transfer and turbulence present in fluid dynamics, as illustrated in the chart from Figure 27. In summary, the media's radiative properties κ and σ_s, as well as the emission term $I_{b,\eta}$, are dependent on the temperature, pressure and species concentration fields. These fields are determined by the media's flow and are thus subject to the effects of turbulence. On the other hand, the radiative heat transfer also affects the energy balance equation, which in turn has a non-linear effect on the other flow properties (velocities, pressure and species concentrations, for example). This coupling leads to a series of effects that are still not well understood.

The turbulence in fluid dynamics may be modelled by the unfiltered CFD balance equations, as long as the spatial mesh and time steps are of high enough resolution, which characterizes Direct Numerical Simulation (DNS). Computational costs usually prohibit the use of this method, which leads people to resort to applying a filter to the balance equations, resulting in a new system of PDEs for the average properties of the flow that require less resolution to be solved. This new system contains new terms related to the fluctuation of the averaged fields that must be modelled, leading to what is known as the turbulence closure problem. In order to solve this problem, a plethora of turbulence models exist (Silveira Neto, 2026).

To give an illustrative example, a generic filter shall be applied in Equation 3.5:

$$\overline{\nabla \cdot (I_\eta \ \hat{s})} + \overline{\beta_\eta I_\eta} = \overline{\kappa_\eta I_{b,\eta}} + \overline{\frac{\sigma_{s,\eta}}{4\pi} \int_{4\pi} I_\eta(\vec{x}, \hat{s}') \ \Phi(\hat{s}, \hat{s}') \ d\Omega'}. \tag{3.70}$$

The filtered scattering, absorption and extinction terms may be opened as follows:

$$\overline{\beta_\eta I_\eta} = \overline{\beta_\eta}\ \overline{I_\eta} + \overline{\beta'_\eta I'_\eta}, \tag{3.71}$$

$$\overline{\kappa_\eta I_{b,\eta}} = \overline{\kappa_\eta}\ \overline{I_{b,\eta}} + \overline{\kappa'_\eta I'_{b,\eta}}, \tag{3.72}$$

$$\overline{\frac{\sigma_{s,\eta}}{4\pi}\int_{4\pi} I_\eta(\hat{s}')\ \Phi(\hat{s},\hat{s}')\ d\Omega'} = \frac{\overline{\sigma_{s,\eta}}}{4\pi}\int_{4\pi}\overline{I_\eta(\hat{s}')}\ \Phi(\hat{s},\hat{s}')\ d\Omega' + \frac{1}{4\pi}\int_{4\pi}\overline{\sigma'_{s,\eta}I'_\eta(\hat{s})'}\ \Phi(\hat{s},\hat{s}')\ d\Omega'. \tag{3.73}$$

Rigorously, the RTE should receive the same filter operation as its CFD counterparts, as shown above, which will also result in a filtered equation and new unknown terms that must be defined somehow; otherwise, the model might not accurately resemble reality. This is one of the biggest concerns of studies in the field of TRI. Although such models exist, they aren't yet as mature as the ones used in CFD.

Coelho (2007), a 73 pages article, is one of the reference publications in the subject of TRI and contains an in-depth discussion complete with turbulence model implementations for the RTE, including implementations utilizing the Discrete Ordinates, Finite Angles, Spherical Harmonics and Monte Carlo methods. The author has also studied TRI behaviour in Large Eddy Simulations (LES), accounted in Roger, Coelho and da Silva (2010), and in Sandia D Flames, registered in Miranda *et al.* (2019). Modest and Haworth (2016) is a book that provides an in-depth discussion on the subject of radiation in turbulent combustion processes, including its modelling and analysis on canonical problems.

Coelho and Fraga (2024) is a recently published and extensive review article on TRI in LES simulations, which notes that the importance of TRI in LES simulations has only started to be investigated in the last decade. The authors note that much is still unknown in this area, and that in many cases sub-grid fluctuations contribute significantly for TRI, citing large pool fires and the Sandia D flame simulated by Gupta, Haworth and Modest (2013) as particular examples. Usually, in these cases, the radiative emission is particularly affected by TRI. In other cases, however, sub-grid scale TRI is generally unimportant. This paper also notes that industrial-scale flames, high pressure combustion, fuel evaporation and solid fuel are cases which still lack studies on sub-grid scale TRI. The authors of this publication have also done a study on how TRI behaves in different points of the electromagnetic spectrum in Fraga, Coelho and Zhao (2024), citing that it can have important implications on experimental data collected with, for example, spectral tomography. They conclude that its effect does in fact differ in intensity depending on the spectral position.

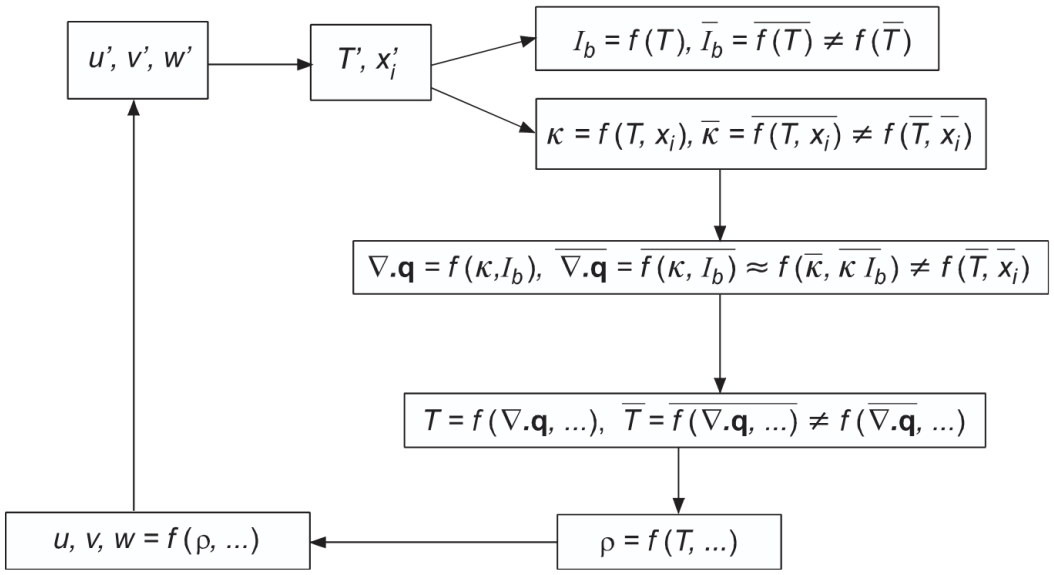

Figure 27 – Diagram illustrating the interaction with turbulent flow properties and radiative transfer properties and the new terms that arise from applying a filter to the RTE. Taken from Coelho (2007).

3.10 Methods for Solving the RTE

The discrete RTE may be understood as a linear system which must be solved to obtain the radiative intensity field. This may be represented mathematically by the expression $\vec{\vec{A}}\vec{I} = \vec{b}$. Given that each band of the problem is assumed independent from each other, this analysis will focus on a linear system defined for a single band. Solving a non-gray RTE may then be understood as solving a similar linear system for every band present in the problem, which will provide a five-dimensional radiative intensity field when solved. There are two main methods to solve this linear system: a Gauss-Seidel based Directional Sweep Algorithm (DSAL) or a Krylov Space (KSP) based algorithm.

The directional sweep algorithm may be summarized as iterating through each cell in the spatial domain for each direction in the angular domain, calculating the radiative intensity value of each node. This sweep is performed **in sequence**, where the the radiative intensity of a cell is determined based on the recently calculated value of its neighbouring cells, such that the sweep naturally follows the radiation wave front. In these methods, it is usual for the angular coupling of the RTE to be solved iteratively: the in-scattering integral effects is contained in a source term S_M, as described previously, and the sweep is performed with its value kept constant. After finishing the sweep, S_M is updated with the new values and a new sweep follows. The diffuse reflection on the boundaries is also dealt with in a similar manner. This process repeats until convergence, and may take more or less time depending on factors such as scattering effects present in the domain or non-black boundaries. The strong directional dependence of this method (one node can't be calculated before another node's value has been determined) makes

it hard to parallelize, as the sequenced sweep limits its parallelization. a discussion on this problem is present in Moustafa (2015), who managed to implement a large scale parallelization of this algorithm. The DSAL is the algorithm that RTS uses for solving the RTE, and discussions on this method are also present in Rodrigues (2023) and Modest and Mazumder (2022). It is commonly chosen due to its simplicity and efficient memory usage. It is also physically inspired in the manner which radiation propagates in the domain. More details on RTS's implementation of the DSAL may be seen in Subsection 4.5.2.

Krylov space based algorithms utilize Krylov solvers, usually GMRES, for determining the RTE solution. These methods require defining two main operations: a matrix multiplication of the form $\overrightarrow{\overrightarrow{A}}\vec{x}$, where $\vec{x}$ is any vector, such as an initial guess or approximated solution; and a good pre-conditioner. For the former, there are two main approaches: one may simply assemble the entire matrix $\overrightarrow{\overrightarrow{A}}$, which is easier and allows the use of default pre-conditioners; or may instead opt for a matrix free approach, in which $\overrightarrow{\overrightarrow{A}}$ is not assembled and instead $\overrightarrow{\overrightarrow{A}}\vec{x}$ is calculated with a clever, custom algorithm. While a matrix-free approach may limit the options of default pre-conditioners available, it is much more memory efficient and avoids time costs related to matrix assembly. Memory constraints may make assembling $\overrightarrow{\overrightarrow{A}}$ unfeasible, as observed by Jolivet, Badri and Favennec (2021). Although less common, Krylov solvers have been applied successfully by Charest, Groth and Gülder (2012) and Badri *et al.* (2018), the latter of which followed their work on a matrix-free approach in Jolivet, Badri and Favennec (2021). This methodology was shown to be promising in high scale, distributed computer simulations and does not contain the same sequential dependence of the DSAL. As such, they may be better candidates for parallelization and GPU implementations. Newton-Krylov methods may also be used to accelerate the convergence even further, as shown by Charest, Groth and Gülder (2012), and other Krylov methods like BICGStab may show satisfactory performance, as noted by Badri *et al.* (2019).

Finally, it is interesting to have a discussion on pre-conditioners. A good pre-conditioner is important for accelerating convergence, especially on complex and coupled linear systems such as the ones provided by the RTE. This is particularly desirable in problems with strong scattering, which strengthens the coupling in the angular domain and makes convergence slower. While standard pre-conditioners, like block Jacobi or Schwarz, are applicable, they may not be feasible unless the matrix $\overrightarrow{\overrightarrow{A}}$ is assembled. The Diffusion Synthetic Algorithm (DSA), first introduced by Alcouffe (1977), consists of solving a simplified version of the RTE known as the diffusion approximation, which is much easier to deal with than the full RTE. Badri *et al.* (2018) also makes use of a pre-conditioner that is resembles this method. Both approaches result in an equation that is not the complete RTE, but is similar enough to it while being much simpler to solve, which are all characteristics of good pre-conditioners.

3.11 Coupling with CFD

Radiation processes interfere with the balance of physical quantities that CFD models rely upon. While the radiation in the domain may also technically affect the mass and linear momentum equations, its effects are negligible in non-relativistic scenarios: that is, this radiation won't convert into mass, or vice versa, nor is its linear momentum significant enough to have appreciable effects. Therefore, accounting for its effects only in the energy balance equation is enough (Viskanta, 1987).

The coupling of radiative heat transfer with fluid dynamics can be divided in two parts. The first is adding its effects as a source term in the energy equation (through the boxed term in Equation 3.76). To do this, a term called **divergent radiative heat flux** must be determined from the solved radiative intensity field, as per Equation 3.10, which results in a simple calculation to be performed in all cells of the domain. In the MFSim-RTS coupling, the divergent radiative heat flux is calculated in the RTS mesh, then interpolated to MFSim with the assumption that it is a scalar field.

$$\frac{\partial \rho}{\partial t} + \nabla \cdot (\rho \vec{u}) = 0, \tag{3.74}$$

$$\frac{\partial (\rho \vec{u})}{\partial t} + \nabla \cdot (\rho \vec{u} \otimes \vec{u}) = -\nabla p + \nabla \cdot \vec{\vec{\tau}} + \rho \vec{g}, \tag{3.75}$$

$$\rho c_p \left(\frac{\partial T}{\partial t} + \vec{u} \cdot \nabla T \right) = \nabla \cdot (k \nabla T) + \sum_{i=1}^{N_s} h_i \dot{\omega}_i - \sum_{i=1}^{N_s} \vec{J}_i \cdot \nabla h_i + \Phi - \boxed{\nabla \cdot \vec{q}_{rad}}, \tag{3.76}$$

$$\frac{\partial (\rho Y_i)}{\partial t} + \nabla \cdot (\rho Y_i \vec{u}) = -\nabla \cdot (\rho D_i \nabla Y_i) + \dot{\omega}_i. \tag{3.77}$$

The second step is determining the radiative heat flux through the boundaries of the domain. This is not only important for quantifying heat transfer in the system (as radiation may make up a significant portion of the heat that enters or leaves the domain), but also for establishing boundary conditions relating to energy fluxes, which are of the Neumann type. For example, in an adiabatic boundary, the net heat flux through it is established as zero:

$$\vec{q} \cdot \hat{n}_w = 0. \tag{3.78}$$

In CFD problems with radiative heat transfer, the heat transmitted through a boundary is the sum of the convective heat flux (caused by a combined effect of advection and conduction from the fluid near the wall) and the radiative heat flux:

$$\vec{q} \cdot \hat{n}_w = (\vec{q}_{conv} + \vec{q}_{rad}) \cdot \hat{n}_w, \tag{3.79}$$

or, put more simply, as:

$$q = q_{conv} + q_{rad}. \tag{3.80}$$

The value of q_{rad} may be retrieved from the RTE solution. q_{conv}, on the other hand, is dependent on the energy boundary condition of the surface. A prescribed temperature falls under the Dirichlet boundary condition, and thus the heat flux is simply calculated from the CFD solution. Prescribing the heat flux through the boundary itself constitutes a Neumann boundary condition for the temperature. In this case, the convective heat flux is stated as:

$$q_{conv} = -k\nabla T \cdot \hat{n}_w. \tag{3.81}$$

An adiabatic boundary is defined as having a net zero heat flux passing through it:

$$q = 0 \text{ (Adiabatic boundary)}. \tag{3.82}$$

For a problem without radiative heat transfer, this simply means that the convective heat flux is zero and thus:

$$q = q_{conv} = 0 \rightarrow -k\nabla T \cdot \hat{n}_w = 0 \overset{k\neq 0}{\rightarrow} -\nabla T \cdot \hat{n}_w = 0. \tag{3.83}$$

However, for an adiabatic boundary with radiative heat transfer, it follows that:

$$q = q_{conv} + q_{rad} = 0, \tag{3.84}$$

$$q_{conv} = -q_{rad}, \tag{3.85}$$

$$k\nabla T \cdot \hat{n}_w = q_{rad}. \tag{3.86}$$

From which ∇T can be calculated from the known value of q_{rad}. More generically, it can be established that:

$$\nabla T \cdot \hat{n}_w = \frac{q_{rad,w}}{k}. \tag{3.87}$$

That is, **the temperature gradient for an adiabatic boundary is not necessarily equal to zero when radiative heat transfer is considered**. Instead, the temperature gradient must be defined from the radiative heat fluxes such that the net heat transfer through the boundary is zero. This fact must be taken into account for **any** Neumann or mixed type boundary conditions of the energy equation. In the MFSim-RTS coupling, $q_{rad,w}$ is calculated by RTS in its own mesh and interpolated to MFSim via a bilinear interpolation on the walls.

In summary, the coupling of the RTE with fluid dynamics is made by introducing the radiative heat fluxes of the domain on the formulation of the energy balance equation **and** its boundary conditions. Computationally, the coupling with a CFD algorithm can be summarized as follows:

1. With an input temperature, pressure and species fields, solve the RTE;

2. From the solution of the RTE, calculate $\nabla \cdot \vec{q}_{rad}$ and apply it as a source term for the energy equation;

3. From the solution of the RTE, calculate $q_{rad,w}$ and use it to define the Neumann or mixed-type boundary conditions of the energy equation where applicable;

4. Follow the CFD part of the iteration.

Further discussions on the computational implementation of the coupling between radiation and fluid dynamics can be seen in Sections 4.3, 4.5.3 and 5.1.

4 Bibliographic review

This chapter provides a discussion on topics of particular concern to this work, namely the effects of radiative heat transfer in combustion systems and thermal cavities, and the coupling of radiative heat transfer with CFD. It also features a review and description of MFSim and RTS, as well as the old coupling between the two, which is improved upon in this work.

4.1 Combustion problems with radiative heat transfer

A brief discussion on the importance of radiative heat transfer in combustion systems is in order to illustrate the importance of the coupling developed in this work. As such, we will summarize a non-exhaustive list of bibliographic works on the subject.

Lee *et al.* (2013) studies the effects of CO_2 dilution on NO_x emissions on a turbine using biogas as fuel. The study uses a numerical model and experimental verification in their endeavour. The authors concluded that CO_2 dilution decreases NO_x emission as its dilution rate increases, while also decreasing flame temperature. Radiation further drops this flame dtemperature. They also found that modelling radiative heat loss based only on a temperature mean tends to underestimate its value, while accounting for temperature fluctuations yields a more accurate estimation.

Bidi, Hosseini and Nobari (2008) show a turbulent premixed methane-air flame in a cylindrical chamber, simulated with DOM and WSGG and using a $k - \epsilon$ turbulence model. Despite not using any TRI models in the RTE, feeding it the average fields directly, they concluded that radiation does have an appreciable effect in the temperature and species fields.

Liu *et al.* (2002b) is a classic publication that studied radiation interaction with gases and soot, and its influence on predicting soot formation on a co-flow laminar ethylene diffusion flame. The authors compared an experimental setup with computer simulations using different radiation models. They illustrated quite clearly that radiation modelling has appreciable effects on soot formation and on the flame temperature. New publications on sooting combustion in computational models include Torres (2021), Tardelli (2021) and Rodrigues (2018).

Orbegoso (2013) performed a detailed study on the radiative heat transfer in turbulent combustion systems, comparing different spectral and soot models. The author combined a series of cases, done both numerically and experimentally, to evaluate their predictive capabilities and limitations. These cases range from a 1D non-isothermal radiation case to a spray burner simulation based on the experiments of Nakamura *et al.* (2011). He

used Fluent as the main simulation platform, having developed a User Defined Function to allow it to pull spectral information from RADCAL.

Armengol (2019) presents a base study on the effects of thermal radiation on free turbulent water vapour jets. It coupled a Monte Carlo radiation solver using a Correlated-k method for spectral modelling with DNS fluid simulation to produce highly detailed information on non-isothermal free jets. The author presents information of effects that radiative heat transfer has on the flow fields, including its second order moments, and a scaling law for the decay of the temperature profile in the jet centerline. He also contrasts DNS with RANS results for identifying key parameters that might require further modelling.

Owen *et al.* (2024) describes a multi-physics, adaptative mesh solver for combustion systems that includes a Spherical Harmonics P_1 solver with soot modelling and a gray gas model based on a Planck-mean absorption coefficient that can incorporate gases such as CO_2, H_2O, CO, C_2H_4 and CH_4. The authors mention that future works will include modelling of non-gray effects by means of an FSK model and higher-order RTE solvers.

Ge *et al.* (2023) is cited by the former publication as a reference to their spectral model, and features a comparison between the spherical harmonics P_N and FAM discretization methods on turbulent jet flames. The authors used a 1D homogeneous case and a scaled Sandia D flame in a series of configuration to test these discretization methods, using Photon Monte Carlo with LBL as a benchmark solution. It was found that FAM is more accurate than P_N for a scaled Sandia D flame, and that it in general performs better than P_N. Although the authors specifically studied turbulent flames, and even acknowledge the existence of TRI, they neglected TRI modelling of the RTE, citing that "the focus was on the performance of RTE solvers".

Zenou (2025) presents a theoretical analysis of the coupling between fluid dynamics, combustion reactions and radiation. This analysis consists of defining a series of dimensionless coupling numbers based on the characteristic time scales of convection, reaction and radiation. From their values, roughly three different regimes can be identified: one where radiation has minor effects, another where it interacts only with the fluid dynamics and a third one where radiation interacts with both fluid flow and chemical reactions.

4.2 Thermal cavity

The thermal cavity is a canonic fluid dynamics problem that illustrates **natural convection**. It typically consists of a rectangular enclosed domain containing a fluid in its interior that is immersed in a gravitational field. The temperature gradient present in the fluid directly causes a similar density gradient (as density is a function of temperature) which, by effect of the gravitational field, naturally induces a pressure difference that makes the fluid move by means of buoyancy. Hence, this type of flow is also called

buoyant flow. A thermal cavity will usually feature two distinct walls, one hot and one cold, while the others are typically adiabatic. Variations of the case may include a cavity with an obstacle inside, inclined cavities (with a non-orthogonal gravitational field), or simply a plain box. This problem is illustrative of many engineering problems that feature fluid flow with heat transfer and has motivated many studies surrounding it. As such, the literature is filled with thermal cavity cases and it has become a staple of CFD benchmarks.

Many of the studies found on thermal cavities are computer simulations. Davis (1983) is one of the first well known studies of this problem, featuring several benchmarks for the laminar thermal cavity with $10^2 \leq Ra \leq 10^6$. Markatos and Pericleous (1984) then extended this analysis to Rayleigh numbers up to 10^{16}, which include turbulent flow that is modelled with $k - \epsilon$. Fusegi *et al.* (1991) produced results for a tridimensional cavity, being known as one of the first that used a 3D domain. The thermal cavity was also studied in MFLab several times, as can be noted from Padilla, Lourenço and Silveira Neto (2013); Duarte (2018); Damasceno, Santos and Vedovotto (2018); and Chiumento (2024).

An experimental study on the thermal cavity was executed by Salat *et al.* (2004), consisting of a three dimensional cavity filled with air with tigthly controlled properties from which data of the flow field was captured. Temperature field was measured by thermocouples, while velocity data was obtained by Laser Doppler Anemometry. Due to physical constraints, the flow inside the cavity couldn't be made laminar, and thus it consists of a turbulent flow analysis with $Ra = 1.5 \times 10^9$. The cavity of this experiment is referred to as Salat's Thermal Cavity, and was one of the benchmark tests for this work, chosen by virtue of being based on real world experimentation.

The authors also followed with a CFD reproduction of their experiment, running a DNS simulation with Chebyshev spectral method and LES with a finite volume model. This experiment produced an investigation of computational model optimization to obtain accurate results in regards to experimental data. The authors researched a series of new models and considerations that might improve the accuracy of the computational model, comprising the following publications: Sergent *et al.* (2013b), Sergent *et al.* (2013a) and Xin *et al.* (2013). One of the conclusions of the authors was that radiative heat transfer, even in this low temperature cavity without participating media, had significant influence in flow properties; the inclusion of a radiative heat transfer model with proper boundary conditions for the walls significantly enhanced the accuracy of their computer models. Another important aspect was considering that some boundaries aren't perfectly adiabatic; as such, they tried modelling them with an imposed Dirichlet boundary condition consisting of a prescribed temperature function $T(x)$. They also tested the use of Conjugate Heat Transfer (CHT) for modelling these boundaries adequately.

One of the first works to introduce a thermal cavity with effects of radiative heat

transfer was Yücel, Acharya and Williams (1989). The authors modelled a bidimensional thermal cavity with a hot wall that is double the temperature of the cold wall, a Rayleigh Number of 5×10^6 and a Planck number of 0.02, producing numerical results that show strong influence of radiative heat transfer. For example, the flow becomes unicellular if the optical thickness is high enough, whereas without radiation one can observe a bi-cellular flow at this Rayleigh number. It also diminishes the advective heat transfer through the hot wall, although the radiative heat flux and overall heat flux through this domain are much higher. It also intensifies the velocities of the cavity, causes the temperature stratification in the core of the cavity to be less apparent and amplifies the average temperature of the domain; colder regions are more restricted to regions close to the cold wall. The simplicity and representativeness of this case led it to be used in the studies of this work as a benchmark. This thermal cavity is also mentioned here as Yücel's Thermal Cavity.

Numerical studies on thermal cavities with radiation effects were performed by Lari *et al.* (2011) and Lari *et al.* (2012). Much like with Yücel's cavity, the authors simulated a bidimensional thermal cavity, this time with a smaller temperature gradient and a broader range of Rayleigh numbers and optical thicknesses. Their results were similar to those of Yücel, Acharya and Williams (1989). In Lari *et al.* (2012), the authors repeated the analysis using a FSK spectral model in a cavity with H_2O and CO_2 concentrations that are representative of combustion systems. As in Xin *et al.* (2013), their results have demonstrated that radiation effects in the thermal cavity, even at low temperatures, has significant impact in the results, evidencing yet again that radiation plays an important role in thermal cavities. The authors also evidenced that spectral modelling with multiple bands may yield different results than with a gray model, although the authors argue that gray models may be applicable in specific analysis through careful modelling.

In most of these thermal cavities with radiative heat transfer, adiabatic boundaries are present. As mentioned in Section 3.11, this condition is significantly more complicated to establish in radiative cases, as it is a non-zero Neumann boundary condition that is a function of the radiative intensity. This is further aggravated by the spatial meshes being separate, requiring special interpolation treatment on the boundaries. This aspect is discussed in some of the publications here, but not as well emphasized.

4.3 Coupling of CFD and radiative heat transfer

Fluid simulations can be described as numerically solving a system of partial different equations that describe the balance of physical properties like mass, linear momentum, energy and chemical species. The existence of phenomena like turbulence or chemical reactions further complicates the issue by requiring higher spatial and temporal resolutions. Solving these equations requires finding corresponding three dimensional scalar

and vector fields that satisfy the problem at each time-step with high enough spatial resolution. CFD software is built with this in mind; For example, MFSim utilizes adaptive meshing and immersed boundary methods to efficiently capture turbulence information while avoiding unnecessary refinement; it also utilizes parallelization algorithms and solvers that are well adjusted for solving fluid flow, like the multi-grid method (Villar, 2007).

Radiative heat transfer, in the context of combustion systems in general, can be described as computationally solving a Radiative Transfer Equation that is defined by the fluid dynamics. Usually, the temporal term of this equation can be dropped. The challenge then becomes, in the context of non-gray media, developing a solver for a six-dimensional integro-partial-differential equation and coupling it with the algorithm that deals with the CFD part. The different physics of the problem creates different computational requirements; for example, the fields utilized in the RTE (temperature, pressure, species concentrations and radiative heat fluxes) tend to be more homogeneous and require less spatial resolution. They also tend to evolve more slowly, which is why temporal term of the RTE can be dropped; in fact, the RTE itself usually does not even need to be solved in each time-step. The existence of the directional and spectral dimensions, however, makes the problem heavier computationally, as it requires the RTE to be solved for multiple bands and directions. In deterministic solvers, like DOM and FAM, the radiative intensity field can get orders of magnitude larger than an equivalent scalar field in the three-dimensional mesh it is stored in. Similarly, solving several bands means solving an already expensive problem several times. As such, computational time and memory costs can get higher than even the ones from CFD solvers.

Several different approaches have been developed over the last decades to couple CFD and radiative transfer codes and they can be broadly categorized in a few different manners:

- **Integrated or segregated:**
  - **Integrated:** broadly refers to whether the solvers are integrated as part of the same software package. In this situation, it is usual that the radiation algorithm is built upon already existing code for the CFD and is treated as an extra physical model that can be used for its flow simulation. They share the same basic libraries for meshing, for solvers and for parallelization. They each can not be run separately and usually share the same spatial mesh.
  - **Segregated:** the CFD and radiation solvers are their own separate software packages. They may share common libraries, but can be run and be developed independently of each other. As they are both independent, they usually have different implementation of solvers and parallelization techniques, and require

interface code to be run together. They also usually have meshes that are separate from each other.

- **Shared or separate spatial mesh:** refers to whether the same spatial mesh is applied for both CFD and radiation, or not. As the spatial mesh for the CFD usually requires higher spatial resolution, utilizing a coarser mesh for radiation helps mitigate computational costs, when considering the interpolation and communication costs between the meshes.

- **Sequential or desynchronized:** in sequential coupling schemes, only either the CFD or the radiation solver can run at a time while the other waits; in other words, they are each run sequentially, one after the other. In desynchronized schemes, they run simultaneously (Figure 28), a feat that can be achieved due to the fact that the temperature, pressure and chemical species fields in CFD usually evolve so slowly that the RTE can be run only once for a series of CFD time-steps. In this approach, the RTE solver receives the input fields and returns the resulting radiative heat fluxes to the CFD solver several time-steps afterward; that is, the field comes with a delay (hence desynchronized) and does not represent the exact state of the fluid dynamics, which may lead to inaccuracies (Zenou, 2025). Nevertheless, de-synchronization allows for a substantial reduction in solver time and is usually employed with acceptable accuracy.

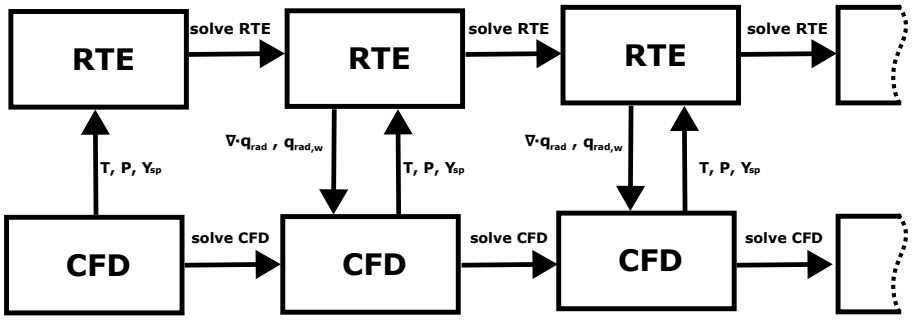

(a) Concurrent coupling.

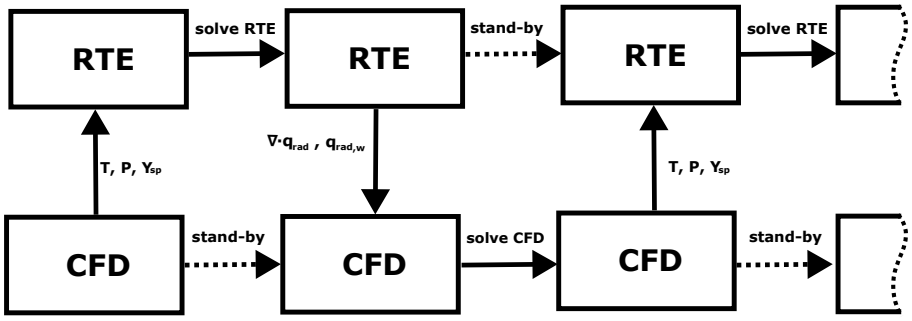

(b) Staggered coupling.

Figure 28 – Flowcharts depicting the differences between a staggered and concurrent coupling. Figures adapted from Rodrigues (2023) and Zenou (2025).

Examples of the integrated solver methodology can be found in softwares like AnSys Fluent (ANSYS INC., 2025), OpenFOAM (OpenFOAM Foundation, 2025) and FDS (McGrattan *et al.*, 2013). The MFSim-RTS coupling presented in this work, as well as the AVBP-Rainier coupling (Zenou, 2025) are examples of segregated couplings: they are separate code bases that can run independently. AVBP is a software suite for reactive turbulent compressive multispecies flows (Schonfeld; Rudgyard, 1999) developed by CERFACS, while Rainier is a Monte Carlo based radiation solver developed at EM2C Laboratory (Zhang, 2011). They are present in a series of studies on CFD-radiation couplings performed at EM2C, usually with an emphasis in combustion, such as: Zenou (2025), Torres (2021), Palluotto (2019), Rodrigues (2018), Refahi (2013) and Zhang (2011), all of which feature coupled radiation-CFD combustion problems. Santos *et al.* (2008) shows the result of a turbulent premixed propane-air flame solved by means of a coupling of AVBP with RADIATION using CORBA as the coupling software, representing a precursor to the now established AVBP-Rainier coupling. Delort-Laval (2023), Armengol (2019), Scoggins (2017), Soucasse (2013) and Zhang (2013) are also cases of CFD-radiation couplings with other simulation software applied to non-reactive flows.

MFSim-RTS, as well as the couplings employed by EM2C described in the paragraph above, allows the user to utilize separate spatial meshes. A particular case is that of Armengol (2019), in which the radiation mesh is defined by grouping cells from the CFD mesh into a coarser cell, essentially making them different but topologically dependent. This is similar to the multi-level methodology employed by Mota (2023) in MFSim, which assigns different physical levels of the MFSim mesh to different phenomena. In the MFSim-RTS coupling, the spatial meshes are defined independently of each other.

Other couplings that employ different mesh sizes for CFD and radiation include the ones utilized by Xin *et al.* (2013), Lari *et al.* (2011) and Lari *et al.* (2012), who utilized this technique in the study of thermal cavities. An interesting trend from the literature is that the spatial mesh for the radiation problem has usually at least about an order of magnitude less nodes than the CFD mesh, as can be seen in Armengol (2019), as well as the previously cited Lari *et al.* (2011), Lari *et al.* (2012) and Xin *et al.* (2013).

Desynchronized couplings between CFD and radiation solvers are quite common as they help in considerably reducing the computation time of a simulation, as noted by authors such as Armengol (2019) and Zenou (2025), and date as far back as Santos *et al.* (2008). The main concern in these couplings is defining the interval of time-steps between each data exchange operation in order to both ensure cost performance and stability. Too large of a coupling interval can result in numerical instabilities or inaccuracies from utilizing very outdated fields, while small intervals may increase the computational cost unnecessarily. Ideally, the coupling interval should be no higher than the amount of time-steps the radiation solver takes to finish its calculations; otherwise, it stalls and

stands by while waiting for new field data, resulting in time as well as precision losses. As a rule of thumb, the coupling periods that are allowed varies according to the problem in question, and a discussion on how they can be estimated can be found in Armengol (2019) and Zenou (2025).

Extrapolation techniques may also be applied to the radiative heat fluxes to ensure that they evolve more smoothly through the fluid simulation's time-steps, instead of being updated only in discrete intervals. This allows for higher coupling intervals while maintaining accuracy. Zenou (2025) noted that this technique can be applied successfully without loss of accuracy up to a certain coupling period. Overall, desynchronized coupling seems to be the norm in the EM2C implementations, with the gain in computational cost outweighing the possible inaccuracies of the methodology.

Sequential coupling may also employ the same delay method, where radiation is only solved once over an interval of time-steps, with similar implications regarding how this interval should be set as well as the inaccuracies it may give. The difference here is that the results are synchronized: the radiative heat fluxes received by the CFD solver are based on the same flow state given as input to the RTE solver, rather than based on the flow state from a previous time-step. They are just kept at the same value (or may also be extrapolated) until the next time-step where new heat fluxes are set to be calculated. This strategy also helps reduce computational cost and is employed by the MFSim-RTS coupling, which is sequential.

4.4 MFSim

MFSim is a multiphysics CFD software developed by the Fluid Mechanics Laboratory of the Federal University of Uberlândia since 2007 in partnership with Petróleo Brasileiro S.A. Some of its core features include adaptive mesh refinement (AMR), usage of immersed boundary (IB) methods for modelling complex geometries, multi-grid based solvers, and running on distributed computing platforms using MPI. A consequence of its usage of IB with AMR is that its main, Eulerian domain, consists of a cuboid containing a block-structured mesh. Coupled with its MPI parallelization capabilities, MFSim can effectively run complex, large, industrial-grade problems with reasonable costs. It is written primarily in FORTRAN and C.

4.4.1 Overview

MFSim employs a series of turbulence models described in works such as Damasceno, Vedovotto and Silveira Neto (2015), Elias (2018) and Catta Preta (2023). It is also capable of modelling multiphase flows, as shown in Souza *et al.* (2022), Pivello *et al.* (2014) and Barbi (2016). Melo (2017) shows a study on the implementation of thermal effects in

the Immersed Boundary Method (IBM) used in MFSim. Other good descriptions of the IBM can be found in Vedovotto, Serfaty and Silveira Neto (2015), in Magalhães (2022) and in Ribeiro Neto (2021), the latter of which uses a Ghost Cell methodology. Development and simulations on compressible flows with Mach numbers ranging from 3×10^{-4} to 3 were carried out by Chiumento (2024). The inner workings of its Adaptive Mesh Refinement and Multigrid solver can be found in the work of Villar (2007).

Discrete Phase Models (DPM) can be used in MFSim for modelling sprays, featured in the studies of Santos (2019), Pinheiro (2022) and Martins (2023). Combustion modelling was developed by Vedovotto (2011), Damasceno (2018) and Elias (2023), the latter which studied the development of a novel virtual mechanism technique for modelling chemical reactions. Finally, Fluid Structure Interaction (FSI) has been dealt with in works such as Ribeiro Neto (2021), Morales *et al.* (2023) and Oliveira (2025).

In other works, MFSim was also used to study corrosion in pipelines (Mota, 2023) and in non-Newtonian flows applied to forensic blood analysis (Vasconcellos, 2024). Last, but not least, radiative heat transfer modelling started with Rodrigues (2023) and is on-going in the present work.

This brief summary of MFSim's history shows how it has been applied in diverse contexts since its inception and illustrates its on-going development, growth and capabilities. Not only is MFSim excellent as an instrument of academic research, it is capable enough of being applied to real world industrial problems, assisting with important process optimization and decision making.

4.4.2 Mesh description

The base building block of MFSim's mesh are its **patches** (Figure 29). Each patch represents a Cartesian block with n_x, n_y and n_z cells in the x, y and z directions, respectively. The communication between each patch, as well as the definition of boundary conditions on the Eulerian domain, is made possible by means of **ghost cells**, which are also known as halo cells. These cells exist beyond the patch's domain, surrounding it, and simply contain information on their nodes such that any stencil performed inside the patch can be correctly calculated. They also define a buffer zone that enables inter-level and inter-process communication. This approach characterizes a full volume discretization, which contrasts with half-volume discretization, where ghost cells are not used and values are instead stored in the face itself when defining boundary conditions. An example of numerical software that uses half-volume discretization is OpenFOAM, and also RTS itself.

MFSim's patches are separated by levels and stored in a linked-list. Each level is stored from 1 to `ltop` and the mesh gets progressively finer with each level increase. Levels are also distinguished between physical and virtual levels. The physical levels

range from `lbot`, the lowest physical level, to `ltop`, the highest level in the mesh. Levels below `lbot` are virtual and are only used by the multi-grid solver. Many algorithms present in MFSim typically revolve around iterating on the mesh's levels and, for each level, iterating on its patches.

The parallelization is performed by dividing patches between different processes. Globally, each process has a strict subset of coordinates within the whole domain, such that each point in the mesh is assigned to only one process. This makes it easy for each process to determine whether a point is within it or not. Likewise, each patch also knows if a point is within its subdomain or not. If it is, then interpolating field values from this patch to said point is possible, as the patch contains all the information needed to assemble the stencil. That's how multi-process interpolation is done: each process occupies itself only with points belonging to it, assigns a patch for each point, and then uses the patch's information to calculate the field value at that respective point. The interpolated information can then, for example, be written on disk or communicated to other processes via MPI.

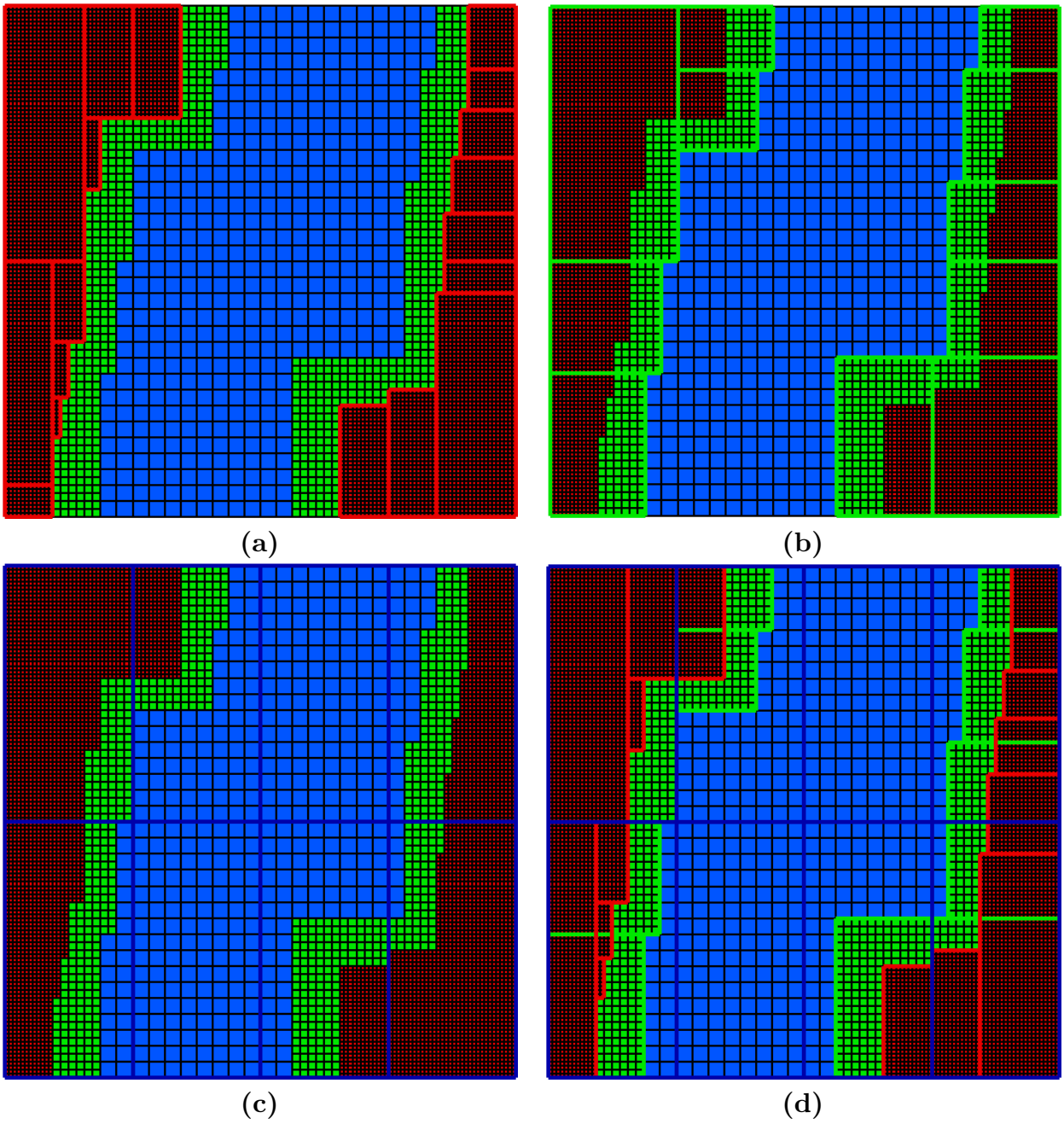

Figure 29 – Illustration of an MFSim mesh with three physical levels. It displays the physical levels `lbot`, `lbot+1` and `ltop` colored in, respectively, blue, green and red. The patches are bounded by lines of the same color. (a) shows the patches in `ltop`, (b) the patches in `lbot+1`, (c) the levels in `lbot` and (d) shows all patches together.

4.5 RTS

RTS (Radiative Transfer Simulator) is a deterministic radiative heat transfer solver developed in MFLab that can be set to use the Spherical Harmonics P1 Method, the DOM or the FAM. It is capable of modelling gray media, either by user-defined values or WSGG modelling (Bordbar; Węcel; Hyppänen, 2014), or non-gray media by means of the

same WSGG model. Finally, it has models for non-isotropic scattering. Its development and features are thoroughly documented in Rodrigues (2023).

An important aspect of RTS is the fact that it was developed as its own separate software. This facilitates development and usage focused on radiation modelling, which by themselves are complex enough and comprise their own particular challenges, as discussed previously. This approach facilitates the spatial mesh separation between MFSim and RTS that is developed in this work: solving the RTE usually does not require the expensive and complicated spatial meshes that are typical of CFD; as such, it can use cheaper, coarser spatial meshes. As a deterministic RTE solver also needs to discretize in the angular and spectral spaces, which can easily increase the total mesh size by $100\times$ the size of the spatial mesh, this decoupling can be quite beneficial. Another advantage of this design is that it opens RTS to be coupled with any platform, as long as a communication layer is implemented. Thus, RTS presents itself as quite a promising general purpose RTE solver.

For as promising as it is, though, it is still lacking in a few areas:

- Currently, it only works in serial (although, with the coupling developed in this work, MFSim runs normally through its MPI parallelization);
- Currently, it can only model rectangular prism (cuboid) domains. It would need either IB modelling or unstructured mesh support for tackling more complex geometries;
- Currently, it only contains the WSGG modelling from (Bordbar; Węcel; Hyppänen, 2014). Other spectral models, such as FSCK or LBL are lacking;
- It can only handle domain boundaries that are opaque and diffusively reflecting. Specular reflection and periodic boundaries are not yet supported;
- It does not feature turbulence models for CFD coupling in turbulent flows. In turbulent flows, average fields are simply sent directly to RTS the same way as in laminar cases. This was not a problem for the present work.

4.5.1 Mesh description

RTS's spatial mesh structure is quite simple: it consists of a structured mesh, divided in n_x, n_y and n_z cells in, respectively, the x, y and z directions. In other words, RTS's mesh can also be thought of as a single MFSim patch. All mesh points are stored in three vectors, one for each direction. As such, mesh information is quite light in memory. Each RTS field is allocated to contain all available points in the mesh; thus, for a mesh with $n_x \times n_y \times n_z$ cells, a field is stored in a 3D array of size $(n_x + 2) \times (n_y + 2) \times (n_z + 2)$,

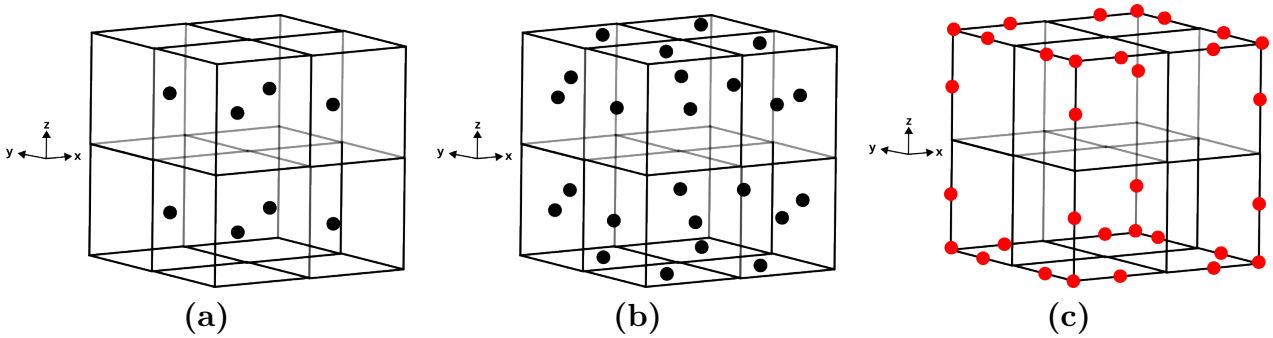

Figure 30 – Illustration of an RTS mesh in 3D. (a) shows the cell centers, (b) the face centers and (c) shows the edge points.

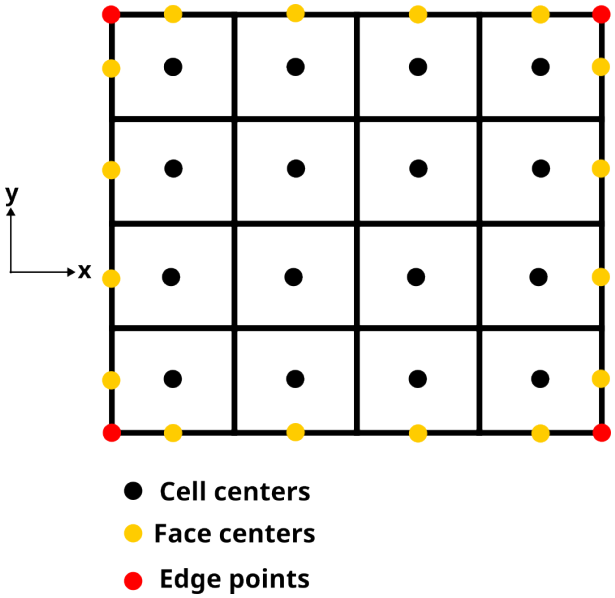

Figure 31 – Illustration of an RTS mesh in 2D with all its points shown.

with the extra cells representing the boundary faces. Each point in the mesh can be divided into three categories:

- A cell centroid;
- A face centroid;
- An edge point.

An illustration of these points in a 3D RTS mesh can be seen in Figure 30, and in a 2D mesh in Figure 31. Edge points are points contained within the domain's edges, which can be either the four corners of a 2D mesh, or all edges that form the cuboid of a 3D mesh. No relevant information is actually stored in them, and they are simply ignored by the rest of the software. They do, however, exist and each field has some value stored in them. The choice for structuring the data in this way can be traced back to ease of programming, at the cost of redundant data being stored.

4.5.2 Solver algorithm

RTS uses a Gauss-Seidel sweep algorithm for determining the I field when using DOM or FAM, much like Moustafa (2015). The calculation is split into octants, where each octant is a subset of the angular space where all angular directions in them have the same signal in their respective i, j and k components. The octant sweep begins at the corner where the boundaries emitting incoming radiation are present, and goes all the way to the corner of the boundaries that are receiving this beam. For each angle in the octant, the spatial dimension is swept in order, using the newly calculated value in a cell to determine the value in the next ones. Thus, for each iteration of the solver, each octant is swept one by one. In each octant, each angular direction's spatial domain is swept, cell by cell. After calculating all the new values of I, the maximum relative difference between the new values and the old ones is evaluated: if it is less than the set convergence criteria, or if too many iterations have been executed, the solver loop is halted and the final result is given. With the I field in hands, the derived $\nabla \cdot q_{rad}$ and $q_{rad,w}$ can be determined. This process is summarized in Algorithm 1.

Algorithm 1 Summary of RTS's solver algorithm for DOM and FAM.

input Mesh, phase function, physical properties
output Radiative intensity field I

while not converged **do**

  Update incoming boundaries of each octant:
  for each incoming direction D **do**
    for each boundary cell BC **do**
      for each outgoing direction D' **do**
        I(BC,D) += $I(BC, D') \cdot w$
      end for
      I(BC,D) = $\frac{I(BC,D)}{\pi}$ + $I_b(BC)$
    end for
  end for

  Update S_M with new in-scattering values:
  for each direction D **do**
    for each cell C **do**
      for each direction D' $\neq$ D **do**
        $S_M(C) += I(C, D') \cdot \Phi(D', D)$
      end for
      $S_M(C) += I_b(C)$
    end for
  end for

  Sweep domain:
  for each direction D **do**
    for each spatial cell C **do**
      Determine I(C,D) from C's neighbours
    end for
  end for

  Update outgoing boundaries of each octant:
  for each outgoing direction D **do**
    for each boundary cell C **do**
      I(C,D) = I(C-1,D)
    end for
  end for
end while
return I

4.5.3 First iteration of coupling with MFSim

An initial coupling between MFSim was developed prior to this work. The coupling between MFSim and RTS is, after all, paramount, and the reason for RTS's existence. It had severe limitations, however, due to focus being put in making sure RTS correctly

modelled and solved thermal radiation problems:

- It forced MFSim to run in serial, like RTS;
- It forced MFSim to use the same mesh as RTS.

As such, the cases in which the MFSim-RTS coupling could be used were severely limited to cheap cases where the fluid dynamics could be run in serial with a simple Cartesian mesh. Furthermore, to the best of the author's knowledge, no testing or verification was performed on this old coupling. A summary of this coupling algorithm can be seen in Algorithm 2.

Algorithm 2 Old CFD-radiation coupling.

MFSim must be **run in serial**, with the **same mesh as RTS**, and **without adaptive mesh refinement**
for each time-step T **do**
  if radiation should be solved in T **then**
    Solve RTE
    Update $\nabla \cdot q_{rad}$ and $q_{rad,w}$
  end if
  Use $q_{rad,w}$ to calculate heat flux boundary conditions
  Apply $\nabla \cdot q_{rad}$ to the energy balance equation and solve it
  Solve the flow for the current time-step T
end for

5 Methodology

This chapter describes the new communication layer between MFSim-RTS that was developed in this work. This new interface allows the separation of the spatial mesh of both codes while also enabling MFSim to run in parallel. In-depth details regarding how information is exchanged between the two meshes, the interpolation methods that were used, and how data is communicated across different processes will be given below.

5.1 Coupling Interface Between MFSim and RTS

The first step for setting up the interpolation of an MFSim field to an RTS field is initializing the RTS mesh on all processes. Although only process zero will actually contain all RTS field data and solve the RTE, mesh information is necessary to be known on all processes for the interpolations to work. Next, a data structure containing important metadata for the interpolation, henceforth known as `interp_map`, must be filled. This data structure is unique to each process and cell centroid of the RTS mesh, and contains the following information:

- Whether the cell centroid is contained in that process or not;
- Whether the point is an edge point (that is, if it is contained in one of the edges of RTS's domain);
- The highest level of the MFSim mesh that contains said point;
- A pointer to the highest level patch that contains this point.

This data structure must be updated whenever a re-meshing occurs. Its information is crucial for interpolation, not only for performing it, but also for the algorithm to know if it even should perform an interpolation. If the point scanned is an edge point (the red dots in Figure 31) for instance, its value should be equal to zero, as RTS does not store information on its edges; field points in this region exist simply due to choices on how the field data should be stored. Furthermore, if a process tries to analyse or interpolate a point that is not contained in it, unexpected behaviour or crashes are bound to happen. An overview of how `interp_map` is assembled can be seen in Algorithm 3.

With the metadata assembled, interpolation can begin. The interpolated field will be stored in a standard RTS 3D array, whose values are set as equal to zero at the beginning of the interpolation. This array exists in all processes. Then, an iteration is performed through each point in the RTS mesh. If the point is contained in the process,

Algorithm 3 Algorithm for constructing or updating `interp_map`.

```
1: input MFSim mesh and RTS mesh
2: output interp_map
3:
4: for each level L do
5:   for each patch P in level L do
6:     for each MFSim cell C in patch P do
7:       for each RTS node N do
8:
9:         if not interp_map[N]->is_in_proc then
10:          continue
11:        end if
12:        if interp_map[N]->is_edge then
13:          continue
14:        end if
15:
16:        interp_map[N]->is_in_proc ← in_proc(C)
17:        interp_map[N]->is_edge ← is_domain_edge(C)
18:
19:        if is_in_patch(P, N) then
20:          interp_map[N]->patch_pointer ← pointer(P)
21:          interp_map[N]->level ← L
22:        end if
23:
24:      end for
25:    end for
26:  end for
27: end for
28:
29: return interp_map
```

and if it is not an edge point, a trilinear interpolation is performed on that point, and its result is stored in said 3D array. Finally, when all processes have interpolated all data they can, an `MPI_REDUCE` is performed, sending the entire field to process 0. A simplified schematic of the stencil utilized is showcased in Figure 33. Field value from neighbouring cells to the point to be interpolated that may not be contained in the current process can still be accessed due to being stored as buffer zones in that process. A summary of this process is shown in Algorithm 4.

The reverse path, that is, taking field values from RTS to MFSim, is performed in a similar fashion. First, the RTS field to be interpolated is sent to all processes by means of an `MPI_BCAST`. Then, the MFSim domain of that process is iterated through, level by level, patch by patch, cell by cell. For each point, another trilinear interpolation is calculated. This time, to assemble the stencil, a binary search algorithm is implemented to figure out the nearest node to the point from the RTS mesh; the rest of the nodes

Algorithm 4 Algorithm for interpolating an MFSim field to RTS.

```
input interp_map, RTS mesh and MFSim field
output RTS field interpolated from MFSim

for each RTS node N do

  if not interp_map[N]->is_in_proc then
    continue
  end if

  if interp_map[N]->is_edge then
    RTS_field[N] = 0.0
    continue
  end if

  level ← interp_map[N]->level
  patch ← interp_map[N]->patch_pointer
  RTS_field[N] ← interpolate(level, patch, MFSim_field)
end for

return RTS_field
```

are indicially calculated based on it. This process can be seen in Algorithm 5 and an illustration of the stencil employed by it is displayed in Figure 34.

Algorithm 5 Algorithm for interpolating an RTS field to MFSim.

```
input MFSim mesh, RTS mesh and RTS field
output MFSim field interpolated from RTS

for each level L do
  for each patch P in level L do
    for each MFSim cell C in patch P do
      MFSim_field ← interpolate(RTS_mesh, RTS_field, C)
    end for
  end for
end for

return MFSim_field
```

To complete the radiation coupling, the radiative heat fluxes on the wall must be calculated as well. This consists of a surface scalar field that is stored in each face centroid of the RTS domain's boundary (the yellow dots in Figure 31), and that must be interpolated to each MFSim face. The interpolation is performed in a similar fashion to the volumetric fields: $q_{rad,w}$ is sent to all processes with `MPI_BCAST` and a binary search algorithm is used to assemble the stencil. The main difference is that a bilinear interpolation is utilized, due to the field belonging in a 2D space. As such, the stencil

utilized is similar to the one illustrated in Figure 34. This interpolation process is described in Algorithm 6.

Algorithm 6 Algorithm for interpolating an RTS face field to MFSim.

```
1: input MFSim mesh, RTS mesh and RTS face field
2: output MFSim field with face data interpolated from RTS
3:
4: for each level L do
5:    for each patch P in level L do
6:       for each MFSim cell C in patch P do
7:          if C is in boundary then
8:             MFSim_field[C] ← interpolate_face(RTS_mesh, RTS_field, C)
9:          end if
10:      end for
11:   end for
12: end for
13:
14: return RTS_field
```

A schematic of the communication process between MFSim and RTS is illustrated in Figure 32. The subscript next to the square brackets indicate the mesh in which the fields are contained. While MFSim runs on one or more processes, RTS runs only on process P_0. In the following section, a more in-depth mathematical description of the interpolations used is presented. This communication process is also represented in Algorithm 7, where it can be directly contrasted with the old interface described in Algorithm 2.

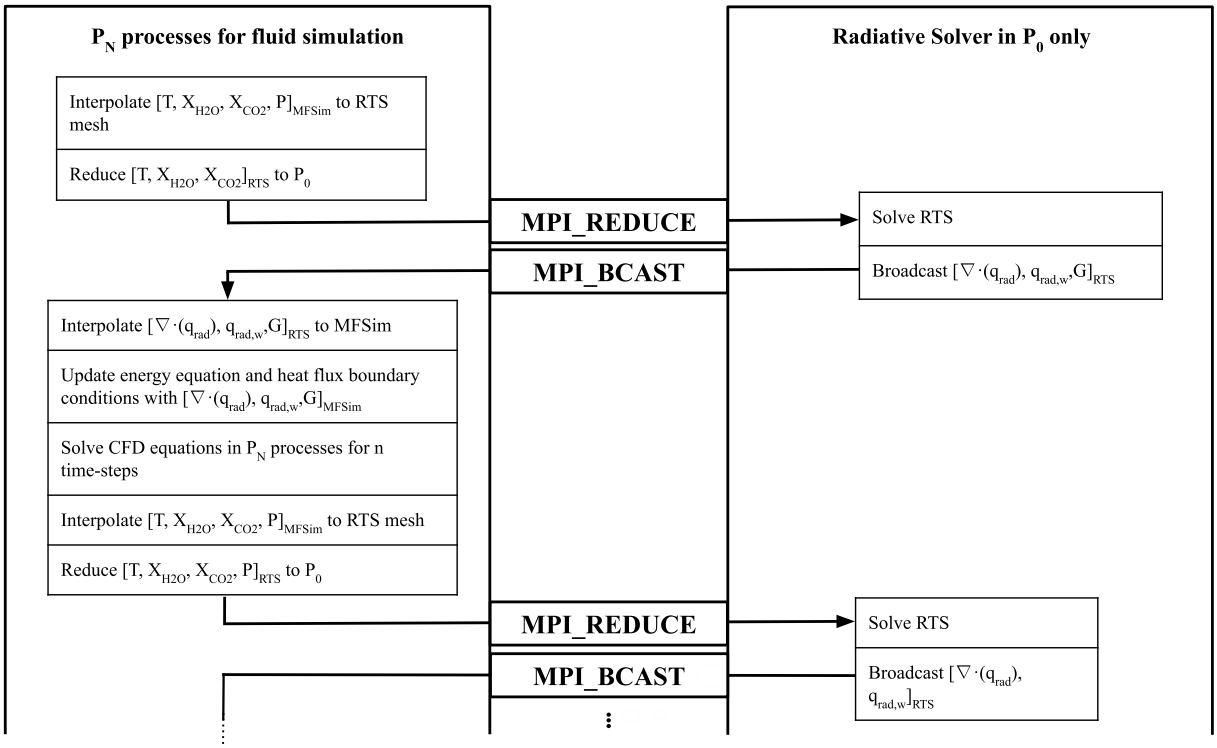

Figure 32 – Descriptive flowchart of the coupling between MFSim and RTS. The symbols inside the square brackets denote the fields in which the interpolation and communication procedures are being performed. The bracket's subscript denote the mesh in which they are stored.

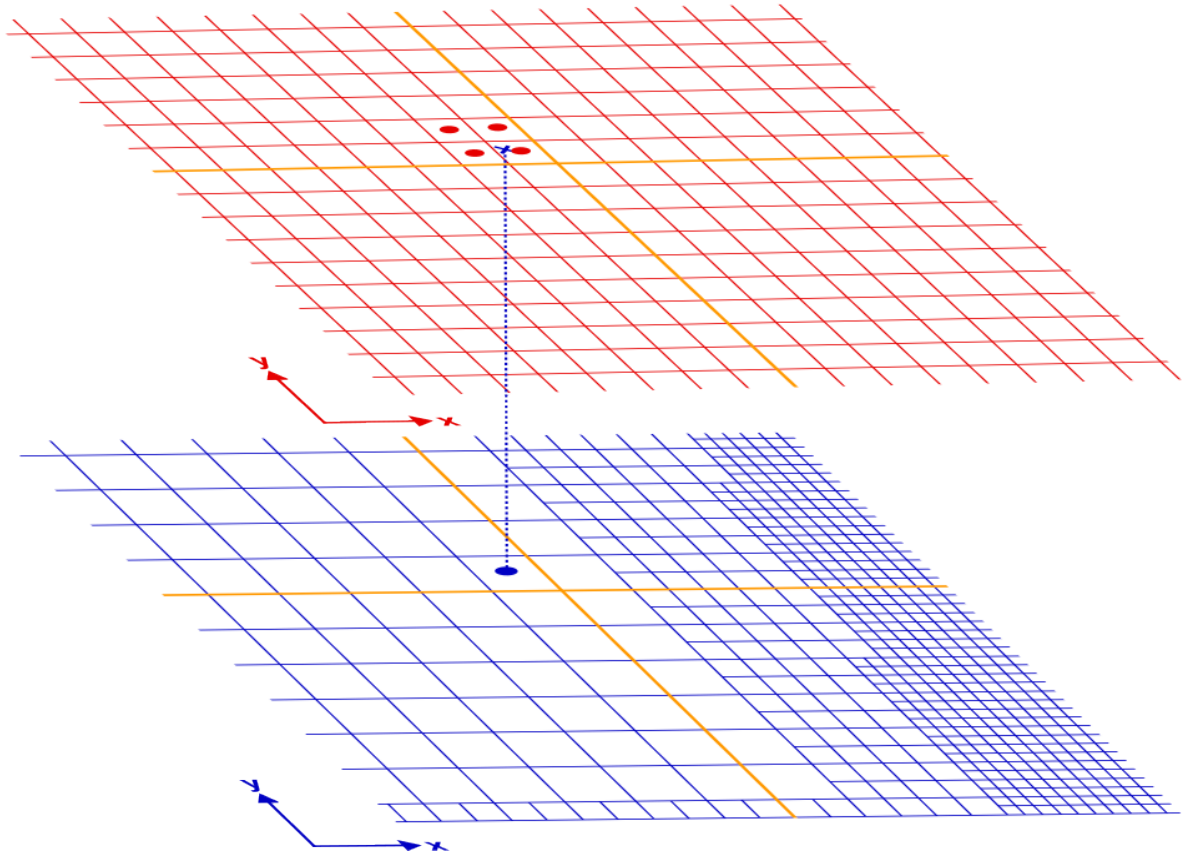

Figure 33 – Illustration of the stencil assembly for the RTS to MFSim interpolation.

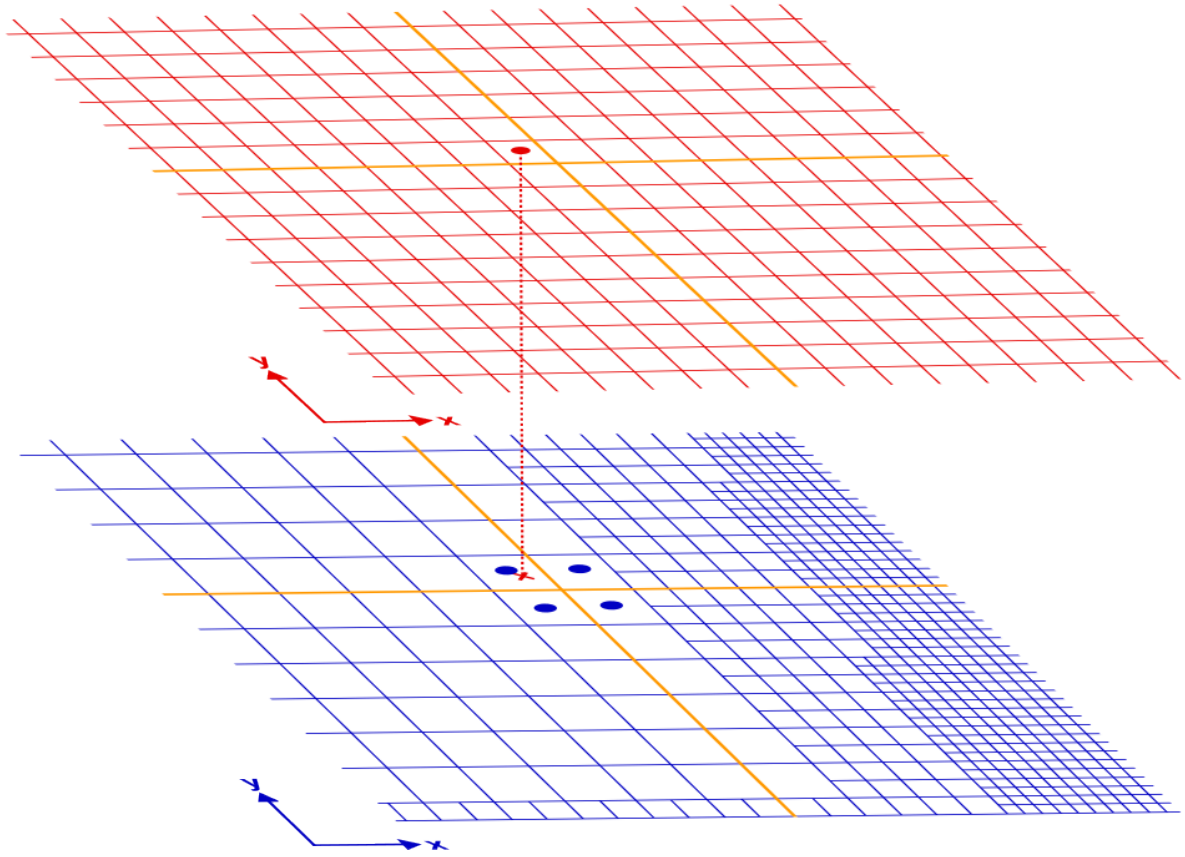

Figure 34 – Illustration of the stencil assembly for the MFSim to RTS interpolation.

Case	Total Simulation Time	Average Time of Time-step	Average Time Speed-up
1 process, 1 delay	5.32 hours	0.40 seconds	1.0×
1 process, 5 delay	2.87 hours	0.21 seconds	1.9×
4 processes, 1 delay	1.61 hours	0.12 seconds	3.3×
4 processes, 5 delay	57.22 minutes	0.07 seconds	5.7×

Table 1 – Summary of time benchmark tests of the CFD-radiation coupling algorithm. The same case was run on 1 or 4 processes, as well as with a radiation delay of either 1 (RTE solved each time step) or 5 (RTE solved every 5 time steps).

.

Algorithm 7 New CFD-radiation coupling.

MFSim can **be run in parellel** and **with adaptive mesh refinement**. RTS **runs in serial** and **with its own, separate mesh**
for each time-step T **do**
  if Radiation should be solved in T **then**
    Interpolate temperature field to RTS
    if gas module is on **then**
      Interpolate X_{CO_2}, X_{H_2O} and pressure fields to RTS
    end if
    `MPI_REDUCE` interpolated RTS fields to P_0
    Solve RTE
    `MPI_BCAST` $\nabla \cdot q_{rad}$ and $q_{rad,w}$ RTS fields to all processes
    Interpolate $\nabla \cdot q_{rad}$ and $q_{rad,w}$ to MFSim
  end if
  Use $q_{rad,w}$ to calculate heat flux boundary conditions
  Apply $\nabla \cdot q_{rad}$ on the energy balance equation and solve it
  Solve the flow for the current time-step T
end for

Overall, the interpolation process is effective and of relatively minor computational costs when compared to the performance gained from solving the fluid equations in parallel. Using the fluid solver in parallel, a sample radiative thermal cavity case run time is reduced by over 3 times. It can be further reduced by 1.7× by solving the RTE every 5 time-steps instead of each time-step, without significant difference to the final results (see Table 1).

5.2 Interpolation Operations

Since the two meshes used in the problem (those being the MFSim adaptive mesh and RTS's simple Cartesian mesh) are not identical, the coupling interface relies on linear interpolations to determine the discrete field values calculated by one of the solvers at points not contained in their mesh. Linear interpolations are fast and simple to

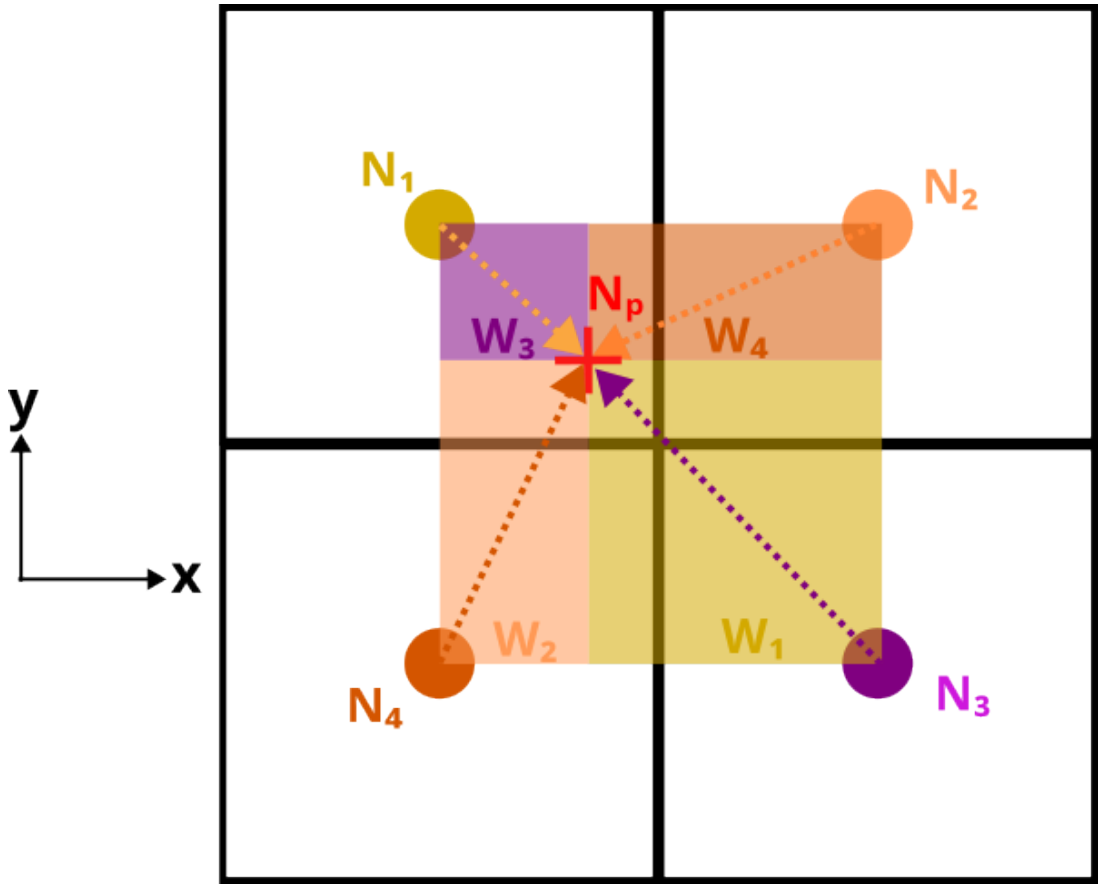

Figure 35 – Illustration of a bilinear interpolation.

implement, having already been used with success for MFSim's probe interpolations. In fact, the communication layer between MFSim and RTS leverages the algorithm already present for the probe calculations.

These linear interpolations are essentially a pondered average and can be generically expressed by the following sum:

$$T_p = \sum_n w_n T_n, \tag{5.1}$$

where T_p is the generic scalar field T at the unknown point p, T_n is the known field value at point n and w_n the weight associated to that point. The set of n points are selected such that they are the closest neighbours of p. For a 2D interpolation, 4 points are chosen in total which forms a bilinear interpolation (Figure 35); for a 3D interpolation, it takes 8 points as it does a trilinear interpolation (Figure 36). The interpolation as expressed by Equation 5.1 also has the following property:

$$\sum_n w_n = 1. \tag{5.2}$$

The algorithm for finding these points is as follows:

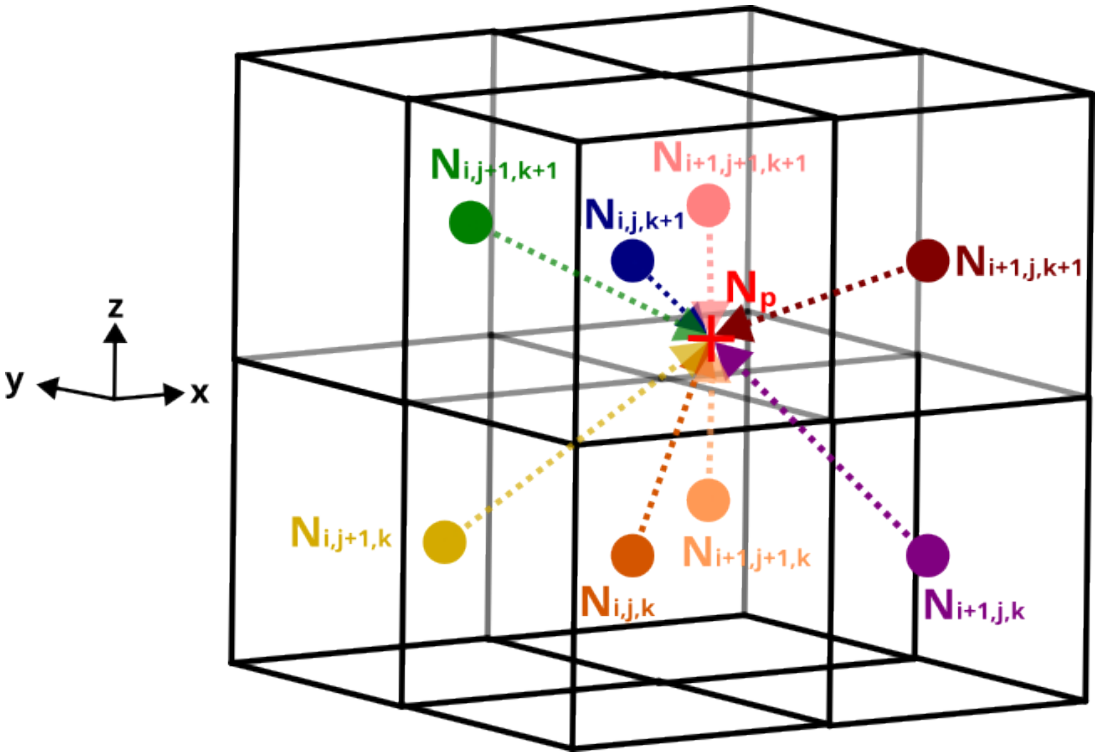

Figure 36 – Illustration of a trilinear interpolation.

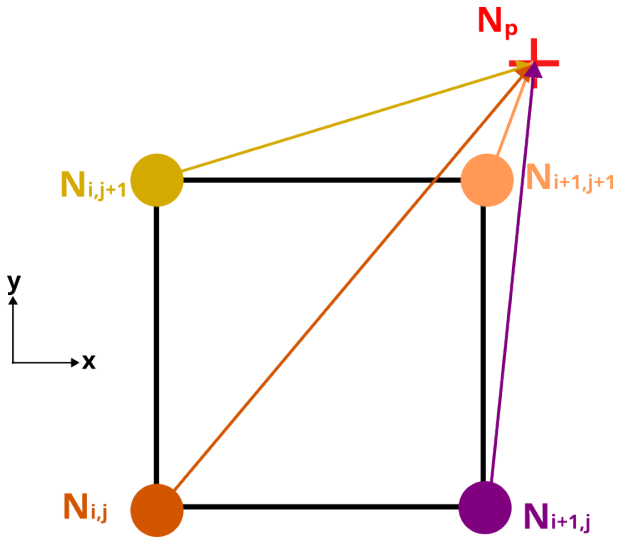

Figure 37 – Illustration of a bilinear extrapolation.

1. Find the point $p_1 = (x_i, y_j, z_k)$, which is the closest point of the known field mesh to the point to be interpolated;

2. As RTS's mesh and MFSim's patches are Cartesian, the other points of the set can be found by taking each of p_1's coordinates and adding one to their indices. That is, $p_2 = (x_{i+1}, y_j, z_k)$, $p_3 = (x_i, y_{j+1}, z_k)$, ..., going all the way to $p_8 = (x_{i+1}, y_{j+1}, z + k + 1)$. If the source mesh is adaptive, the highest refinement level is taken to ensure the greatest possible accuracy of the interpolation.

3. If one of these calculated coordinates do not exist due to existing beyond the upper boundary of the domain where field values are stored, they are simply replaced by their mirror points. For example, if p_1 is in the x direction east boundary, then $p_2 = (x_{i+1}, y_j, z_k)$ cannot exist and thus is taken to be $p_2 = (x_{i-1}, y_j, z_k)$. This configures an extrapolation, as illustrated by Figure 37. Extrapolation is performed on the RTS to MFSim interpolations to deal with values close to the boundary, while in the MFSim to RTS interpolations this is not necessary due to MFSim having ghost cells.

4. Once these points are found, the stencil is formed. From the stencil, the field's T_n values can be taken and the points' respective weights can be calculated accordingly. The closest these points are to the point being interpolated, the higher their weight will be, as shown in Figure 35.

5. With their weights in hand, the sum in Equation 5.1 can be performed and the value T_p of the field in the new mesh can be found.

Taking Figures 38 and 39 as reference, the following definitions can be established:

$$\Delta x_n = \begin{cases} x_{i+1} - x_p, \text{ if n = i} \\ x_p - x_i, \text{ if n = i + 1} \end{cases}, \tag{5.3}$$

$$\Delta y_n = \begin{cases} y_{j+1} - y_p, \text{ if n = j} \\ y_p - y_j, \text{ if n = j + 1} \end{cases}, \tag{5.4}$$

$$\Delta z_n = \begin{cases} z_{k+1} - z_p, \text{ if n = z} \\ z_p - z_k, \text{ if n = k + 1} \end{cases}. \tag{5.5}$$

Then, the weight for each point n for the 3D interpolation can be determined by the following equation:

$$w_n = w_{i,j,k} = \frac{\Delta x_n \cdot \Delta y_n \cdot \Delta z_n}{(x_{i+1} - x_i) \cdot (y_{j+1} - y_j) \cdot (z_{k+1} - z_k)}. \tag{5.6}$$

Similarly, for the 2D interpolation:

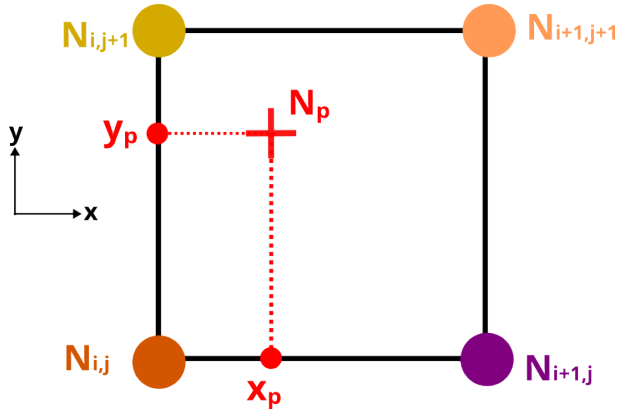

Figure 38 – Bilinear stencil with the target node N_P's coordinates annotated.

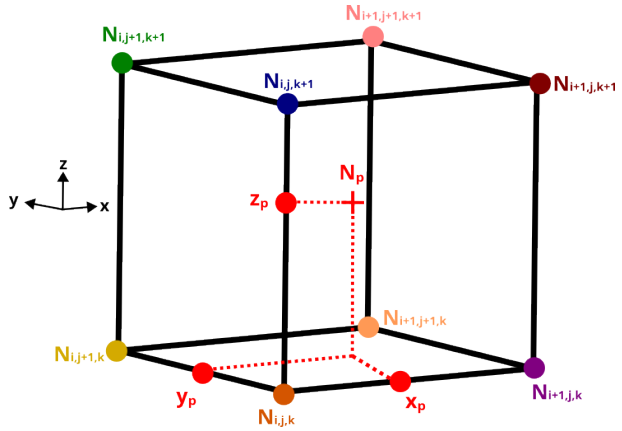

Figure 39 – Trilinear stencil with the target node N_P's coordinates annotated.

$$w_n = w_{i,j} = \frac{\Delta x_n \cdot \Delta y_n}{(x_{i+1} - x_i) \cdot (y_{j+1} - y_j)}. \tag{5.7}$$

The extrapolation follows the same formulas, except that point P is outside the box that bounds the stencil points, instead of inside, which will lead to Equation 5.2 not applying any more.

6 Results

This section discusses the application of the MFSim and RTS coupling on the numerical simulation of two thermal cavities, namely the Yücel and Salat thermal cavities discussed in Section 4.2. Their setups are detailed, and results are compared with the literature. Both feature significant effects of radiative thermal transfer, helping to shed light not only on the coupling's accuracy and performance, but also on the importance of radiation in heat transfer applications.

6.1 Yücel's Thermal Cavity

This problem, published by Yücel, Acharya and Williams (1989), consists of a 2D thermal cavity that is similar to the one presented in Davis (1983) with the added effect of radiative heat transfer. The authors discretized the CFD equations and the RTE with the FVM and used the DOM for the angular discretization. Solutions using the Spherical Harmonics P_1 were also presented. The equations adopted in the model are described in their dimensionless form.

The cavity can be mainly characterized by a few dimesionless parameters, some of which make part of its differential equations: the Rayleigh number, the Prandtl number, the Planck number (or the conduction-radiation parameter, see Section 2.5.12), the optical thickness of the media (Section 2.5.8), the scattering albedo (Section 2.5.9) and the emissivity of the walls. The first two numbers of this list come from the fluid dynamics of the problem and are also present in the classical problem, while the other four come from the added radiative transport.

The domain consists of a square or cubic domain in which opposite walls are set at different temperatures, while the other walls are set as adiabatic (Figure 40). The fluid velocity is set to zero in all walls, with the pressure receiving a zero Neumann boundary condition on all four walls. The emissivity of its four walls is set to 1 (i.e. they are all black). The Boussinesq-Oberbeck approximation is used to model the buoyant flow, with the specific mass being considered constant except for the Boussinesq term. The fluid of the domain is modelled as a gray gas with constant properties. In the MFSim-RTS implementation of this problem, the computational domain is pseudo 2D, utilizing two cells in the z direction and a symmetry boundary conditions to model 2D behaviour.

The following cases are presented in this work: no radiation, $\tau = 0.2$, $\tau = 1$ and $\tau = 5$. For all these cases, $Ra = 5 \times 10^6$, $Pr = 0.72$, $Pl = 0.02$ and no scattering is adopted, as summarized in the dimensionless numbers shown in Table 4. The cases are solved using the Finite Volumes Method with a DOM S_4 quadrature. The physical properties and

boundary conditions are summarized in Tables 2 and 3. This thermal cavity was used both for verifying the accuracy of the MFSim-RTS coupling and for measuring the its computational costs, as it is a simple, cheap to simulate case that illustrates well a flow with radiative heat transfer effects.

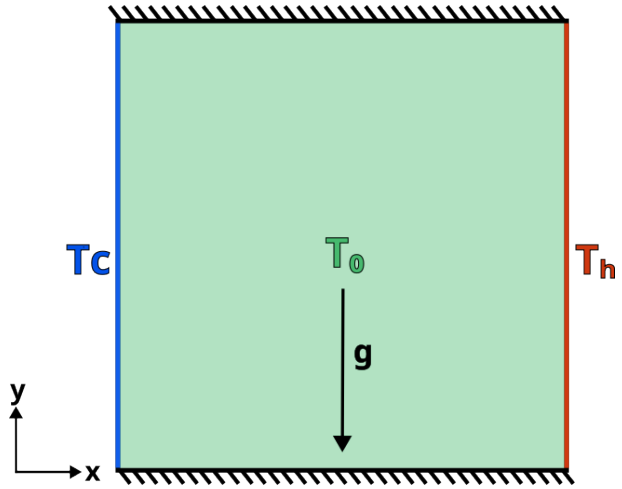

Figure 40 – Thermal cavity domain illustrated at time $t = 0\ s$.

Specific mass (ρ)	$2.34045\ \frac{m^3}{kg}$
Viscosity (μ)	$1.81702 \times 10^{-5}\ Pa \cdot s$
Gravity acceleration (g)	$9.81\ \frac{m}{s^2}$
Specific heat (c_p)	$1014.41\ \frac{J}{kg \cdot K}$
Thermal conductivity (k)	$2.56 \times 10^{-2}\ \frac{W}{m \cdot K}$
Expansion coefficient (β_V)	$1.92091 \times 10^{-3}\ \frac{1}{K}$
Hot wall temperature (T_h)	$694.115\ K$
Cold wall temperature (T_c)	$347.058\ K$
Initial temperature (T_0)	$520.586\ K$
Cavity length (L)	$0.04\ m$
Absorption coefficient (κ)	$5.0\ m^{-1}$, $25.0\ m^{-1}$ or $125.0\ m^{-1}$
Scattering coefficient (σ_s)	0.0

Table 2 – Physical properties used for modelling Yücel's thermal cavity.

6.1.1 Coupling interface performance

The Yücel thermal cavity with optical thickness $\tau = 1$ was run with different mesh configurations, with and without the WSGG model, as synthetized by Table 5. The WSGG model requires interpolating the X_{CO_2} and X_{H_2O} and pressure fields along with the temperature. The cases without gas modelling interpolate only the temperature to

Field	**West**	**East**	**South and North**	**Bottom and Top**
Velocity $[\frac{m}{s}]$	No-slip	No-slip	No-slip	$\frac{du_x}{dx}, \frac{du_y}{dy} = 0; u_z = 0$
Pressure $[Pa]$	$\frac{dp}{dx} = 0$	$\frac{dp}{dx} = 0$	$\frac{dp}{dy} = 0$	$\frac{dp}{dz} = 0$
Temperature $[K]$	694.115 K	347.058 K	$\frac{dT}{dy} = \frac{q_{rad,w}}{k}$	$\frac{dT}{dz} = 0$
Emissivity $[-]$	1	1	1	Symmetry

Table 3 – Boundary conditions for Yücel's thermal cavity.

Dimensionless number	**Value**
Rayleigh (Ra)	5×10^6
Prandtl (Pr)	0.72
Optical thickness (τ)	0.2, 1.0 or 5.0
Scattering albedo (ω)	0.0
Planck number	0.02

Table 4 – Dimensionless numbers for the Yücel thermal cavity.

RTS. In both cases, the information interpolated out of RTS is the same. Each case was run to 1,000 iterations for thirty times, totalling 30,000 iterations per case. The average and standard deviation of the elapsed wall-clock time for the MFSim to RTS and the RTS to MFSim interpolations were taken for these 30,000 iterations. The same statistics were also taken for the RTS solver time and for the total time of time-step for comparison.

The results are summarized in Table 6 and in Figures 41 and 42. From Figure 42, it can be observed that the interpolation cost increases by $\mathcal{O}(N)$, where N is the number of cells in the target mesh. The interpolation and MPI communication times for both operations (transporting MFSim fields to RTS and transporting RTS fields to MFSim) range from a fraction of a millisecond to up to around 20 ms in the worst scenario (MFSim to RTS operation in Case 7). On average, one can expect a wall-clock time of the order of 10^{-7} s spent transporting a field for each cell in the target mesh. The cost of the RTS to MFSim interpolation is roughly the same for all cases. This is expected, as the number of fields sent to MFSim does not change with the addition of gas modelling, while the number of fields sent to RTS increases threefold when gas modelling is activated. Finally, it can be observed that the standard deviation of each point increases with mesh size: this might be due to MPI scheduling and communication adding cost uncertainty when payloads get bigger.

From Table 6, two comparisons evidence well the impact in computational costs from employing separate spatial meshes. Case 3 shows a total time-step reduction of almost 61% when compared to Case 1, with interpolation and communication costs in Case

Case	MFSim mesh	RTS mesh	Gas model
1	64×64	64×64	Gray
2	64×64	128×128	Gray
3	64×64	32×32	Gray
4	128×128	64×64	Gray
5	32×32	64×64	Gray
6	64×64	64×64	Non-gray WSGG
7	64×64	128×128	Non-gray WSGG
8	64×64	32×32	Non-gray WSGG
9	128×128	64×64	Non-gray WSGG
10	32×32	64×64	Non-gray WSGG

Table 5 – Summary of interpolation cost test cases.

Case	MFSim to RTS	RTS to MFSim	RTS solver	Time-step
1	$1.435 \pm 0.05886\ ms$	$2.765 \pm 0.08117\ ms$	$196.3 \pm 1.750\ ms$	$235.0 \pm 5.997\ ms$
2	$5.784 \pm 0.1928\ ms$	$3.564 \pm 0.08583\ ms$	$886.9 \pm 13.67\ ms$	$938.0 \pm 15.71\ ms$
3	$0.3558 \pm 0.02131\ ms$	$2.452 \pm 0.06751\ ms$	$55.17 \pm 0.9010\ ms$	$90.64 \pm 5.717\ ms$
4	$1.421 \pm 0.09140\ ms$	$7.599 \pm 0.2226\ ms$	$193.8 \pm 1.656\ ms$	$292.9 \pm 14.47\ ms$
5	$1.369 \pm 0.05783\ ms$	$1.269 \pm 0.03517\ ms$	$197.6 \pm 5.289\ ms$	$223.2 \pm 5.562\ ms$
6	$4.732 \pm 0.2377\ ms$	$2.790 \pm 0.06926\ ms$	$216.4 \pm 18.94\ ms$	$879.6 \pm 76.42\ ms$
7	$19.27 \pm 1.113\ ms$	$3.583 \pm 0.09602\ ms$	$949.2 \pm 10.43\ ms$	$2158 \pm 77.13\ ms$
8	$1.228 \pm 0.05216\ ms$	$2.472 \pm 0.06818\ ms$	$61.56 \pm 0.8538\ ms$	$718.0 \pm 71.77\ ms$
9	$4.710 \pm 0.3656\ ms$	$7.518 \pm 0.2469\ ms$	$211.7 \pm 2.273\ ms$	$2645 \pm 280.5\ ms$
10	$4.599 \pm 0.1481\ ms$	$1.334 \pm 0.02385\ ms$	$211.1 \pm 2.226\ ms$	$419.9 \pm 30.46\ ms$

Table 6 – Summary of wall clock time statistics for interpolation cost tests.

1 accounting for $\approx 2\%$ of the total time of time-step and $\approx 3\%$ in Case 3. A similar pattern is seen between Case 6 and Case 8, with a reduction of $\approx 18\%$ in the total time of time-step, with the total time spent interpolating and communicating fields both ways being $\approx 0.85\%$ of the time of time-step in Case 6 and $\approx 0.5\%$ in Case 8. Between cases 6 and 8, the total time-step did not improve as much because the extra models activated to include Y_{CO_2} and Y_{H_2O} in MFSim significantly increased the total time of time-step; nevertheless, the RTS solver time decreased by around 70%, which is quite substantial. Essentially, these extra MFSim models have a strong influence on the simulation time when activated, whereas without them the RTS solver time dominates. Therefore, it can be concluded that utilizing coarser spatial meshes for the RTE algorithm can lead to significant cost reductions for the radiation model with a relatively minor computational cost associated with interpolating and communicating fields.

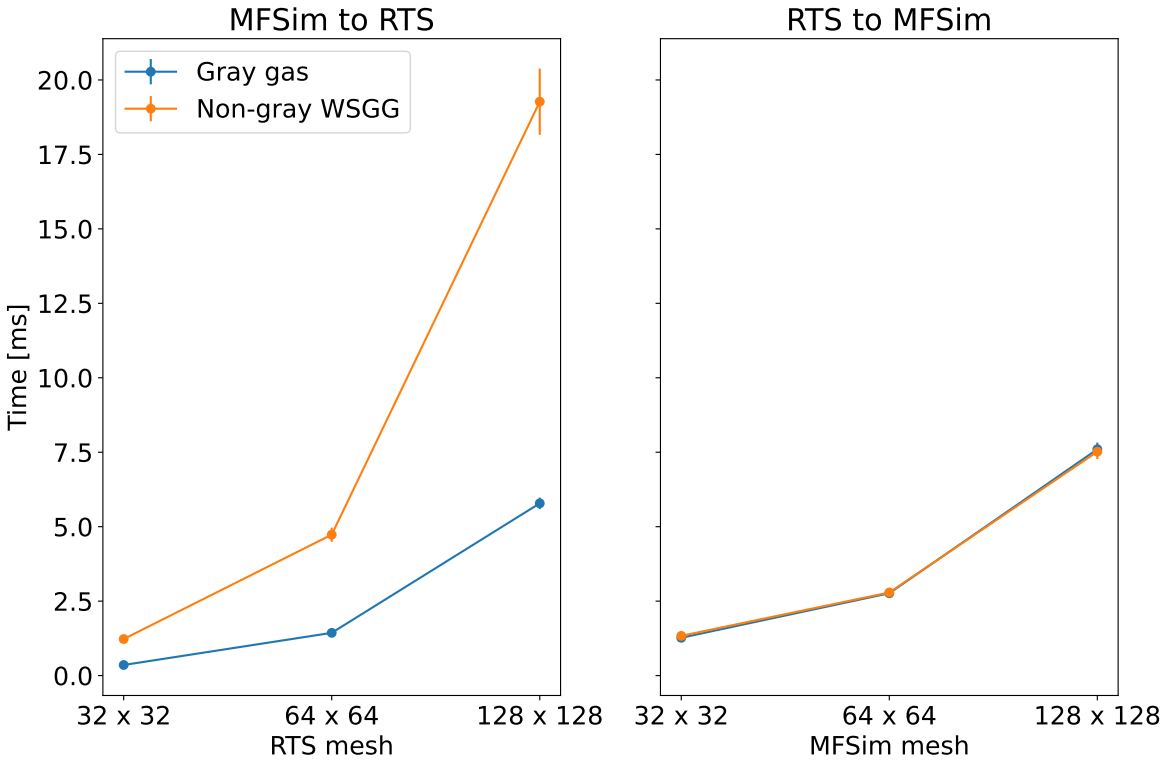

Figure 41 – Interpolation costs for a series of Yücel thermal cavity cases. For the left plot, the MFSim mesh is fixed at 64×64. For the right plot, the RTS mesh is fixed at 64×64 as well.

6.1.2 Results for the validation with adaptive mesh

For the sake of evaluating the MFSim and RTS coupling's performance and accuracy, the cases described in Section 6.1 were solved utilizing an adaptively refined mesh for the CFD calculations, with two physical levels and 48×48 cells in the lowest physical level (`1bot`). The simulation is started without remeshing, which occurs every 200 timesteps, using only the temperature gradient as refinement criteria. The second level increases mesh resolution by 2 times in the x direction, and another 2 times in the y direction. Meanwhile, RTS's mesh was kept fixed at 48×48. This mesh size was chosen as it is close to the 50×50 size chosen by Yücel, Acharya and Williams (1989) while being divisible by more factors of two, which helps the multigrid algorithm work better. Like in the publication, the S4 quadrature was adopted. The case was simulated until the transient field converged to a statistically steady solution.

Figure 43 shows the cavity's isotherms for the case without radiative heat transfer and for three cases with radiative heat transfer with different optical thicknesses. In the case without radiation, it can be seen that the isotherms are neatly stacked on top of each other, forming a type of symmetry that is more evident near the cavity's centre. The inclusion of radiation breaks this symmetry, with the isotherms being displaced around the domain and forming a more curvy profile instead of a horizontally flat and

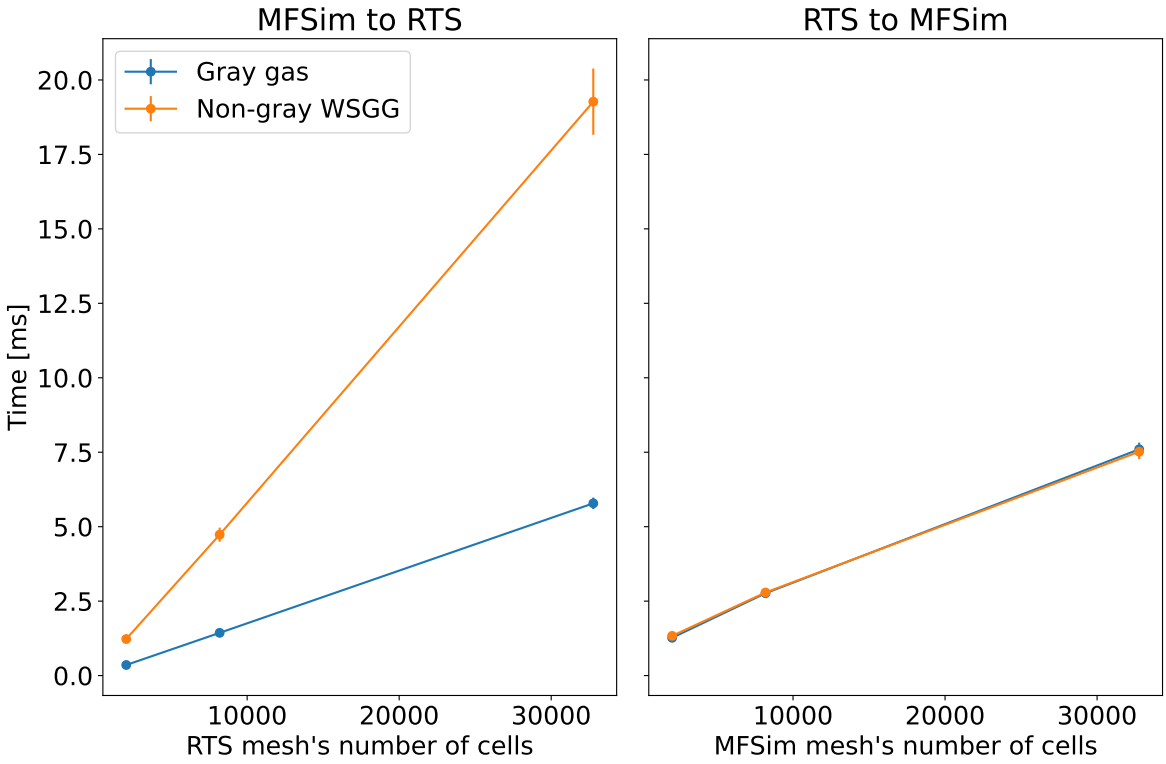

Figure 42 – Figure 41 with x-axis replaced by the number of cells in each mesh. This plot properly shows the $\mathcal{O}(N)$ cost of the interpolation.

neatly stacked arrangement.

The fact that the isotherms become farther apart from one another when radiation is included means that the thermal gradients in the y direction are lessened, which is commonly referred in the literature as a lessened thermal stratification. A consequence of this is that the colder regions concentrate more on the bottom of the cavity (as can be seen from $\theta = 0$), which represents the median temperature of the domain, being further down the cavity. This is in compliance with results shown by Yücel, Acharya and Williams (1989), with the isotherms obtained from the publication matching with the profile taken from the MFSim-RTS simulations.

Another interesting aspect are the adiabatic boundaries. In the case without radiation, the isotherms near the adiabatic boundaries are perpendicular (or almost perpendicular, due to how the plots were generated); this is expected, as the zero Neumann boundary leads to this behaviour. When radiation is considered, this boundary condition is not necessarily equal to zero and some of these isotherms are not perpendicular any more. For example, looking at the $\theta = 0.1$ and $\theta = 0.2$ isotherms, the angle they form in the top and bottom walls changes significantly with the optical thickness: while for $\tau = 5$ they are closer to being perpendicular, for $\tau = 0.2$ and $\tau = 1$ their angles is quite appreciable. This angle is directly related to the radiative heat flux through these boundaries: the more perpendicular these lines, the less radiative heat crosses through the boundary

they meet, such that $\frac{dT}{dy}$ tends to zero.

In Figure 44, the streamlines of these cases can be visualized. At the $Ra = 5 \times 10^6$ regime, due to having surpassed a Rayleigh number threshold, the unicellular flow of the cavity will have already split into two distinct cores in the classic cavity. If radiation is taken into account, however, this development subsides and a unicellular flow returns, as long as the fluid is absorbing enough of the thermal radiation (i.e. has a high enough optical thickness). For a low enough optical thickness, such as the case with $\tau = 0.2$, the streamlines develop into a different flow pattern. All of the streamlines illustrated in Figure 44 coincide to what is told in the reference publication.

The effects on the heat transfer through the boundaries of the domain are discussed based on the Nusselt number, a dimensionless measurement of the heat flux. The Nusselt number can be defined for the convective and radiative heat fluxes, respectively, by:

$$Nu_c = (\nabla T|_w \cdot \hat{n}_w)\frac{L}{T_h - T_c}, \tag{6.1}$$

$$Nu_r = \frac{\phi_0 \cdot \ q_{rad,w}|_{\text{hot wall}}}{4\,\sigma\,T_0^4\,Pl}, \tag{6.2}$$

where $(\nabla T|_w \cdot \hat{n}_w)$ is the temperature gradient on the boundary (for the hot wall, it is simply $\frac{dT}{dx}|_{\text{hot wall}}$), L is the cavity's length, T_h is the hot wall temperature, T_c is the cold wall temperature, $q_{rad,w}|_{\text{hot wall}}$ is the radiative heat flux in the hot wall, Pl is the Planck number and $\phi_0 = \frac{T_h+T_c}{2(T_h-T_c)}$. Most of these values are defined by the setup, while $(\nabla T|_w \cdot \hat{n}_w)$, and $q_{rad,w}|_{\text{hot wall}}$ come from the simulation results.

The Nusselt number on the hot wall was calculated for the convective heat transfer in all cases (Table 7), where a significant decline in the convective Nusselt number is observed when radiation is applied. However, the total heat flux through the walls increases due to radiative transport, which has a Nusselt number around three to five times higher than the convective heat flux. These higher heat fluxes evidence how important radiation is in this cavity's heat transfer processes. The results obtained with MFSim and RTS also agree well with the findings of Yücel, Acharya and Williams (1989), with a relative error of around 1% to 6% for the cases with radiation. This indicates that the MFSim-RTS coupling is capable of accurately capturing the heat transfer of the cavity when radiation is active, particularly the heat transfer by means of radiation. A larger relative deviation of 13.2% can be seen in the case without radiation, which is likely caused by differences between the fluid dynamics model employed by Yücel, Acharya and Williams (1989) and the one from this work: in this work, we utilized an adaptive mesh with higher resolution, a pseudo-2D setup, and solved a transient flow until it converged to a steady-state, while Yücel, Acharya and Williams (1989) simulated a 2D case with a steady-state solver and a coarser mesh employing a dimensionless mathematical model.

Finally, in Figures 45 and 46, comparative velocity plots through the middle of the cavity can be seen. An important point of analysis is how increasing the optical thickness causes a rise in the velocities' amplitudes. They also show that the MFSim-RTS coupling manages to predict the overall flow pattern in the interior of the domain much like Yücel, Acharya and Williams (1989), including the trend of increasing in intensity with an increase in optical thickness. When scaled by the domain's length, the relative error of peak position (both positive and negative) is around $\approx 4\% - 5\%$ for all cases. The difference in the peaks' amplitudes are possibly caused by the differences in the fluid dynamics model, similarly to the differences in the Nusselt number for the case without radiation.

The MFSim-RTS coupling reproduced the patterns and trends described by Yücel, Acharya and Williams (1989), including the distribution of isotherms for different optical thickness configurations, the streamlines profiles and the increase in heat transfer on the hot wall due to radiation. The temperature and heat fluxes measurements agree well with what was shown by Yücel, Acharya and Williams (1989). A few discrepancies can be seen in velocity peaks and in the Nusselt number for the case without radiation, which can be explained by the different fluid dynamics computational models between both results. Overall, the results are quite agreeable and point to the fact that the MFSim-RTS coupling is modelling the radiative heat transfer in this flow correctly.

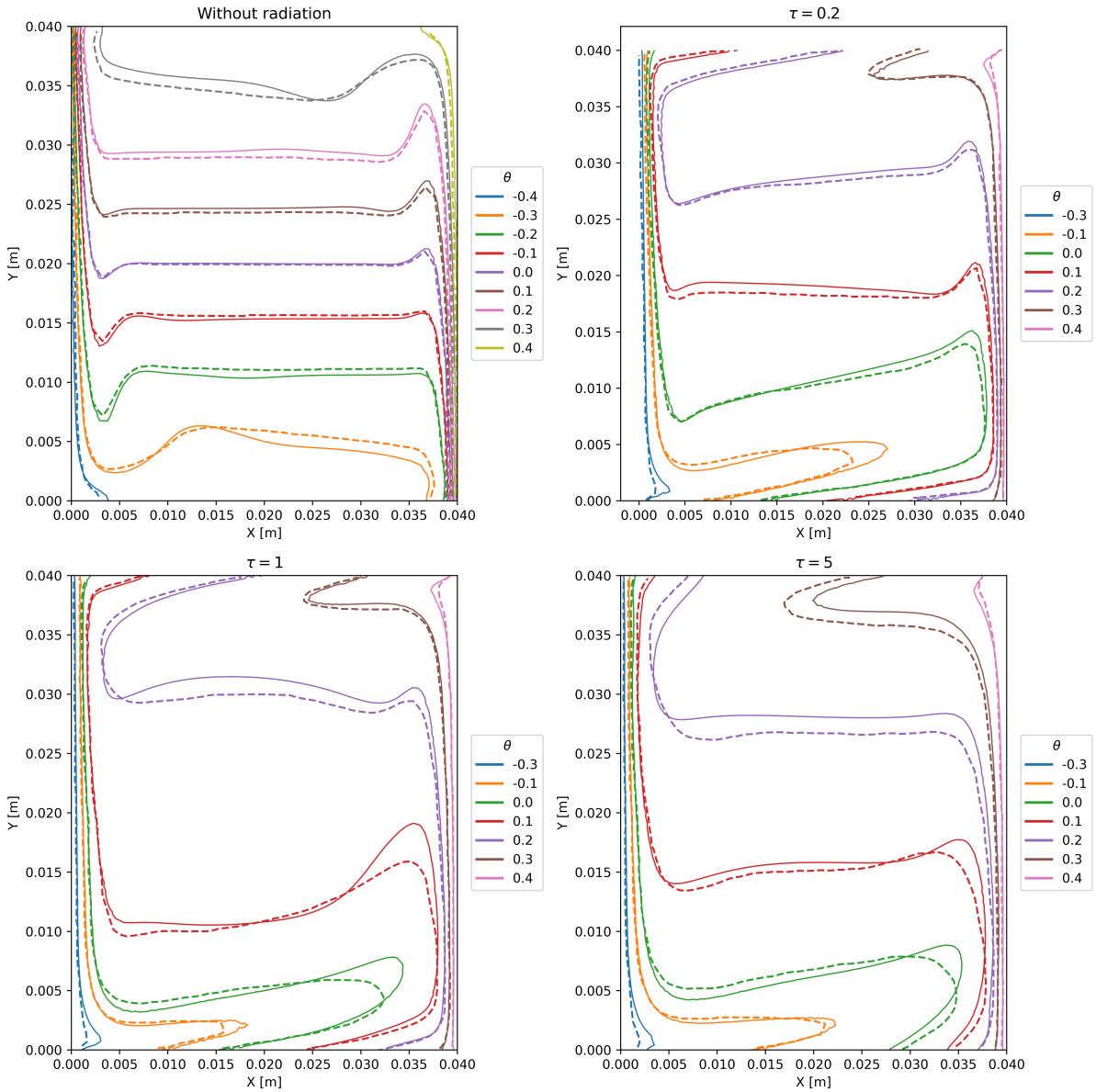

Figure 43 – Isotherms for the Yücel thermal cavity. Full lines correspond to results obtained from the MFSim + RTS coupling using the DOM S4 quadrature. Dashed lines correspond to results obtained from Yücel, Acharya and Williams (1989), also using DOM S4.

Case	MFSim + RTS		Yücel et al.		Relative difference [%]	
	Nu_c	Nu_r	Nu_c	Nu_r	Nu_c	Nu_r
Without radiation	11.94	-	13.76	-	13.2%	-
$\tau = 1$	7.51	32.31	7.68	31.77	2.2%	1.7%
$\tau = 0.2$	8.76	38.07	8.71	37.69	0.6%	1%
$\tau = 5$	7.58	25.05	8.1	23.96	6.4%	4.5%

Table 7 – Comparison of Nusselt number average on the hot wall for the Yücel cavity. The relative difference is calculated by the formula $\frac{|Nu_{(\text{MFSim+RTS})} - Nu_{(\text{Yücel})}|}{|Nu_{(\text{Yücel})}|}$.

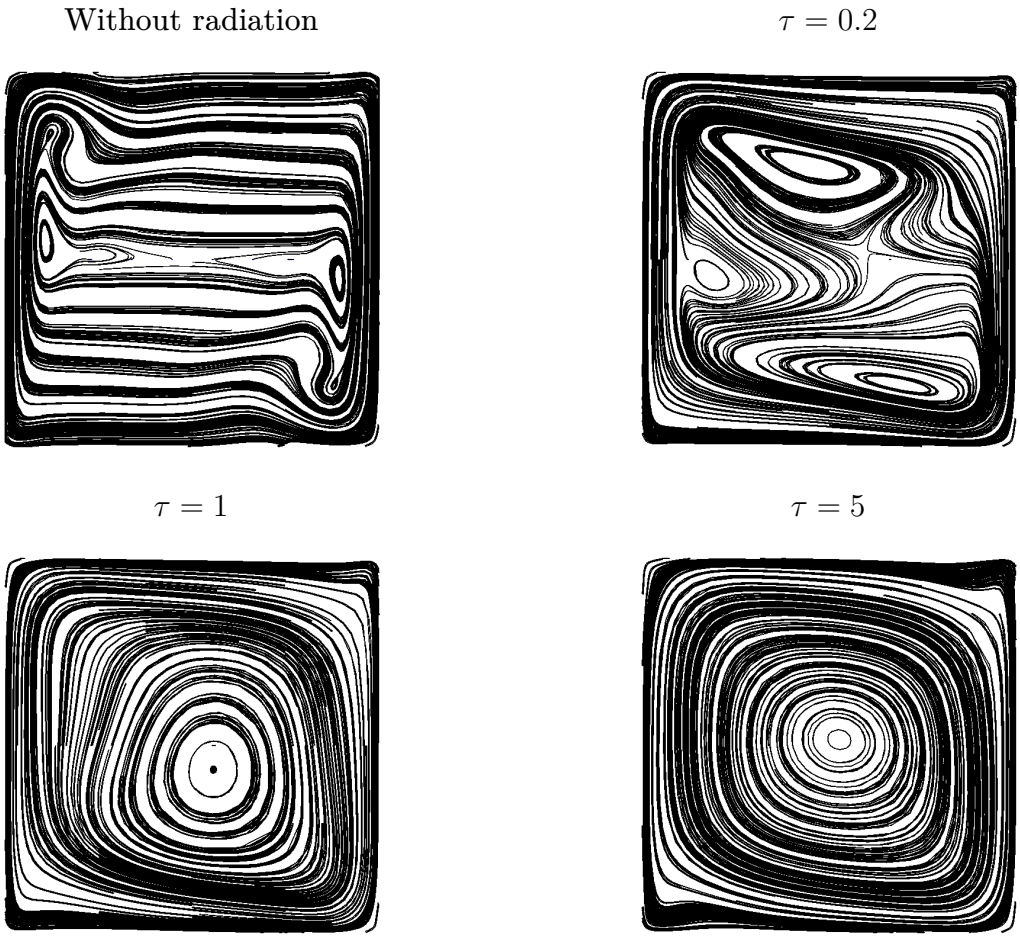

Figure 44 – Streamlines for the Yücel thermal cavity with AMR on the CFD mesh.

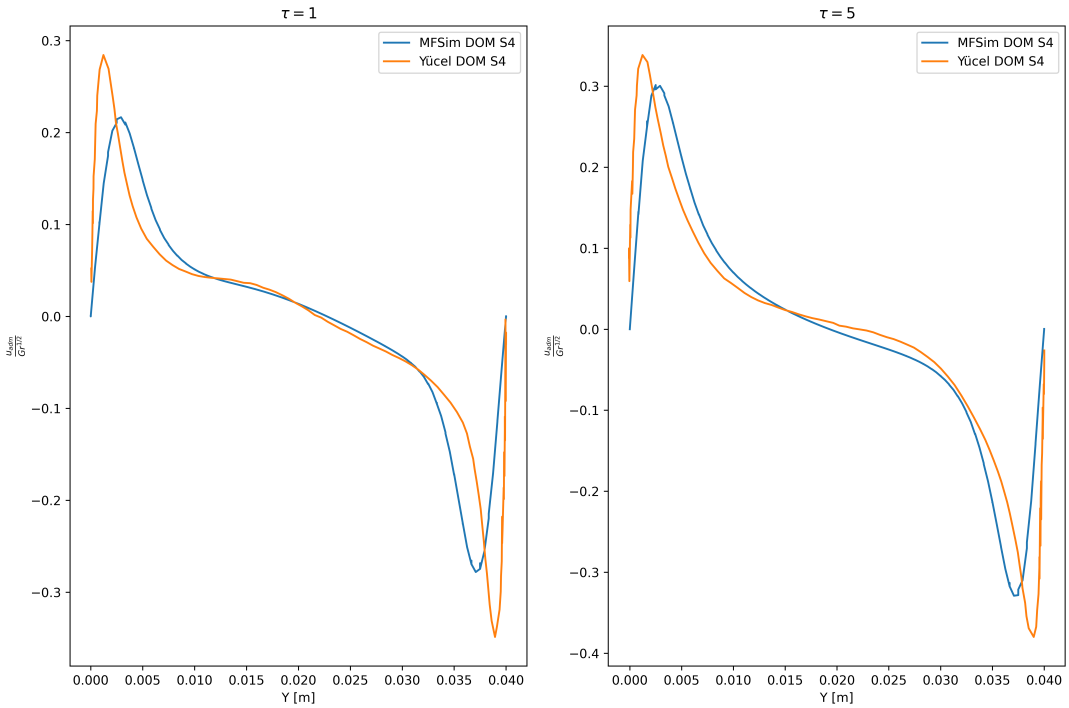

Figure 45 – U Velocity lines in $x = 2\ cm$ for different optical thicknesses.

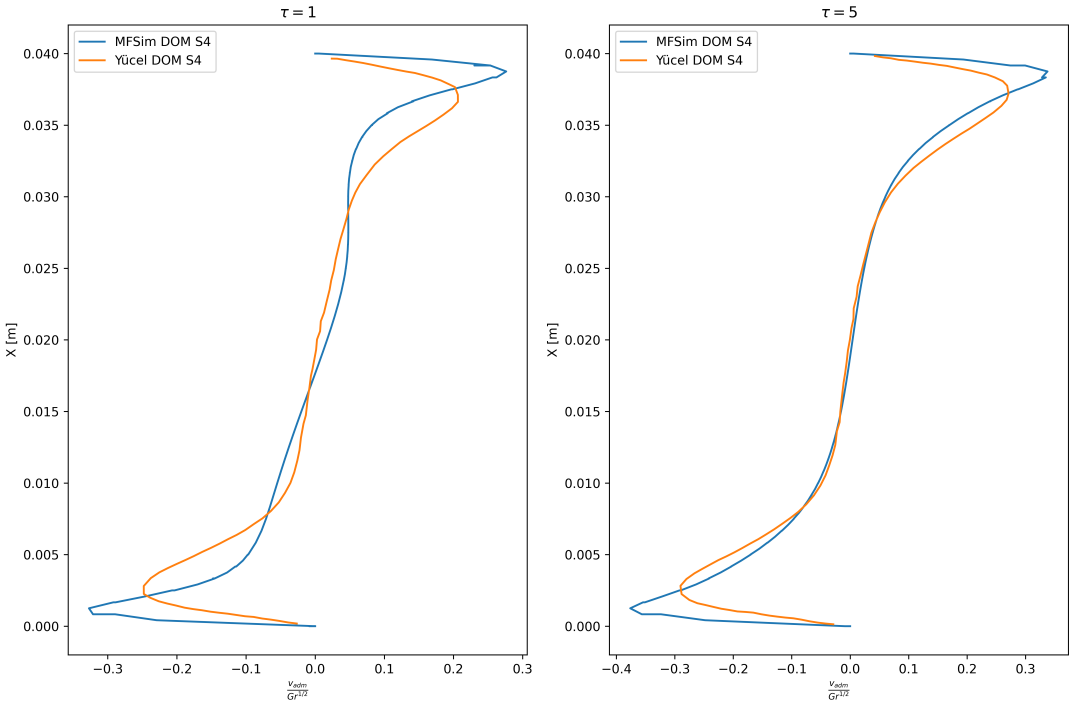

Figure 46 – V velocity lines in $y = 2\ cm$ for different optical thicknesses.

6.2 Salat's Thermal Cavity

As part of the MFSim-RTS coupling verification, the thermal cavity experiment from Salat *et al.* (2004) was modelled and solved computationally. This thermal cavity will be mentioned henceforth as Salat's thermal cavity. The computational domain consists of a $1\ m \times 0.32\ m \times 1\ m$ box (Figure 47), discretized in $64 \times 32 \times 96$ cells in the lowest physical level (`lbot`), two physical levels and dynamic remeshing. The CFD domain was also set to always have the finest level around the walls, as seen in Figure 48a. Every 200 CFD iterations, a remeshing operation occurs. The RTS mesh was set to $32 \times 16 \times 48$ cells, with no stretch (Figure 48b). RTS is called to solve the radiative transport every five CFD iterations, which use adaptive time step with a CFL of 0.7. At later stages of the simulation, each time-step ends up being equal to, or around, 0.1 miliseconds of physical time.

The problem was solved both with and without radiative heat transfer, with the latter consisting of a case using DOM with a S_8 quadrature and a case using FAM with an 8×4 angular discretization (i.e. the azimuthal angle is divided in 8 equal regions and the polar angle is divided in 4 equal regions). For turbulence modelling, the dynamic Smagorinsky model was used (Lilly, 1992) (Germano *et al.*, 1991). It was considered that TRI modelling was not necessary due to the medium being transparent, that is, the fluid does not interact with radiation, only the surfaces of the boundaries. As such, the average temperature fields were fed diretcly to RTS, without applying filtering and

turbulence models to the RTE.

The cavity is filled with initially stagnant air, whose properties were calculated using CoolProp considering a pressure of $P = 101,325\ Pa$ (ambient constant pressure, as in the experiment) and a temperature of $T = 295.5\ K$ (an average of the hot and cold wall temperatures). The natural convection was modelled with Boussinesq's approximation, with the thermal expansion coefficient taken from CoolProp as well. Gravity is set to be parallel to the z direction, going from the top wall to the bottom wall. The values were obtained this way due to Xin *et al.* (2013) not informing the values of all variables as shown in Table 8, but rather only the kinematic viscosity, the thermal diffusivity and thermal expansion coefficients, and thus leaving values like the heat conductivity, specific heat and specific mass implicit. Nevertheless, the values calculated with CoolProp are coherent with the ones informed by Xin *et al.* (2013), displaying only slight differences, and are representative of the real experiment.

For the radiation model, the air was considered transparent, and thus the spectral properties of the media are zero. The emissivities of the walls, as well as the boundary conditions, were taken directly from Xin *et al.* (2013). Finally, due to an inability of simulating the conjugated heat transfer on the top and bottom walls, a fixed temperature profile boundary condition was taken as specified by Sergent *et al.* (2013a). This profile is given by the following function:

$$\theta_{\text{bottom}} = (0.5 - x) + 0.994\frac{x \cdot (x-1) \cdot (x-0.681)}{x \cdot (x-1) - 0.0406(x+0.5)}. \tag{6.3}$$

The above equation can be rewritten, considering that $\theta = \frac{T - \frac{T_h + T_c}{2}}{T_h - T_c}$, where $T_c = 288\ K$ and $T_h = 303\ K$, as:

$$T_{\text{bottom}}(x) = 295.5 + 15 \cdot \theta_{\text{bottom}}(x). \tag{6.4}$$

A summary of the physical properties and boundary conditions is available in Tables 8 and 9. A summary of the dimensionless parameters that describe this case is given in Table 10.

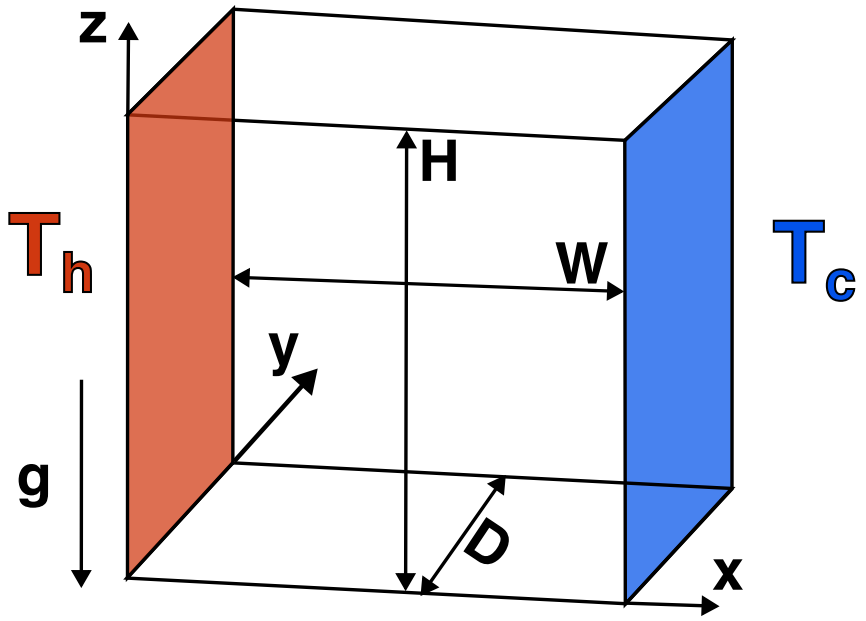

Figure 47 – Illustration of the computational domain for the Salat Thermal Cavity. Cold and hot walls are highlighted with blue and red respectively. The figure also shows the width, height and depth measures of the cavity, as well as its orientation according to the Cartesian axes.

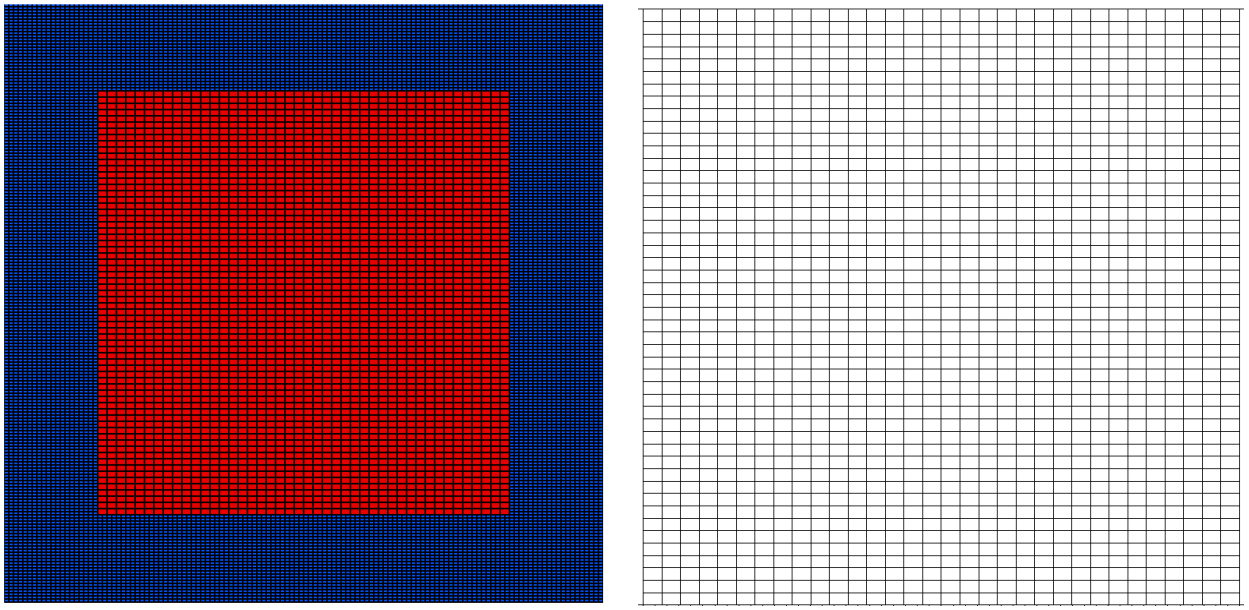

(a) **(b)**

Figure 48 – Initial mesh on MFSim (a) and mesh utilized in RTS (b) viewed in the middle plane $y = 0.16\ m$. In (a), red and blue indicate levels `lbot` and `lbot+1` respectively.

Specific mass (ρ)	$1.1949686702345306\ \frac{m^3}{kg}$
Viscosity(μ)	$1.8319820060333877 \times 10^{-5}\ Pa \cdot s$
Gravity acceleration (g)	$9.81\ \frac{m}{s^2}$
Specific heat (c_p)	$1006.218690342917\ \frac{J}{kg \cdot K}$
Thermal conductivity (k)	$0.02604944054127262\ \frac{W}{m \cdot K}$
Expansion coefficient (β_V)	$0.00339\ \frac{1}{K}$
Absorption coefficient (κ)	$0.0\ m^{-1}$
Scattering coefficient (σ_s)	$0.0\ m^{-1}$

Table 8 – Physical properties used for modelling Salat's thermal cavity.

Field	**West**	**East**	**South**	**North**	**Bottom**	**Top**
Velocity $[\frac{m}{s}]$	No-slip	No-slip	No-slip	No-slip	No-slip	No-slip
Pressure $[Pa]$	$\frac{dP}{dx} = 0$	$\frac{dP}{dx} = 0$	$\frac{dP}{dy} = 0$	$\frac{dP}{dy} = 0$	$\frac{dP}{dz} = 0$	$\frac{dP}{dz} = 0$
Temperature $[K]$	303	288	$\frac{dT}{dy} = \frac{q_{rad,w}}{k}$	$\frac{dT}{dy} = \frac{q_{rad,w}}{k}$	$T_{\text{bot}}(x)$	$-T_{\text{bot}}(1-x)$
Emissivity $[-]$	0.09	0.09	0.97	0.97	0.18	0.18

Table 9 – Boundary conditions for the Salat Thermal Cavity. For the top and bottom walls, the temperature value is given by the function $T_{\text{bot}}(x) = 295.5 + 15 \cdot \left[(0.5 - x) + 0.994\frac{x \cdot (x-1) \cdot (x-0.681)}{x \cdot (x-1) - 0.0406(x+0.5)}\right]$, with x values given in metres.

Dimensionless number	**Value**
Rayleigh (Ra)	1.5×10^9
Prandtl (Pr)	0.7076
Optical thickness (τ)	0.0
Scattering albedo (ω)	-
Planck number (Pl)	0.0178

Table 10 – Dimensionless numbers for Salat's thermal cavity.

6.2.1 Verification results

The results were taken from the dimensionless temperature θ, as well as the dimensionless u_{adm} and w_{adm} velocity fields. These are defined by the following relations:

$$\theta = \frac{T - \frac{T_h + T_c}{2}}{T_h - T_c}, \tag{6.5}$$

$$U_{ref} = \frac{k}{\rho \cdot c_p \cdot H} Ra^{\frac{1}{2}}, \text{ where } H = 1\ m \text{ is the cavity's height,} \tag{6.6}$$

$$u_{adm} = \frac{u}{U_{ref}}, \tag{6.7}$$

$$w_{adm} = \frac{w}{U_{ref}}. \tag{6.8}$$

The time-averaged u_{adm} and w_{adm} velocities, as well as the dimensionless temperature θ were taken on horizontal lines in the mid-depth ($y = L_y/2$) of the cavity, with heights varying from $z = 0.1\ m$ to $z = 0.5\ m$. The dimensionless temperature field on the line $x = L_x/2,\ y = L_y/2$, and the convective Nusselt number on the centre line of the hot wall ($x = 0,\ y = L_y/2$) were also measured. Results from these fields were taken from $t = 100\ s$ to $t = 600\ s$ and their weighted mean was calculated to obtain their time-averaged values $\langle\theta\rangle$, $\langle u_{adm}\rangle$, $\langle w_{adm}\rangle$ and $\langle Nu_c\rangle$. The results were compared to experimental data, as seen in Figures 49 and 50.

The error between the curves from Figures 49 and 50 and the respective experimental data was also measured. For this, the following definitions were used:

- **Error:** $err(\phi) = \phi_{MFSim} - \phi_{exp.}$,
- **Relative Error:** $err_{rel.}(\phi) = \left|\frac{err(\phi)}{\phi_{exp.}}\right|$,
- **Root Mean Square of the Error:** $RMSE(\phi) = \sqrt{\frac{1}{l}\int_0^l err^2(\phi)\,\mathrm{d}l}$,
- **Root Mean Square of the Relative Error:** $RMSE_{rel.}(\phi) = \sqrt{\frac{1}{l}\int_0^l err_{rel.}^2(\phi)\,\mathrm{d}l}$,
- **Maximum Absolute Error:** $L_\infty = max(|err(\phi)|)$,
- **Maximum Absolute Relative Error:** $L_\infty^{rel.} = max(|err_{rel.}(\phi)|)$,

where ϕ is any of the time-averaged fields and l is the length of the line in which they were measured. Error plots based on, respectively, Figures 49 and 50 can be seen in Figures 51 and 52. Global error metrics from these plots are written in Tables 11 and 12.

A stark contrast between the problem solved without and without radiative heat transfer modelling can be noticed in Figures 49 and 51. Overall, the FAM and DOM results are also roughly similar to each other. For instance, the peak value of $\langle w_{adm}\rangle$ is under-predicted by about 15% to 27% in the cases without radiation, while the cases with radiation follow the experimental data quite closely, although for $z = 0.1\,m$ they show a slight deviation in the region after the peak. Despite this, the simulation without radiation modelling still shows a higher RMSE for this plot. The inclusion of radiation increases the magnitude of $\langle w_{adm}\rangle$, which translates to an increase in the flow velocity of thermal cavities that has been observed by both Xin *et al.* (2013) and Yücel, Acharya and Williams (1989). Overall, a reduction of $2\times$ to $3\times$ of the RMSE is observed for all $\langle w_{adm}\rangle$ plots when radiation modelling is applied, except for $z = 0.1\,m$ where they are just slightly lower.

The temperature plots also reveal a difference when radiation is considered, where a reduction of $2\times$ to $7\times$ in the RMSE can be seen. Although all cases display curves that are close to each other, the case without radiation consistently fit the experimental data

better, which leads to a higher global error. This is also the variable that best fits the experimental data overall, as can be seen from its error plots.

The $\langle u_{adm} \rangle$ field present higher errors overall, owing to the fact that the experimental data itself is probably noisier, evidenced for example by the fact that many experimental points cluster together and do not form a neat curve. This makes sense, as the flow in this region points strongly towards the z, meaning that w_{adm} is expected to be intense while u_{adm} should be close to zero. For this field, the models with radiation show relatively good agreement with the experimental data, particularly for $z = 0.2\,m$, $z = 0.3\,m$ and $z = 0.5\,m$, while for $z = 0.1\,m$ it under-predicts the intensities in the middle of the curve (but fits well with the last two points), and in $z = 0.4\,m$ it over-predicts the intensity in the latter half of the points. Nevertheless, a gain in accuracy by applying radiation modelling was achieved for $z = 0.2\,m$ where a reduction of $5\times$ of the RMSE can be seen. In the other plots, the RMSE is roughly the same between the DOM, FAM and no radiation simulations. Similar patterns for the $\langle u_{adm} \rangle$ plots were reproduced by the computer simulations in Xin *et al.* (2013), although the MFSim-RTS coupling showed more accurate predictions for $z = 0.3\,m$.

In Figures 50 and 52, it can be observed that $\langle Nu_c \rangle$ is over-predicted by the model without radiation, similarly to the Yücel thermal cavity cases. The contrast is quite stark, with both RMSE and maxima of the relative error having a $5 \times reduction$ when radiation is applied, similarly to the $\langle \theta \rangle$ and $\langle w_{adm} \rangle$ plots. This means a reduction of 56% in the RMSE to around 11%. The FAM discretization performed slightly better, but it is still relatively close in performance to the DOM model, with their error lines relatively close to each other.

For $\langle \theta \rangle$ in the middle of the cavity shown in Figures 50 and 52, all models under-predict the temperatures at the bottom of the cavity and over-predict the temperatures at the top, although the cases with DOM and FAM do this only around the peaks, fitting well with the experimental data between these peaks, while the no radiation case has a considerably worse fit. This is translated by a relatively flat error plot for the cases with radiation, and a reduction of over two times in the RMSE metric.

Overall, a noticeable gain in accuracy from considering radiative heat transfer can be inferred from all of the plots. Despite this gain in accuracy not being shown in all plots, the models with radiation at worst do not cause a significant reduction in accuracy. This can be seen in the RMSE metrics from Table 11, where they are either several times lower than the case without radiation, or roughly the same. The differences between the DOM and FAM models are also overall quite small, although they may perform a bit better or a bit worse depending on the plot. The accuracy gain is in line with Xin *et al.* (2013), where the authors concluded that the radiative heat transfer between the cavity's surfaces has significant effects on the temperature and flow fields, and must be taken into account for accurately modelling the cavity. In fact, the MFSim-RTS coupling

has shown accuracy similar to the computer simulations by Xin *et al.* (2013).

From this verification, it is clear that radiative heat transfer is appreciable in thermal cavities, even if the media is optically thin (or transparent) and the domain has relatively small temperatures and temperature gradients.

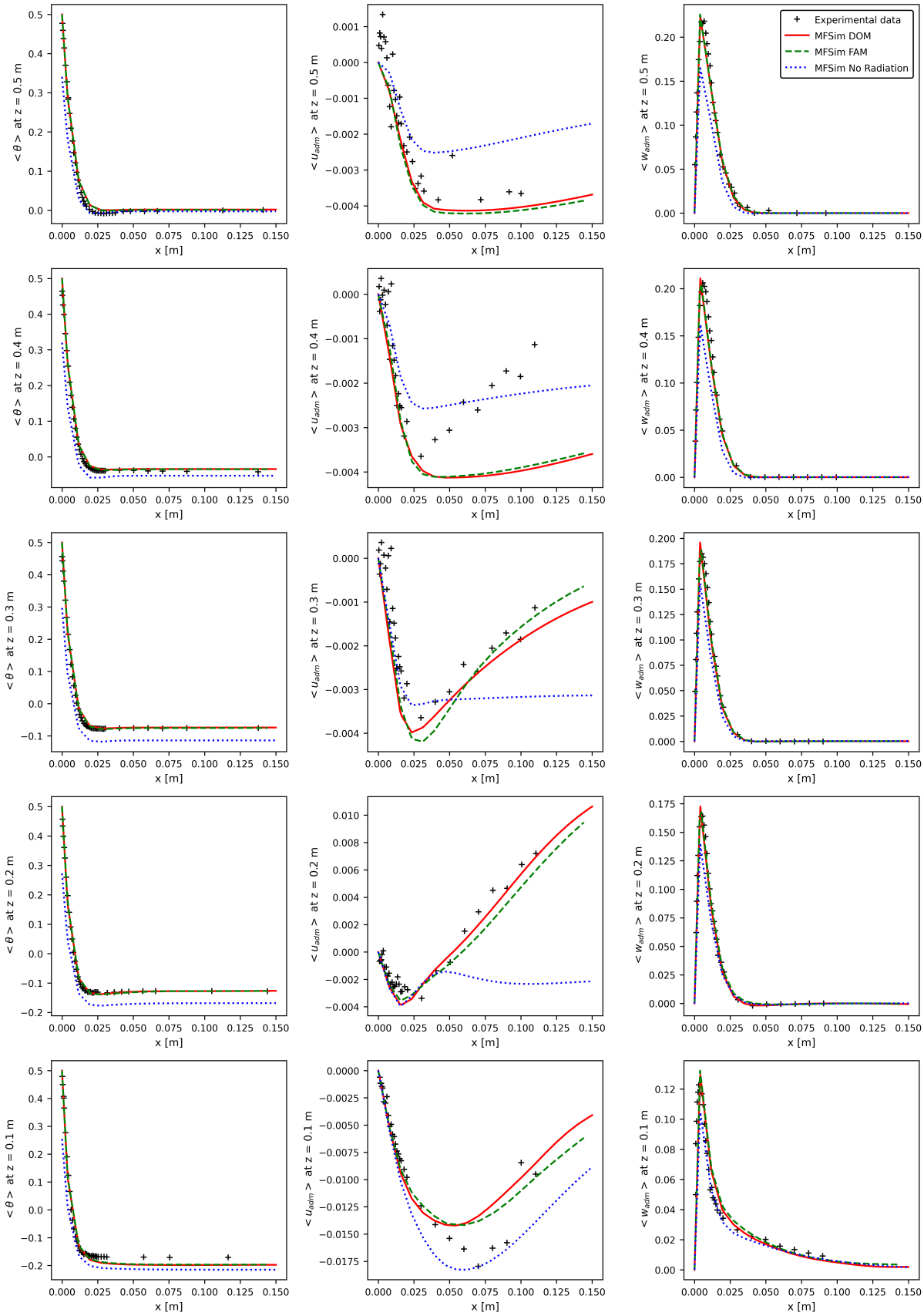

Figure 49 – Time averaged fields for $y = 0.16\ m$.

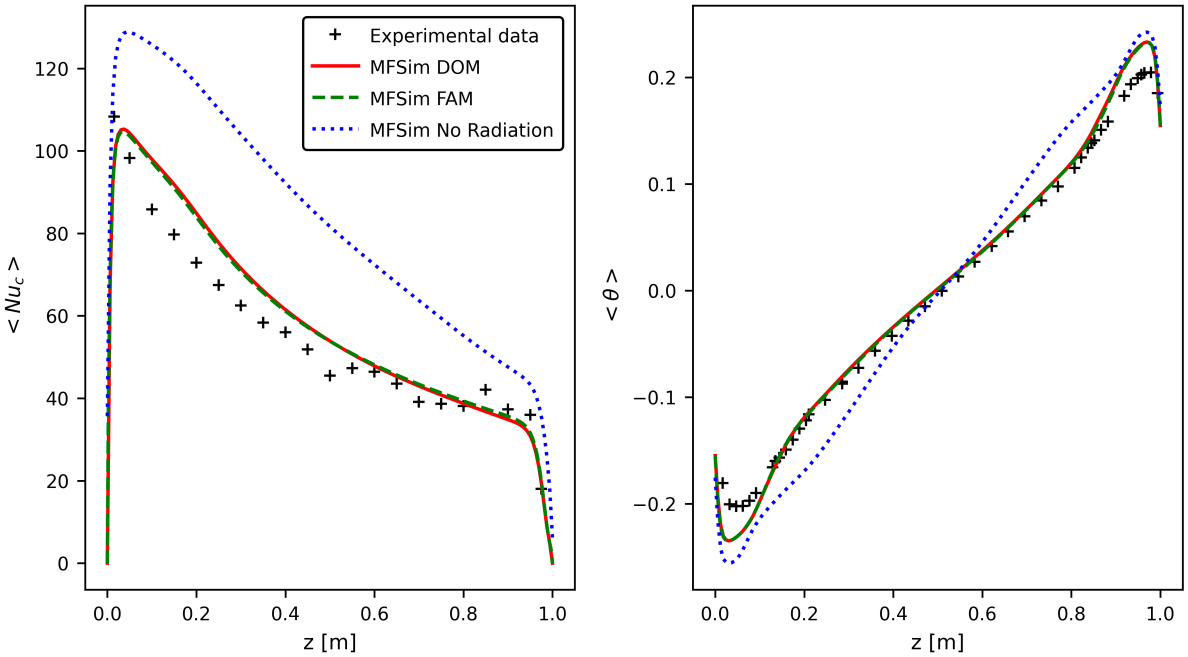

Figure 50 – Time averaged Nusselt number in the middle of the hot wall ($x = 0$, $y = 0.16\ m$) and dimensionless temperature in the middle of the domain ($x = 0.5\ m$, $y = 0.16\ m$).

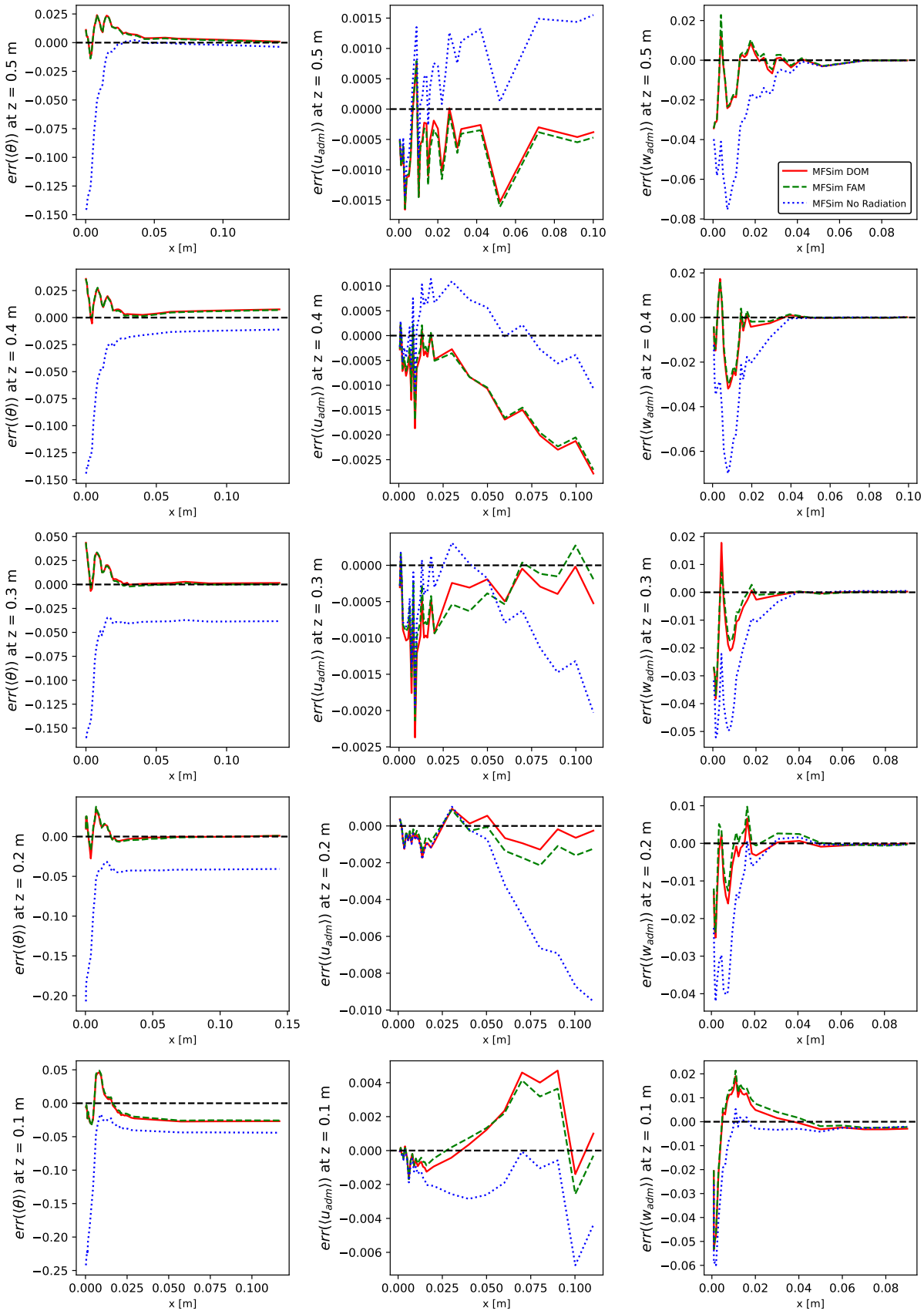

Figure 51 – Errors from the plots of Figure 49.

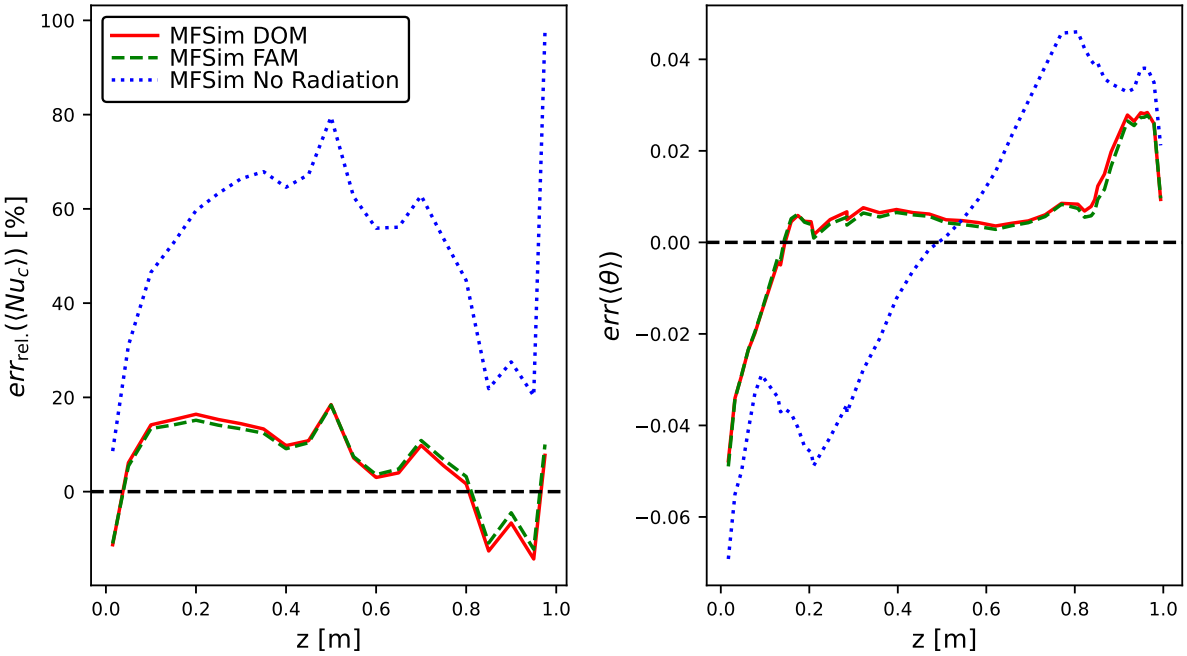

Figure 52 – Errors for plots in Figure 50.

	$\langle\theta\rangle$			$\langle u_{adm}\rangle$			$\langle w_{adm}\rangle$		
Z=0.5 m	**DOM**	**FAM**	**noRad**	**DOM**	**FAM**	**noRad**	**DOM**	**FAM**	**noRad**
RMSE	0.007	0.007	0.028	0.001	0.001	0.001	0.008	0.008	0.023
L_∞	0.024	0.024	0.146	0.002	0.002	0.002	0.034	0.034	0.075
Z=0.4 m	**DOM**	**FAM**	**noRad**	**DOM**	**FAM**	**noRad**	**DOM**	**FAM**	**noRad**
RMSE	0.009	0.008	0.033	0.002	0.001	0.001	0.008	0.007	0.020
L_∞	0.036	0.036	0.144	0.003	0.003	0.001	0.032	0.030	0.070
Z=0.3 m	**DOM**	**FAM**	**noRad**	**DOM**	**FAM**	**noRad**	**DOM**	**FAM**	**noRad**
RMSE	0.008	0.008	0.049	0.001	0.001	0.001	0.007	0.006	0.016
L_∞	0.044	0.044	0.160	0.002	0.002	0.002	0.038	0.037	0.052
Z=0.2 m	**DOM**	**FAM**	**noRad**	**DOM**	**FAM**	**noRad**	**DOM**	**FAM**	**noRad**
RMSE	0.007	0.007	0.051	0.001	0.001	0.005	0.004	0.004	0.012
L_∞	0.035	0.038	0.207	0.002	0.002	0.010	0.025	0.024	0.042
Z=0.1 m	**DOM**	**FAM**	**noRad**	**DOM**	**FAM**	**noRad**	**DOM**	**FAM**	**noRad**
RMSE	0.026	0.024	0.055	0.003	0.002	0.003	0.009	0.009	0.011
L_∞	0.046	0.049	0.242	0.005	0.004	0.007	0.053	0.053	0.060

Table 11 – Global error metrics for the plots in Figure 49.

$\langle \boldsymbol{Nu_c} \rangle$				$\langle \boldsymbol{\theta} \rangle$			
	DOM	**FAM**	**noRad**		**DOM**	**FAM**	**noRad**
$RMSE_{rel.}$	11.48%	10.89%	56.06%	$RMSE$	0.013	0.013	0.033
$L_\infty^{rel.}$	18.48%	18.36%	97.58%	L_∞	0.048	0.049	0.069

Table 12 – Global error metrics for the plots in Figure 50.

7 Conclusions

Radiation is known to have an important role in combustion processes, making its correct modelling fundamental for obtaining accurate data in combustion simulations. One way this is evidenced is that these cases in particular are usually associated with high temperatures which, according to Planck's law, increases radiation emission and thus its effects. Furthermore, combustion products like gases and soot are known to interact strongly with radiation. That said, evidence in literature also suggest that it may play similarly significant roles in many other heat transfer problems, even when such high temperatures are not present, as in the Salat thermal cavity. This is further evidence that it is evidenced an important process to be modelled for computer simulations.

For the sake of implementing radiative heat transfer modelling capabilities in MFSim, initially aiming for simulating industrial processes with combustion, RTS was developed by Rodrigues (2023). Due to focusing his efforts in developing RTS and verifying its accuracy, the coupling with MFSim was in need of adjustments and testing of its own. This work further enhanced this coupling, enabling MFSim to run independently from it, utilizing its usual MPI parallelization and AMR mesh. This allowed for more flexibility in simulations with radiative heat transfer and directly improved computational costs.

The coupling developed in this work was also verified with two thermal cavity cases that serve as good canonical cases for representing radiative heat transfer interactions with fluid dynamics. The setup of these cases was presented in great detail, allowing for them to be reproduced in other software suites. The results obtained are in line with the literature and show interesting behaviour of radiative heat transfer in thermal cavities, such as the increase of flow velocities and a decrease in thermal stratification. It has also been shown that the new coupling layer has relatively small costs when compared to the total time of time step while allowing for significant reductions in the average wall-clock time of each time-step by enabling the utilization of coarser spatial meshes for RTS. The fact that MFSim can now run in parallel with AMR further reduces simulation memory and time costs.

Last, but not least, bibliographic review on cases relating to radiative heat transfer and many aspects of its computational implementation, as well as its coupling with CFD and presence in combustion systems, was performed. This review will hopefully be a stepping stone for future research in the MFLab. This research encompassed topics such as fundamental concepts of radiative heat transfer, the definition of the RTE and its simplifying hypothesis, discretization methods for the angular domain, spectral modelling, RTE solver design (including a discussion on parallelization strategy), the important influence that radiation can have on fluid dynamics, the application of radiation in

combustion processes and trends in academia relating to radiation modelling.

Comparing to Subsection 4.5.3, the coupling of MFSim with RTS now:

- Allows for MFSim to run in parallel, just like in its other applications;
- Allows for MFSim to utilize its AMR mesh, allowing for optimal solver costs for the CFD;
- Allows for RTS to have its own spatial mesh, separate from MFSim;
- Allows for optimization of computational costs by utilizing coarser meshes for the radiative fields, a commonly employed technique.

As such, the objectives of this work have been concluded successfully and another step is taken towards enabling MFSim to simulate problems with complex radiative heat transfer phenomena. Simulations that were formerly prohibitively costly or impractical are now possible.

7.0.1 Future works

Currently, RTS is a promising deterministic RTE solver for general applications in combustion processes. Further development is necessary to expand its applications and scalability. Considering recent trends on reworking MFSim to run on distributed GPU platforms, it is also vital that RTS be adapted to run on this same environment and leverage GPU capabilities. Section 3.10 discusses how a parallel RTE solver may be developed, concluding that a Krylov-based solver may be a better and promising alternative to a parallel sweep algorithm, especially on highly parallel environments like GPUs. In this vein, the use of Diffusion Synthetic Algorithm as pre-conditioner may also help in amplifying the solver performance. It is likely that, going forward, RTS's spatial mesh implementation may be re-written with the prospect of it running in parallel and on a GPU.

Another problem on the radar is that RTS for now can only handle problems with a simple, rectangular geometry: although this is enough for flames such as Smooke (Smooke; Mitchell; Keyes, 1986), Sandia D (Barlow; Frank, 1998; Pitsch; Steiner, 2000) and Liu's sooting flame (Liu *et al.*, 2002b), it is not enough for the complex geometries of the engineering problems it aims to simulate. Although unstructured meshes is a commonly implemented solution to this problem, Immersed Boundary methods such as Multi Direct Forcing (Magalhães, 2022) or Ghost Cells (Ribeiro Neto, 2021) may be a more interesting solution, especially considering that MFSim is built upon this technology. Other codes, like Pele, do use Ghost Cells and contain RTE solvers. Whichever method may be used should concern itself with the existence of solid angle overhang (Section 3.6.2) whenever irregular geometries are present.

On an aspect more focused on radiation modelling, currently RTS can only solve grey gases, or a non-gray mixture of carbon dioxide and water using the WSGG model from Bordbar, Węcel and Hyppänen (2014) and Bordbar, Fraga and Hostikka (2020). Models featuring more participating species, such as CO, may be strategic for the solver. Section 3.8 shows a tendency from researchers of using the FSK family methods for spectral modelling in CFD-RTE couplings due to displaying great accuracy while being relatively lightweight; as such, it might be a strategic addition to the code in conjunction with other WSGG models. Finally, a LBL model for benchmarking purposes may be an interesting idea to pursue as well.

As future projects aim to simulate turbulent flames, it is important to cite TRI models as well, as the literature hints to important contributions to solver accuracy and they should become a considerable concern when more complex simulations are addressed. Although developing and testing TRI models present quite a challenge, it is also a field with many research opportunities, untackled problems and important applications. For example, the recently published Coelho and Fraga (2024) on Large Eddy Simulation (LES) of reactive flows shows scenarios where TRI data are still lacking, and discuss how TRI can be important in LES combustion simulations.

Other RTE discretization methods such as Photon Monte Carlo could be implemented, which could leverage MFSim's already existent Discrete Particle Method (DPM) models used for simulating spray droplets. Monte Carlo is naturally scalable on the GPU due to the fact that each photon particle is independent from each other, making them a prime target for parallelization. Although historically a very costly method, modern GPU platforms may allow them to be cost efficient enough for CFD coupling. Furthermore, it is a trend that can be observed, for example, in the AVBP-Rainier coupling that has been constantly employed in combustion simulations recently.

Finally, the modelling of soot radiation is also a strategic addition to be had in RTS, as these not only commonly appear in combustion, but are well-known to strongly interact with radiation, as noted by Liu *et al.* (2002b). This task would also require the addition of soot models in MFSim, and the ability for RTS to communicate with the soot data from MFSim, making it quite challenging.

For now, a more immediate second step would be simulating non-isothermal jets such as the ones described by Armengol (2019). Another interesting approach would be laminar flames with simple geometries like the experiment described in Smooke, Mitchell and Keyes (1986).

Bibliography

ALCOUFFE, R. E. Diffusion synthetic acceleration methods for the diamond-differenced discrete-ordinates equations. *Nuclear Science and Engineering*, Taylor & Francis, v. 64, n. 2, p. 344–355, 1977. Available from: https://doi.org/10.13182/NSE77-1.

ANDRE, F. *et al.* Accuracy of engineering methods for radiative transfer in CO_2-H_2O mixtures at high temperature. In: *Proceeding of Proceedings of the 9th International Symposium on Radiative Transfer, RAD-19*. Connecticut: Begellhouse, 2019.

ANSYS INC. *Fluent User's Guide*. 2025. [Online]. Available from: https://ansyshelp.ansys.com/public/account/secured?returnurl=/Views/Secured/corp/v242/en/flu_ug/flu_ug.html.

ARMENGOL, J. M. *Numerical investigation of the effects of coupled radiative heat transfer on free turbulent jets of water vapor*. Thesis (Ph.D.) — Université Paris Saclay; Universidade Estadual de Campinas, jun. 2019. Available from: https://theses.hal.science/tel-02275920.

ASLLANAJ, F. *et al.* New gas radiation model of high accuracy based on the principle of weighted sum of gray gases. *Journal of Quantitative Spectroscopy and Radiative Transfer*, 2023. Available from: https://api.semanticscholar.org/CorpusID:266612209.

BADRI, M. *et al.* High performance computation of radiative transfer equation using the finite element method. *Journal of Computational Physics*, v. 360, p. 74–92, 2018. ISSN 0021-9991. Available from: https://www.sciencedirect.com/science/article/pii/S0021999118300378.

BADRI, M. *et al.* Preconditioned Krylov subspace methods for solving radiative transfer problems with scattering and reflection. *Computers & Mathematics with Applications*, v. 77, n. 6, p. 1453–1465, 2019. ISSN 0898-1221. 7th International Conference on Advanced Computational Methods in Engineering (ACOMEN 2017). Available from: https://www.sciencedirect.com/science/article/pii/S0898122118305534.

BARBI, F. *Experimentação numérica de bolhas em ascensão*. Thesis (Ph.D.) — EDUFU - Editora da Universidade Federal de Uberlandia, 2016. Available from: http://dx.doi.org/10.14393/ufu.te.2016.107.

BARLOW, R.; FRANK, J. Effects of turbulence on species mass fractions in methane/air jet flames. *Symposium (International) on Combustion*, v. 27, n. 1, p. 1087–1095, jan. 1998. ISSN 00820784.

BHOWMIK, S.; SEN, M. A study on thermography. *International Journal of Current Trends in Engineering & Research (IJCTER)*, v. 2, p. 117–125, mar. 2016.

BIDI, M.; HOSSEINI, R.; NOBARI, M. Numerical analysis of methane–air combustion considering radiation effect. *Energy Conversion and Management*, v. 49, n. 12, p. 3634–3647, 2008. ISSN 0196-8904. Available from: https://www.sciencedirect.com/science/article/pii/S019689040800277X.

BORDBAR, H. *et al.* Pressure-dependent weighted-sum-of-gray-gases models for heterogeneous CO_2-H_2O mixtures at sub- and super-atmospheric pressure. *International Journal of Heat and Mass Transfer*, v. 173, p. 121207, 2021. ISSN 0017-9310. Available from: https://www.sciencedirect.com/science/article/pii/S0017931021003100.

BORDBAR, H.; FRAGA, G. C.; HOSTIKKA, S. An extended weighted-sum-of-gray-gases model to account for all CO_2-H_2O molar fraction ratios in thermal radiation. *International Communications in Heat and Mass Transfer*, v. 110, p. 104400, 2020. ISSN 0735-1933. Available from: https://www.sciencedirect.com/science/article/pii/S0735193319302660.

BORDBAR, M. H.; WĘCEL, G.; HYPPÄNEN, T. A line by line based weighted sum of gray gases model for inhomogeneous CO_2-H_2O mixture in oxy-fired combustion. *Combustion and Flame*, v. 161, n. 9, p. 2435–2445, 2014. ISSN 0010-2180. Available from: https://www.sciencedirect.com/science/article/pii/S0010218014000935.

BOYAO, W. *Finite Volume Discrete Ordinates Method (FVDOM) in OpenFOAM.* 2020. Accessed: 2025-02-20. Available from: https://boyaowang.github.io/boyaowang_OpenFOAM.github.io/2020/09/30/fvdom/.

CATTA PRETA, R. T. O. *Modelagem matemática e computacional de escoamentos turbulentos bifásicos em regime denso.* Thesis (Ph.D.) — EDUFU - Editora da Universidade Federal de Uberlandia, 2023. Available from: http://dx.doi.org/10.14393/ufu.te.2023.418.

CENTENO, F. R. *et al.* Evaluation of the WSGG model against line-by-line calculation of thermal radiation in a non-gray sooting medium representing an axisymmetric laminar jet flame. *International Journal of Heat and Mass Transfer*, v. 124, p. 475–483, 2018. ISSN 0017-9310. Available from: https://www.sciencedirect.com/science/article/pii/S0017931017350561.

CHANDRASEKHAR, S. Radiative transfer. *New York: Dover*, 1960.

CHAREST, M. R. J.; GROTH, C. P. T.; GÜLDER Ömer L. Solution of the equation of radiative transfer using a Newton–Krylov approach and adaptive mesh refinement. *Journal of Computational Physics*, v. 231, n. 8, p. 3023–3040, 2012. ISSN 0021-9991. Available from: https://www.sciencedirect.com/science/article/pii/S0021999111006711.

CHIUMENTO, V. H. *Modelagem computacional de escoamentos reativos compressíveis.* 101 p. Thesis (Ph.D.) — PPUFU - Portal de Periódicos da Universidade Federal de Uberlândia, 2024. Available from: http://dx.doi.org/10.14393/ufu.te.2025.5008.

COELHO, P. J. Numerical simulation of the interaction between turbulence and radiation in reactive flows. *Progress in Energy and Combustion Science*, v. 33, n. 4, p. 311–383, 2007. ISSN 0360-1285. Available from: https://www.sciencedirect.com/science/article/pii/S036012850600061X.

COELHO, P. J. Boundary conditions. In: *Thermopedia.* [S.l.]: Begel House Inc., 2012. ISBN 978-1-56700-456-4.

COELHO, P. J. Advances in the discrete ordinates and finite volume methods for the solution of radiative heat transfer problems in participating media. *Journal*

of Quantitative Spectroscopy and Radiative Transfer, v. 145, p. 121–146, 2014. ISSN 0022-4073. Available from: https://www.sciencedirect.com/science/article/pii/S0022407314001927.

COELHO, P. J. M.; FRAGA, G. C. Turbulence-radiation interaction in large eddy simulations of turbulent reactive flows: a review. *High Temperatures - High Pressures*, Old City Publishing, v. 53, n. 1-2, p. 3–51, 2024. ISSN 0018-1544. Publisher Copyright: ©2023 Old City Publishing, Inc.

CONSALVI, J. *et al.* Assessment of engineering gas radiative property models in high pressure turbulent jet diffusion flames. *Journal of Quantitative Spectroscopy and Radiative Transfer*, v. 253, p. 107169, 2020. ISSN 0022-4073. Available from: https://www.sciencedirect.com/science/article/pii/S0022407319309355.

DAMASCENO, M. M. R. *Desenvolvimento de uma modelagem para escoamentos reativos em malhas adaptativas do tipo bloco-estruturada.* Thesis (Ph.D.) — EDUFU - Editora da Universidade Federal de Uberlandia, 2018. Available from: http://dx.doi.org/10.14393/ufu.te.2018.771.

DAMASCENO, M. M. R.; SANTOS, J. G. de F.; VEDOVOTTO, J. M. Simulation of turbulent reactive flows using a FDF methodology – advances in particle density control for normalized variables. *Computers & Fluids*, v. 170, p. 128–140, 2018. ISSN 0045-7930. Available from: https://www.sciencedirect.com/science/article/pii/S0045793018302494.

DAMASCENO, M. M. R.; VEDOVOTTO, J.; SILVEIRA NETO, A. Turbulent inlet conditions modeling using large-eddy simulations. *Computer Modeling in Engineering & Sciences*, v. 104, n. 2, p. 105–132, 2015.

DAVIS, G. D. V. Natural convection of air in a square cavity: A bench mark numerical solution. *International Journal for Numerical Methods in Fluids*, v. 3, n. 3, p. 249–264, 1983. Available from: https://onlinelibrary.wiley.com/doi/abs/10.1002/fld.1650030305.

DELORT-LAVAL, M. *Influence des transferts radiatifs sur les écoulements de convection naturelle en régime turbulent, dans des ambiances habitables.* Thesis (Theses) — Université Paris-Saclay, jul. 2023. Available from: https://theses.hal.science/tel-04461746.

DENISON, M. K.; WEBB, B. W. A spectral line-based weighted-sum-of-gray-gases model for arbitrary RTE solvers. *Journal of Heat Transfer*, v. 115, n. 4, p. 1004–1012, nov. 1993. ISSN 0022-1481. Available from: https://doi.org/10.1115/1.2911354.

DOMBROVSKY, L. A.; BAILLIS, D. *Thermal radiation in disperse systems: an engineering approach.* [S.l.]: Begell House New York, 2010. v. 565.

DUARTE, B. A. d. F. *Phase change modelling for non-isothermal flows: a mathematical, numerical and computational model for pure substances.* Thesis (Ph.D.) — EDUFU - Editora da Universidade Federal de Uberlandia, 2018. Available from: http://dx.doi.org/10.14393/ufu.te.2018.795.

ELIAS, A. *Mecanismos virtuais de cinética química aplicados à modelagem de misturas complexas de combustíveis gasosos.* Dissertation (M.Sc.) — EDUFU - Editora da Universidade Federal de Uberlandia, 2023. Available from: http://dx.doi.org/10.14393/ufu.te.2023.421.

ELIAS, A. J. *Modelagem híbrida URANS-LES para escoamentos turbulentos.* Dissertation (M.Sc.) — EDUFU - Editora da Universidade Federal de Uberlandia, 2018. Available from: http://dx.doi.org/10.14393/ufu.di.2018.1219.

FELDICK, A. M.; MODEST, M. F. A spectrally accurate two-dimensional axisymmetric, tightly coupled photon Monte Carlo radiative transfer equation solver for hypersonic entry flows. *Journal of Heat Transfer*, v. 134, n. 12, p. 122701, dec. 2012. ISSN 0022-1481. Available from: https://doi.org/10.1115/1.4007069.

FONSECA, R. J. C. *et al.* A wide-band based weighted-sum-of-gray-gases model for participating media: Application to H_2O-CO_2 mixtures with or without soot. *International Journal of Heat and Mass Transfer*, v. 204, p. 123839, 2023. ISSN 0017-9310. Available from: https://www.sciencedirect.com/science/article/pii/S0017931022013072.

FRAGA, G. C.; COELHO, P. J.; ZHAO, X. Band-wise assessment of turbulence–radiation interaction in the prediction of mean and filtered radiative quantities. *Journal of Quantitative Spectroscopy and Radiative Transfer*, v. 322, p. 109020, 2024. ISSN 0022-4073. Available from: https://www.sciencedirect.com/science/article/pii/S0022407324001274.

FUSEGI, T. *et al.* A numerical study of three-dimensional natural convection in a differentially heated cubical enclosure. *International Journal of Heat and Mass Transfer*, v. 34, n. 6, p. 1543–1557, 1991. ISSN 0017-9310. Available from: https://www.sciencedirect.com/science/article/pii/001793109190295P.

GE, W. *et al.* Comparison of spherical harmonics method and discrete ordinates method for radiative transfer in a turbulent jet flame. *Journal of Quantitative Spectroscopy and Radiative Transfer*, v. 296, p. 108459, 2023. ISSN 0022-4073. Available from: https://www.sciencedirect.com/science/article/pii/S0022407322003946.

GERMANO, M. *et al.* A dynamic subgrid-scale eddy viscosity model. *Physics of Fluids A: Fluid Dynamics*, v. 3, n. 7, p. 1760–1765, jul. 1991. ISSN 0899-8213.

GORDON, I. *et al.* The HITRAN2016 molecular spectroscopic database. *Journal of Quantitative Spectroscopy and Radiative Transfer*, v. 203, p. 3–69, 2017. ISSN 0022-4073. HITRAN2016 Special Issue. Available from: https://www.sciencedirect.com/science/article/pii/S0022407317301073.

GROSSHANDLER, W. L. *RADCAL – a narrow-band model for radiation calculations in a combustion environment.* Gaithersburg, MD: National Institute of Standards and Technology, Building and Fire Research Laboratory, 1993. (NIST technical note; 1402).

GUPTA, A.; HAWORTH, D.; MODEST, M. Turbulence-radiation interactions in large-eddy simulations of luminous and nonluminous nonpremixed flames. *Proceedings of the Combustion Institute*, v. 34, n. 1, p. 1281–1288, 2013. ISSN 15407489.

HOTTEL, H. C.; SAROFIM, A. F. *Radiative transfer.* [S.l.]: McGraw-Hill, 1967. (McGraw-Hill series in mechanical engineering).

HOWELL, J.; MENGÜÇ, M.; SIEGEL, R. *Thermal Radiation Heat Transfer, 6th Edition.* Taylor & Francis, 2015. ISBN 9781466593268. Available from: https://books.google.com.br/books?id=4qYprgEACAAJ.

HURT, R. *Hands in a Bag (black and white): Visible vs Infrared Light*. 2025. [Online; accessed 27. May 2025]. Available from: https://www.spitzer.caltech.edu/image/sig08-005-hands-in-a-bag-black-and-white-visible-vs-infrared-light.

JOLIVET, P.; BADRI, M.; FAVENNEC, Y. Deterministic radiative transfer equation solver on unstructured tetrahedral meshes: Efficient assembly and preconditioning. *Journal of Computational Physics*, v. 437, p. 110313, 2021. ISSN 0021-9991. Available from: https://www.sciencedirect.com/science/article/pii/S0021999121002084.

KOCH, R. *et al.* Discrete ordinates quadrature schemes for multidimensional radiative transfer. *Journal of Quantitative Spectroscopy and Radiative Transfer*, v. 53, n. 4, p. 353–372, 1995. ISSN 0022-4073. Available from: https://www.sciencedirect.com/science/article/pii/0022407395900128.

KOGAWA, T. *et al.* Effect of gas radiation-depended natural convection on the transition of spatially developing boundary layers. *International Journal of Heat and Mass Transfer*, v. 177, p. 121580, 2021. ISSN 0017-9310. Available from: https://www.sciencedirect.com/science/article/pii/S0017931021006839.

KOROTEEVA, E.; SHAGIYANOVA, A. Infrared-based visualization of exhalation flows while wearing protective face masks. *Physics of Fluids*, v. 34, n. 1, p. 011705, jan. 2022. ISSN 1070-6631. Available from: https://doi.org/10.1063/5.0076230.

LARI, K. *et al.* Numerical study of non-gray radiation and natural convection using the full-spectrum k-distribution method. *Numerical Heat Transfer, Part A: Applications*, Taylor & Francis, v. 61, n. 1, p. 61–84, 2012. Available from: https://doi.org/10.1080/10407782.2012.638504.

LARI, K. *et al.* Combined heat transfer of radiation and natural convection in a square cavity containing participating gases. *International Journal of Heat and Mass Transfer*, v. 54, n. 23, p. 5087–5099, 2011. ISSN 0017-9310. Available from: https://www.sciencedirect.com/science/article/pii/S0017931011004029.

LEE, K. *et al.* CO_2 radiation heat loss effects on NOx emissions and combustion instabilities in lean premixed flames. *Fuel*, v. 106, p. 682–689, 2013. ISSN 0016-2361. Available from: https://www.sciencedirect.com/science/article/pii/S0016236112010721.

LILLY, D. K. A proposed modification of the Germano subgrid-scale closure method. *Physics of Fluids A: Fluid Dynamics*, v. 4, n. 3, p. 633–635, mar. 1992. ISSN 0899-8213.

LIU, F. *et al.* Effects of gas and soot radiation on soot formation in a coflow laminar ethylene diffusion flame. *Journal of Quantitative Spectroscopy and Radiative Transfer*, v. 73, n. 2, p. 409–421, 2002. ISSN 0022-4073. Third International Symposium on Radiative Transfer. Available from: https://www.sciencedirect.com/science/article/pii/S0022407301002059.

LIU, F. *et al.* Effects of gas and soot radiation on soot formation in a coflow laminar ethylene diffusion flame. *Journal of Quantitative Spectroscopy and Radiative Transfer*, v. 73, n. 2, p. 409–421, 2002. ISSN 0022-4073. Third International Symposium on Radiative Transfer. Available from: https://www.sciencedirect.com/science/article/pii/S0022407301002059.

MAGALHÃES, G. M. *Modelagem matemática e computacional de escoamentos turbulentos multifásicos em malha adaptativa bloco estruturada utilizando o método multi direct forcing*. Thesis (Ph.D.) — EDUFU - Editora da Universidade Federal de Uberlandia, 2022. Available from: http://dx.doi.org/10.14393/ufu.te.2022.342.

MARKATOS, N.; PERICLEOUS, K. Laminar and turbulent natural convection in an enclosed cavity. *International Journal of Heat and Mass Transfer*, v. 27, n. 5, p. 755–772, 1984. ISSN 0017-9310. Available from: https://www.sciencedirect.com/science/article/pii/0017931084901455.

MARTINS, J. K. A. *Modelagem euler-lagrange da evaporação de um spray multicomponente em meio heterogêneo*. Dissertation (M.Sc.) — EDUFU - Editora da Universidade Federal de Uberlandia, 2023. Available from: http://dx.doi.org/10.14393/ufu.di.2023.407.

MCGRATTAN, K. *et al. Fire Dynamics Simulator, Technical Reference Guide, Sixth Edition*. [S.l.]: Special Publication (NIST SP), National Institute of Standards and Technology, Gaithersburg, MD, 2013.

MELO, R. *Modelagem e simulação de escoamentos turbulentos com efeitos térmicos, utilizando a metodologia da fronteira imersa e malha adaptativa*. Thesis (Ph.D.) — EDUFU - Editora da Universidade Federal de Uberlandia, 2017. Available from: http://dx.doi.org/10.14393/ufu.te.2017.79.

MIRANDA, F. C. *et al.* Study of turbulence-radiation interactions in large-eddy simulation of scaled Sandia flame D. *Journal of Quantitative Spectroscopy and Radiative Transfer*, v. 228, p. 47–56, 2019. ISSN 0022-4073. Available from: https://www.sciencedirect.com/science/article/pii/S0022407318307088.

MODEST, M. F.; HAWORTH, D. C. *Radiative Heat Transfer in Turbulent Combustion Systems*. Springer International Publishing, 2016. ISSN 2191-5318. ISBN 9783319272917. Available from: http://dx.doi.org/10.1007/978-3-319-27291-7.

MODEST, M. F.; MAZUMDER, S. *Radiative Heat Transfer*. Fourth edition. London: Academic Press, 2022. ISBN 978-0-323-98406-5 978-0-323-98407-2.

MODEST, M. F.; ZHANG, H. The full-spectrum correlated-k distribution for thermal radiation from molecular gas-particulate mixtures. *Journal of Heat Transfer*, v. 124, n. 1, p. 30–38, jun. 2001. ISSN 0022-1481. Available from: https://doi.org/10.1115/1.1418697.

MORALES, F. A. P. *et al.* Fluid–structure interaction with a finite element–immersed boundary approach for compressible flows. *Ocean Engineering*, v. 290, p. 115755, 2023. ISSN 0029-8018. Available from: https://www.sciencedirect.com/science/article/pii/S002980182302139X.

MOTA, P. H. A. *Modelagem numérico-computacional multiníveis de processos de corrosão em sistemas fluidodinâmicos*. Thesis (Ph.D.) — EDUFU - Editora da Universidade Federal de Uberlandia, 2023. Available from: http://dx.doi.org/10.14393/ufu.te.2023.72.

MOUSTAFA, S. *Massively Parallel Cartesian Discrete Ordinates Method for Neutron Transport Simulation*. Thesis (Ph.D.) — Université de Bordeaux, dec. 2015. Available from: https://theses.hal.science/tel-01379686.

MURTHY, J.; MATHUR, S. Finite volume method for radiative heat transfer using unstructured meshes. *Journal of thermophysics and heat transfer*, v. 12, n. 3, p. 313–321, 1998.

NAKAMURA, M. *et al.* Soot formation, spray characteristics, and structure of jet spray flames under high pressure. *Combustion and Flame*, v. 158, n. 8, p. 1615–1623, 2011. ISSN 0010-2180. Available from: https://www.sciencedirect.com/science/article/pii/S0010218010003871.

NUSSENZVEIG, H. M. *Curso de física básica: Ótica, relatividade, física quântica (vol. 4), 1st Edition.* [S.l.]: Editora Blucher, 1998.

OLIVEIRA, G. S. *Implementation of numerical-computational tools for fluid-structure interaction analysis in industrial cases.* Dissertation (M.Sc.) — PPUFU - Portal de Periódicos da Universidade Federal de Uberlândia, 2025. Available from: http://dx.doi.org/10.14393/ufu.di.2025.130.

OPENFOAM FOUNDATION. *The OpenFOAM Source Code Guide | OpenFOAM v13.* 2025. [Online]. Available from: https://cpp.openfoam.org/v13.

ORBEGOSO, E. M. M. *Estudo numérico da radiação térmica e sua interação com a fuligem formada na combustão turbulenta de combustíveis líquidos e gasosos.* Thesis (Ph.D.) — PUC Rio, 2013.

OWEN, L. D. *et al.* PeleMP: The multiphysics solver for the combustion Pele adaptive mesh refinement code suite. *Journal of Fluids Engineering*, v. 146, n. 4, p. 041103, feb. 2024. ISSN 0098-2202. Available from: https://doi.org/10.1115/1.4064494.

PADILLA, E. L. M.; LOURENÇO, M. A. S.; SILVEIRA NETO, A. Natural convection inside cubical cavities: numerical solutions with two boundary conditions. *J. Braz. Soc. Mech. Sci. Eng.*, Springer Science and Business Media LLC, v. 35, n. 3, p. 275–283, oct. 2013.

PALLUOTTO, L. *Quasi-Monte Carlo computation of radiative heat transfer in coupled Large Eddy Simulation of a swirled premixed flame.* Thesis (Ph.D.) — Université Paris-Saclay and Université libre de Bruxelles, jul. 2019. Available from: https://theses.hal.science/tel-02385868.

PINHEIRO, A. P. *Eulerian-Lagrangian modelling of aviation kerosene spray breakup and evaporation.* Thesis (Ph.D.) — EDUFU - Editora da Universidade Federal de Uberlandia, 2022. Available from: http://dx.doi.org/10.14393/ufu.te.2022.357.

PITSCH, H.; STEINER, H. Large-eddy simulation of a turbulent piloted methane/air diffusion flame (Sandia flame D). *Physics of Fluids*, v. 12, n. 10, p. 2541–2554, oct. 2000. ISSN 1070-6631, 1089-7666.

PIVELLO, M. *et al.* A fully adaptive front tracking method for the simulation of two phase flows. *International Journal of Multiphase Flow*, v. 58, p. 72–82, 2014. ISSN 0301-9322. Available from: https://www.sciencedirect.com/science/article/pii/S0301932213001286.

POLYZOS, K. D. *Detection and recognition of aerial targets via RADAR data processing, machine learning techniques and neural networks.* Dissertation (Diploma

Thesis) — University of Patras, School of Engineering, Patras, Greece, 2018. Supervisor: Evangelos Dermatas; Laboratory: Wired Communications. Available from: http://hdl.handle.net/10889/11880.

RASHIDZADEH, S. *et al.* On the compromise between accuracy and computational cost for different global spectral models. In: BEGEL HOUSE INC. *Proceedings of the 10th International Symposium on Radiative Transfer, RAD-23 Thessaloniki, Greece, 12–16 June 2023*. [S.l.], 2023.

REFAHI, S. *Développement d'un code de transfert radiatif et de son couplage avec un code LES*. Thesis (Ph.D.) — École Centrale Paris, feb. 2013. Available from: https://theses.hal.science/tel-00832350.

RIBEIRO NETO, H. *Modelagem matemática e computacional de acoplamento fluido-estrutura em ambiente paralelo e com malha adaptativa*. Thesis (Ph.D.) — EDUFU - Editora da Universidade Federal de Uberlandia, 2021. Available from: http://dx.doi.org/10.14393/ufu.te.2021.412.

RODRIGUES, G. S. *Desenvolvimento de um simulador de transferência radiativa de código aberto para combustão de gases não cinzentos*. Thesis (Ph.D.) — Universidade Federal de Uberlândia, 2023.

RODRIGUES, P. *Modélisation multiphysique de flammes turbulentes suitées avec la prise en compte des transferts radiatifs et des transferts de chaleur pariétaux*. Thesis (Ph.D.) — Université Paris Saclay, jun. 2018. Available from: https://theses.hal.science/tel-01871656.

ROGER, M.; COELHO, P. J.; da Silva, C. B. The influence of the non-resolved scales of thermal radiation in large eddy simulation of turbulent flows: A fundamental study. *International Journal of Heat and Mass Transfer*, v. 53, n. 13, p. 2897–2907, 2010. ISSN 0017-9310. Available from: https://www.sciencedirect.com/science/article/pii/S0017931010000608.

ROTHMAN, L. *et al.* HITEMP, the high-temperature molecular spectroscopic database. *Journal of Quantitative Spectroscopy and Radiative Transfer*, v. 111, n. 15, p. 2139–2150, 2010. ISSN 0022-4073. XVIth Symposium on High Resolution Molecular Spectroscopy (HighRus-2009). Available from: https://www.sciencedirect.com/science/article/pii/S002240731000169X.

SADEGHI, H. *et al.* Weighted-sum-of-gray-gases models for non-gray thermal radiation of hydrocarbon fuel vapors, CH_4, CO and soot. *Fire Safety Journal*, v. 125, p. 103420, 2021. ISSN 0379-7112. Available from: https://www.sciencedirect.com/science/article/pii/S0379711221001612.

SALAT, J. *et al.* Experimental and numerical investigation of turbulent natural convection in a large air-filled cavity. *International Journal of Heat and Fluid Flow*, v. 25, n. 5, p. 824–832, 2004. ISSN 0142-727X. Selected papers from the 4th International Symposium on Turbulence Heat and Mass Transfer. Available from: https://www.sciencedirect.com/science/article/pii/S0142727X04000839.

SANTOS, J. G. d. F. *Modelagem matemática e computacional de escoamentos gás-sólido em malha adaptativa dinâmica*. Thesis (Ph.D.) — PPUFU - Portal

de Periódicos da Universidade Federal de Uberlândia, 2019. Available from: http://dx.doi.org/10.14393/ufu.di.2019.2218.

SANTOS, R. G. *et al.* Coupled large eddy simulations of turbulent combustion and radiative heat transfer. *Combustion and Flame*, v. 152, n. 3, p. 387–400, 2008. ISSN 0010-2180. Available from: https://www.sciencedirect.com/science/article/pii/S001021800700288X.

SCHONFELD, T.; RUDGYARD, M. Steady and unsteady flow simulations using the hybrid flow solver AVBP. *AIAA Journal*, v. 37, n. 11, p. 1378–1385, 1999. Available from: https://doi.org/10.2514/2.636.

SCOGGINS, J. *Développement de méthodes numériques et étude des phénomènes couplés d'écoulement, de rayonnement, et d'ablation dans les problèmes d'entrée atmosphérique*. Thesis (Ph.D.) — Université Paris Saclay, sep. 2017. Available from: https://theses.hal.science/tel-01639797.

SERGENT, A. *et al.* Resolving the stratification discrepancy of turbulent natural convection in differentially heated air-filled cavities Part II: End walls effects using large eddy simulation. *International Journal of Heat and Fluid Flow*, v. 39, p. 15–27, 2013. ISSN 0142-727X. Available from: https://www.sciencedirect.com/science/article/pii/S0142727X12001269.

SERGENT, A. *et al.* Resolving the stratification discrepancy of turbulent natural convection in differentially heated air-filled cavities – Part I: Reference solutions using Chebyshev spectral methods. *International Journal of Heat and Fluid Flow*, v. 39, p. 1–14, 2013. ISSN 0142-727X. Available from: https://www.sciencedirect.com/science/article/pii/S0142727X12001178.

SHEN, T.; HUANG, Y.; CHIEN, S. Using fire dynamic simulation (FDS) to reconstruct an arson fire scene. *Building and Environment*, v. 43, n. 6, p. 1036–1045, 2008. ISSN 0360-1323. Available from: https://www.sciencedirect.com/science/article/pii/S0360132306003908.

SILVEIRA NETO, A. *Turbulent Flows: Physical Analysis and Theoretical Modeling*. Cham: Springer Nature Switzerland, 2026. ISBN 978-3-031-89221-9 978-3-031-89222-6.

SMOOKE, M. D.; MITCHELL, R. E.; KEYES, D. E. Numerical solution of two-dimensional axisymmetric laminar diffusion flames. *Combustion Science and Technology*, v. 67, n. 4-6, p. 85–122, oct. 1986. ISSN 0010-2202, 1563-521X.

SNYDER, D. Cooling of lava flows on Venus: The coupling of radiative and convective heat transfer. *Journal of Geophysical Research: Planets*, Wiley Online Library, v. 107, n. E10, p. 10–1, 2002.

SOLOVJOV, V. P.; WEBB, B. W. SLW modeling of radiative transfer in multicomponent gas mixtures. *Journal of Quantitative Spectroscopy and Radiative Transfer*, v. 65, n. 4, p. 655–672, 2000. ISSN 0022-4073. Available from: https://www.sciencedirect.com/science/article/pii/S0022407399001338.

SOUCASSE, L. *Effets des transferts radiatifs sur les écoulements de convection naturelle dans une cavité différentiellement chauffée en régimes transitionnel et*

faiblement turbulent. Thesis (Ph.D.) — École Centrale Paris, dec. 2013. Available from: https://theses.hal.science/tel-00978507.

SOUZA, P. R. C. *et al.* Multi-phase fluid–structure interaction using adaptive mesh refinement and immersed boundary method. *Journal of the Brazilian Society of Mechanical Sciences and Engineering*, Springer Science and Business Media LLC, v. 44, n. 4, mar. 2022. ISSN 1806-3691. Available from: http://dx.doi.org/10.1007/s40430-022-03417-x.

TARDELLI, L. P. *Investigating the LES strategy for the prediction of soot production in an aero-engine combustor*. Thesis (Ph.D.) — Université Paris-Saclay, mar. 2021. Available from: https://theses.hal.science/tel-03244444.

TORRES, K. *Numerical simulation and thermal radiation analysis in sooted flames : impact of radiative properties description*. Thesis (Ph.D.) — Université Paris-Saclay, jul. 2021. Available from: https://theses.hal.science/tel-03462471.

VASCONCELLOS, L. G. S. *Advanced Computational Fluid Dynamics in Bloodstain Pattern Analysis: Investigating Non-Newtonian Properties for Forensic Applications*. Thesis (Ph.D.) — PPUFU - Portal de Periódicos da Universidade Federal de Uberlândia, 2024. Available from: http://dx.doi.org/10.14393/ufu.di.2024.488.

VEDOVOTTO, J. M. *Mathematical and numerical modeling of turbulent reactive flows using a hybrid LES / PDF methodology*. Thesis (Ph.D.) — ISAE-ENSMA École Nationale Supérieure de Mécanique et d'Aérotechnique - Poitiers, nov. 2011. Available from: https://theses.hal.science/tel-00665800.

VEDOVOTTO, J. M.; SERFATY, R.; SILVEIRA NETO, A. Mathematical and numerical modeling of turbulent flows. *Anais da Academia Brasileira de Ciências*, Academia Brasileira de Ciências, v. 87, n. 2, p. 1195–1232, Apr 2015. ISSN 0001-3765. Available from: https://doi.org/10.1590/0001-3765201520140510.

VILLAR, M. M. *Análise numérica detalhada de escoamentos multifásicos bidimensionais*. Thesis (Ph.D.) — Universidade Federal de Uberlândia, apr. 2007.

VISKANTA, R. Radiation heat transfer in combustion systems. *Progress in Energy and Combustion Science*, v. 13, n. 2, p. 95–129, 1987.

WANG, C. *et al.* A full-spectrum k-distribution look-up table for radiative transfer in nonhomogeneous gaseous media. *Journal of Quantitative Spectroscopy and Radiative Transfer*, v. 168, p. 46–56, 2016. ISSN 0022-4073. Available from: https://www.sciencedirect.com/science/article/pii/S0022407315002952.

XIN, S. *et al.* Resolving the stratification discrepancy of turbulent natural convection in differentially heated air-filled cavities. Part III: A full convection–conduction–surface radiation coupling. *International Journal of Heat and Fluid Flow*, v. 42, p. 33–48, 2013. ISSN 0142-727X. Available from: https://www.sciencedirect.com/science/article/pii/S0142727X13000374.

YÜCEL, A.; ACHARYA, S.; WILLIAMS, M. Natural convection and radiation in a square enclosure. *Numerical Heat Transfer*, Taylor & Francis, v. 15, n. 2, p. 261–278, 1989.

ZENOU, J. B. *Thermal radiation effects on flame speed and acceleration in exhaust-gases-diluted mixtures.* Thesis (Ph.D.) — Université Paris-Saclay, may 2025. Available from: https://theses.hal.science/tel-05229914.

ZHANG, J. *Radiation Monte Carlo approcah dedicated to the coupling with LES reactive simulation.* Thesis (Ph.D.) — École Centrale Paris, jan. 2011. Available from: https://theses.hal.science/tel-00594229.

ZHANG, Y. *Coupled convective heat transfer and radiative energy transfer in turbulent boundary layers.* Thesis (Ph.D.) — École Centrale Paris, sep. 2013. Available from: https://theses.hal.science/tel-00969159.